

**HIGH ENERGY ALL-SOLID-STATE LITHIUM
SECONDARY BATTERIES COMBINING SULFUR-BASED
CATHODES WITH ARGYRODITE ELECTROLYTE**

CHEN MAOHUA

(Bachelor of *Eng*, *SJTU*)

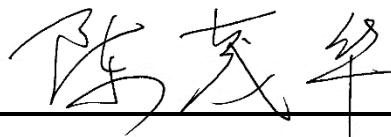
**A THESIS SUBMITTED
FOR THE DEGREE OF DOCTOR OF PHILOSOPHY
DEPARTMENT OF MATERIAL SCIENCE AND ENGINEERING
NATIONAL UNIVERSITY OF SINGAPORE**

2014

DECLARATION

I hereby declare that this thesis is my original work and it has been written by me in its entirety. I have duly acknowledged all the sources of information which have been used in the thesis.

This thesis has also not been submitted for any degree in any university previously.

A handwritten signature in black ink, consisting of three characters: '陈', '茂', and '华'. The signature is written in a cursive style and is positioned above a horizontal line.

Chen Maohua

18/08/2014

ACKNOWLEDGEMENTS

First of all, I would like to express my sincere appreciation to my supervisor, associate professor Stefan Adams, who gave me this precious opportunity to pursue my PhD on such an interesting and promising area. His supportive and invaluable supervision effectively helped me throughout the projects. It is really a pleasant and inspiring experience working with him.

I would like to give my thanks to my group members, Dr. R. Prasada Rao, Dr. M. V. Venkatesh Reddy, Li Kangle, To Tran Thinh, Gu Wenyi, Dorsasadat Safanama, Yow Zhen Feng and Chen Haoming, for their advice and supports in my research. I also would like to extend my thanks to other friends Li Feng, Tang Chunhua, Lv Wenlai, Gui Yang, Yin Xuesong, Sun Yang, Huang Qizhao and Zuo Lianrong.

I also want to express my gratefulness to all the lab officer in Department of Materials Science and Engineering, especially Chen Qun, Lim Mui Keow and Chan Yew Weng, for their kindly help in the use of equipment.

My profound thanks for the scholarship from National University of Singapore and from Singapore Ministry of Education (MOE), and research funding from the National Research Foundation, Prime Minister's Office, Singapore under its Competitive Research Programme (CRP Awards No. NRF-CRP 8-2011-4 and NRF-CRP 10-2012-6) and the Singapore Ministry of Education grant MOE2009-T2-1-065.

Last but not the least, my forever and deepest love and gratefulness to my father Chen Caijian, my mother Wu Xizhen, my sisters Chen Yanhua and Chen Yanping, and my fiancé Zhang Beiyu.

CONTENT

Declaration.....	i
Acknowledgements.....	ii
Summary.....	vi
List of Tables.....	viii
List of Figures.....	viii
List of Abbreviations.....	xiv
List of Symbols.....	xv
Chapter 1 Introduction.....	1
1.1 Lithium Secondary Batteries.....	1
1.2 All-solid-state Lithium Batteries.....	5
1.3 Solid Electrolytes.....	8
1.3.1 Overview.....	8
1.3.2 Lithium argyrodite electrolyte.....	12
1.4 Electrode Materials.....	16
1.4.1 Reversible energy storage mechanism.....	16
1.4.2 Overview of cathode materials.....	19
1.4.3 Copper sulfide.....	22
1.4.4 Sulfur.....	26
1.4.5 Molybdenum sulfide.....	31
1.5 Objectives and Significance of the thesis.....	35
Chapter 2 Experimental Details.....	38
2.1 Preparation of Lithium Argyrodites.....	38
2.2 Preparation of Various Composite Cathode Powders.....	38
2.2.1 Cu-Li ₂ S composite cathode powder.....	39

2.2.2	CuS composite cathode powder.....	39
2.2.3	Sulfur composite cathode powder.....	39
2.2.4	MoS ₂ composite cathode powder.....	39
2.3	Assembly of All-solid-state Lithium Batteries.....	39
2.4	Characterization Methods	41
2.4.1	X-ray Diffraction (XRD)	41
2.4.2	Neutron Powder Diffraction (NPD).....	42
2.4.3	Scanning Electron Microscopy (SEM)	42
2.4.4	Transmission Electron Microscopy (TEM)	42
2.4.5	Electrochemical Impedance Spectroscopy (EIS).....	43
2.4.6	Electrochemical cycling.....	44
Chapter 3	Properties of Lithium Argyrodites Li ₆ PS ₅ X	45
3.1	Phase formation during heat treatment.....	45
3.2	Conductivity vs. annealing temperature.....	51
3.3	Structure	54
3.4	Electrochemical stability	56
3.5	Morphology	57
3.6	Chemical stability.....	57
Chapter 4	All-solid-state Batteries Using CuS or Cu-Li ₂ S as Cathode.....	61
4.1	Effects of Original States of Composite Cathodes.....	61
4.1.1	Composite cathodes prepared by mortar grinding or ball milling	61
4.1.2	Battery assembly in charged or discharged state	67
4.2	Special Role of Cu ⁺ in ASSLBs.....	70
4.3	Capacity fading analysis.....	76
Chapter 5	All-solid-state S/Li ₆ PS ₅ Br/In-Li Batteries	80

Chapter 6	All-solid-state $\text{MoS}_2/\text{Li}_6\text{PS}_5\text{Br}/\text{In-Li}$ Batteries	91
Chapter 7	Conclusions and Outlook.....	98
Publication List		105
Journal Publication.....		105
Conference contributions		105
References.....		109

SUMMARY

This thesis aimed to design a high energy density all-solid-state lithium secondary batteries (ASSLBs) combining lithium argyrodite $\text{Li}_6\text{PS}_5\text{X}$ solid electrolyte with various sulfur-based composite cathode, including CuS , $\text{Cu-Li}_2\text{S}$, S and MoS_2 . The structure, electrochemical properties and accordingly preparation conditions of lithium argyrodites are explored in detail. ASSLBs based on lithium argyrodites solid electrolyte are optimized by exploring the reasons for the capacity fading of the batteries using various high capacity sulfur-based cathode materials.

Chapter 1 introduces ASSLBs and their components - solid electrolyte and electrode materials. Historical development and challenges of lithium secondary batteries using organic liquid electrolyte are reviewed. Replacing liquid electrolyte with solid electrolyte is a potential solution to realize lithium batteries with high safety, high cyclability and high energy density. Among all the known solid electrolytes, lithium argyrodites $\text{Li}_6\text{PS}_5\text{X}$ ($\text{X}=\text{Br}, \text{Cl}$) are promising due to relatively high ionic conductivity. In addition, sulfur-based conversion materials, including CuS , S and MoS_2 , show high capacity over conventional intercalation materials. By combining lithium argyrodite solid electrolyte with sulfur-based cathode materials, high energy density ASSLBs are expected.

Chapter 2 describes the details of preparing lithium argyrodites and various composite cathode powders of CuS , $\text{Cu-Li}_2\text{S}$, S and MoS_2 , and the way of assembling ASSLBs. Characterization techniques used in the study are also specified, including X-ray diffraction, neutron powder diffraction, scanning electron microscopy, transmission electron microscopy, electrochemical impedance spectroscopy and electrochemical cycling.

Chapter 3 presents the results of lithium argyrodites. In-situ neutron powder diffraction and impedance measurement reveal that lattice parameters, halide content and distribution, and consequently ionic conductivity vary with annealing temperature. A room temperature ionic conductivity of 1.1×10^{-3} S/cm was obtained. Based on this finding, preparation condition of lithium argyrodites is optimized. The resulting sample shows a high

electrochemical stability between 0-4 V and a high densification without distinct holes or gaps after pelletization.

Chapter 4 shows ASSLBs using $\text{Li}_6\text{PS}_5\text{Br}$ in combination with CuS or $\text{Cu-Li}_2\text{S}$ as cathode. Preparing composite cathode by ball milling instead of mortar grinding increases the initial discharge capacity of the ASSLB but not the reversible capacity, while batteries using $\text{Cu-Li}_2\text{S}$ cathodes show a slightly higher reversible capacity than those using CuS cathodes. However, all the ASSLBs present a fast capacity fading. Detailed investigations on ex-situ X-ray diffraction of CuS composite cathode at different discharge stages reveal a peculiar novel reaction mechanism, i.e. Cu^+ formed by the reduction of CuS at intermediate stages partially substitutes Li^+ in both lithium argyrodite $\text{Li}_6\text{PS}_5\text{Br}$ and Li_2S , leading to $\text{Cu}_y\text{Li}_{6-y}\text{PS}_5\text{Br}$ ($y_{\text{max}}=1.59$) and $\text{Cu}_z\text{Li}_{2-z}\text{S}$. The resulting mixed mobile ion effect is one of the reasons for the fast capacity fading.

Eliminating the negative role of Cu^+ in ASSLBs, all-solid-state $\text{S/Li}_6\text{PS}_5\text{Br/In-Li}$ batteries are prepared and examined, as discussed in Chapter 5. Sulfur composite cathodes are prepared by two-step high-energy ball milling, yielding a uniform mixture with a particle size smaller than 100 nm. The resulting batteries demonstrate an initial discharge capacity of 1355 mAh/g and reversible capacity of up to 1080 mAh/g after 50 cycles at C/10. No structural change of lithium argyrodite is observed after the long cycling.

Moreover, a novel type of all-solid-state Li/S batteries is achieved by the design and realization of all-solid-state $\text{MoS}_2/\text{Li}_6\text{PS}_5\text{Br/In-Li}$ batteries (see Chapter 6). Cyclic voltammetry and TEM confirm that these ASSLBs after the first full discharge of the MoS_2 cathode function as Li/S batteries with Mo nanoparticles of a size of ca. 7 nm finely dispersed in the composite cathode. At 70 °C the battery produced in this project exhibits a high rate capability up to 1C in comparison to existing ASSLBs (especially those with high capacity conversion cathodes) and a high capacity retention of 85% up to 700 cycles with a reversible capacity of 270 mAh/g at C/5.

Chapter 7 concludes this thesis and sketches promising directions for future work based on the results obtained in this project.

LIST OF TABLES

Table 1-1 Ionic conductivity and electronic conductivity of lithium argyrodite $\text{Li}_6\text{PS}_5\text{X}$ ($\text{X}=\text{Cl}, \text{Br}, \text{I}$). ⁸⁶	15
Table 3-1 Atomic coordinates, site occupancy factors (n) and isotropic atomic displacement parameters (Uiso) of $\text{Li}_6\text{PS}_5\text{Br}$ obtained from Rietveld refinement using XRD and neutron data.....	55

LIST OF FIGURES

Figure 1-1* Comparison of the various battery technologies in term of volumetric and gravimetric energy density (modified after Tarascon ¹).	2
Figure 1-2 Operating principles of lithium secondary batteries.	3
Figure 1-3* Schematic representation of the formation of lithium dendrite. ¹	4
Figure 1-4* ASSLBs are being considered to take the place of batteries with liquid electrolyte for electric vehicles, mobile equipment and stationary use due to higher safety, longer service life and higher energy density. ²⁸	7
Figure 1-5 Overview of progress in the development of Li^+ solid electrolytes. For comparison, the conductivity value for a typical liquid electrolyte is indicated as a horizontal broken line.	9
Figure 1-6 Dependence of the conductivity σ on temperature T for various Li^+ ion conducting solid sulfides and oxides shown as an Arrhenius plot $\log(\sigma T)$ vs. $1000/T$. ^{67,71} . The solid lines are curves of sulfide solid electrolytes, while the dash lines are curves of oxide solid electrolytes.	12
Figure 1-7 Structure model of $\text{Li}_6\text{PS}_5\text{Br}$. For the smaller spheres, the green ones stand for phosphorus atoms, and the yellow ones for sulfur atoms, while the blue ones mark the sites partially occupied by lithium atoms. The larger spheres represent the sites partially occupied by S and Br: the red ones are dominantly occupied by Br while the yellow ones by S.	14

Figure 1-8* A schematic representation of various reversible energy storage mechanisms in lithium-based batteries. Black circles: voids in the crystal structure; blue circles: metal elements; yellow: lithium; red: electrons. Modified from Palacin⁸⁷ and Zu et al.⁸⁸. 17

Figure 1-9 Calculated emf values of conversion reactions between selected binary transition metal compounds and lithium. Data were collected from the materials project database.^{113,114} 21

Figure 1-10* Behavior of high purity CuS electrode vs. lithium when using liquid electrolyte over five cycles between 1.5 and 2.6V range at room temperature.¹²⁸ 23

Figure 1-11* Schematic discharge reaction mechanism of Li/S batteries. The products Li_2S_8 , Li_2S_6 , Li_2S_4 are soluble in the liquid electrolyte.¹³⁶ 28

Figure 2-1 Schematic diagram of preparing the pellet of the respective composite cathode powder and the solid electrolyte using 13 mm pressing die set. 40

Figure 2-2 Schematic diagram of assembly of ASSLBs in Swagelok cell. 40

Figure 2-3 Schematic diagram of sealing of sample for ex-situ XRD measurement. 42

Figure 2-4 Equivalent circuits used to fit the impedance data. 43

Figure 3-1* (a) 2-D intensity color map of in-situ NPD pattern during the phase formation of $\text{Li}_6\text{PS}_5\text{Cl}$ from ball-milled precursors. The changes of color from blue to red represent the increase of intensity. The solid black line demonstrates the variation of temperature with time during the measurement. (b) Detailed NPD patterns at selective temperature extracted from in-situ NPD results in (a).¹⁷⁹ 46

Figure 3-2* Rietveld refinement results of NPD demonstrating the temperature dependences of (a) lattice parameter a , (b) Cl content x in the main argyrodite phase $\text{Li}_{7-x}\text{PS}_{6-x}\text{Cl}_x$, and (c) Cl distribution (fraction of Cl residing in position Cl(2) to total Cl in argyrodites). In all the figures, the red diamonds represent data during heating, while the blue triangles represent data during cooling.¹⁷⁹ The open squares in figure (a) are data from literature for $\text{Li}_{7-x}\text{PS}_{6-x}\text{Cl}_x$, low-temperature modification of Li_7PS_6 (LT- Li_7PS_6) and high-temperature modification of Li_7PS_6 (HT- Li_7PS_6), as denoted in the figure⁸⁰ 49

Figure 3-3 (a) 2-D intensity color map of in-situ XRD patterns during the phase formation of $\text{Li}_6\text{PS}_5\text{Br}$ from ball-milled precursors. The changes of color from blue to red represent the increase of intensity. (b) Rietveld refinement results of the samples at the beginning of

heating (50 °C), at the maximum temperature (250 °C) and at the end of cooling (50 °C).
..... 50

Figure 3-4* (a) Arrhenius plot of the ionic conductivity of Li₆PS₅Cl heating to various temperatures, i.e. 150 °C, 200 °C, and 250 °C, and their relevant cooling curves. For the heating curve, to avoid duplication, only the curve heating to 250 °C is shown. (b) Arrhenius plot of the ionic conductivity of Li₆PS₅Cl at the 2nd heating. The samples were annealed at different temperatures during the 1st heat treatment, i.e. 200 °C and 250 °C.¹⁷⁹
..... 52

Figure 3-5 Rietveld refinement of XRD data for Li₆PS₅Br (R_{wp} = 6.3%) 55

Figure 3-6 Cyclic voltammogram of Li/Li₆PS₅Br/stainless steel cell at a scanning rate of 2 mV/s between -0.5 V and 4 V. Inset: enlarged voltammogram in the current range -20 μA to 20 μA. 56

Figure 3-7 SEM image of a Li₆PS₅Br pellet 57

Figure 3-8 (a) Nyquist plots of the impedance data and (b) Arrhenius plot of the total ionic conductivity of the 10Li₆PS₅Br-ZnO sample. The frequency scale is 10 MHz to 5 kHz. 59

Figure 3-9 Nyquist plot of the 10Li₆PS₅Br-ZnO sample before exposure and after exposed to the air for 2 min and 5 min. The measurements were performed at room temperature with a frequency range of 10 MHz to 5 kHz. 60

Figure 4-1 SEM images of composite cathode powders prepared by (a) mortar grinding and (b) ball milling..... 62

Figure 4-2 (a) Charging and discharging curves and (b) discharge capacity of the first 20 cycles of all-solid-state Cu-Li₂S/Li₆PS₅Br/In batteries with composite cathodes prepared by mortar grinding and ball milling. The current density is 50 mA/g (C/10) and the voltage range is 0.65 V to 3.1 V vs. Li/Li⁺ (0.05 – 2.5 V vs. In-Li). 64

Figure 4-3 Discharge capacity of ASSLBs with composite cathodes prepared by mortar grinding and ball milling charged and discharged at various C rates, i.e. C/2, C/5, C/10, C/20 and C/50. The charge and discharge current was set to be the same and changed every 5 cycles..... 65

Figure 4-4 (a) Discharge curve of the battery using mortar-ground composite cathode during the cycling experiment shown in Figure 4-3; (b) Detailed cycling data for the

mortar-ground sample at C/10 rate (cycles 11-15) from the experiment as shown in Figure 4-3.	66
Figure 4-5 (a) Discharge and charge curves and (b) discharge capacity of ASSLB using ball-milled CuS cathode. The battery was cycled between 0.65 V and 3.1 V at a current density of 11.2 mA/g (C/50).	68
Figure 4-6 Comparison of discharge capacity of ASSLB using ball-milled CuS or Cu-Li ₂ S as cathode. Both batteries were cycled between 0.65 V and 3.1 V at a rate of C/10 at room temperature. Capacities of both batteries were calculated with respect to the weight of CuS.	69
Figure 4-7 XRD patterns of the cathode discharged to different capacity, i.e. 0, 100, 200, 300, 560 mAh/g (top to bottom).	71
Figure 4-8 (a) Rietveld refinement fitting plots of composite cathode discharged to 300 mAh/g as an example. (b) Correlation between the variation of copper content y of Cu _y Li _{6-y} PS ₅ Br and its cubic lattice (filled symbols). Open symbol refers to literature data for Cu ₆ PS ₅ Br.	72
Figure 4-9 Rietveld refinements results showing dependencies of weight fraction of Cu _y Li _{6-y} PS ₅ Br, CuS, Cu ₂ S, Cu _z Li _{2-z} S and Cu, and the copper content y of Cu _y Li _{6-y} PS ₅ Br on discharge capacity. The closed diamonds represent Li ₂ S, while the open diamond represents Cu _z Li _{2-z} S.	75
Figure 4-10 SEM images of the cross section of the cathode of the all-solid-state CuS/Li ₆ PS ₅ Br/In-Li battery (a) before cycling and after (b) 1 st discharge and (c) 1 st charge between 0.05V and 2.5V.	77
Figure 4-11 Rietveld refinements of the composite cathode after 20 cycles (discharged state) between 0.05V and 2.5V at C/10.	78
Figure 5-1 XRD patterns of pristine sulfur and ball-milled sulfur-carbon composite.	81
Figure 5-2 SEM images of (a) pristine sulfur, (b) pristine super P carbon, (c, d) ball-milled sulfur-carbon composite and (e, f) sulfur composite cathode powder after removing Li ₆ PS ₅ Br.	82
Figure 5-3 Cyclic voltammogram of the all-solid-state cell S/Li ₆ PS ₅ Br/In-Li in a voltage range of 1.0 to 3.0 V (vs. Li/Li ⁺) at a scanning rate of 0.02 mV/s. Top voltage axis shows the corresponding values of the voltage vs. In-Li.	84

Figure 5-4 Room temperature cyclic performance of the all-solid-state S/Li₆PS₅Br/In-Li cell up to 100 cycles in ambient atmosphere. The current density is 167 mA/g of active sulfur (corresponding to C/10). The voltage range is 1.0 to 3.0 V vs. Li/Li⁺. (a) Discharge-charge curves, (b) discharge/charge capacity and coulombic efficiency and (c) discharge depth of composite cathode during cycling based on discharge/charge capacity shown in (b)..... 86

Figure 5-5 (a) Discharge-charge curves, (b) discharge/charge capacity and coulombic efficiency of the all-solid-state S/Li₆PS₅Br/In-Li cell up to 50 cycles at room temperature. The current density was 167 mA/g of active sulfur (corresponding to C/10). The voltage range was 1.0 to 3.0 V vs. Li/Li⁺. The measurement was carried out in argon atmosphere. 87

Figure 5-6 Ex-situ XRD patterns of composite cathode before cycling and after 101st cycle (discharged state). 89

Figure 5-7 Discharge capacity of the all-solid-state cells using composite cathode mixture with various S contents, i.e. 20 wt%, 25 wt%, 30 wt% and 40 wt%. Here the discharge capacity is given with respect to the total weight of the composite cathode as a more direct measure for the energy density of cells based on these composites. Discharge capacity curves are shown only for the 1st, 10th, 15th and 20th cycle for clarity. The open symbols are data for the cell testing in the glove box (20 wt%). 90

Figure 6-1 SEM images of the pristine MoS₂ powder and the MoS₂ composite cathode powder after ball milling..... 92

Figure 6-2 Cyclic voltammogram of all-solid-state MoS₂/Li₆PS₅Br/In-Li cell at a scanning rate of 0.05 mV/s. The voltage range is 0.1-3.1 V vs. Li/Li⁺. 93

Figure 6-3 TEM results of the charged MoS₂ composite cathode powder after dissolving in DI water. Bottom left: SAED pattern of sample shown in the figure at the top left side. Right: HRTEM image. 94

Figure 6-4 (a) Discharge-charge curves and (b) cyclic behavior of the all-solid-state MoS₂/Li₆PS₅Br/In-Li cell at room temperature at a rate of C/10. The voltage range was 0.1-3 V (vs. Li/Li⁺) in the first 5 cycles and 1-3 V in the following cycles. 96

Figure 6-5 (a) Cycling behavior and (b) discharge curves of all-solid-state MoS₂/Li₆PS₅Br/In-Li cell at 70 °C. The voltage range was 0.1-3.1 V vs. (Li/Li⁺) at the first

cycle and 0.6-3.1 V in the following cycles. The discharge/charge rate changed every 200 cycles from C/5, C/2 to 1C and then back to C/5. 97

Figure 7-1 Theoretical and practical capacities of various cathode composite materials. The red columns of S and MoS₂ represent the practical capacity with respect to the amount of active material, while the blue columns represent the practical capacities with respect to the total weight of the composite cathode. The theoretical and practical capacities of LiCoO₂, LiFePO₄ and LiMn₂O₄ are taken from the literature. 102

* Copyright permissions for reproduction of these figures that are taken from the literature (and partially modified as needed for the discussion, sources are indicated in the captions) have been obtained from the respective copyright owners.

LIST OF ABBREVIATIONS

ASSLB	All-solid-state lithium battery
CV	cyclic voltammetry
DI water	Deionized water
GSAS	Generalized structure analysis system
HT	High temperature
LAGP	$\text{Li}_{1+x}\text{Al}_x\text{Ge}_{2-x}(\text{PO}_4)_3$
LGPS	$\text{Li}_{10}\text{GeP}_2\text{S}_{12}$
LIB	Lithium-ion battery
LiPON	$\text{Li}_{2.88}\text{PO}_{3.73}\text{N}_{0.14}$
LISICON	<u>L</u> ithium <u>S</u> uper <u>I</u> onic <u>C</u> onductor
LLT	Perovskite $\text{Li}_{3x}\text{La}_{2/3-x}\square_{1/3-2x}\text{TiO}_3$ (\square : A-site vacancies)
LLZ	$\text{Li}_7\text{La}_3\text{Zr}_2\text{O}_{12}$
LPS	glass-ceramic $\text{Li}_2\text{S-P}_2\text{S}_5$
LT	Low temperature
LTAP	$\text{Li}_{1+x}\text{Ti}_{2-x}\text{Al}_x(\text{PO}_4)_3$
NASICON	sodium (<u>N</u> a) <u>S</u> uper <u>I</u> onic <u>C</u> onductor
NPD	Neutron Powder Diffraction
PEO	Poly(ethylene oxide)
PMMA	Poly(methyl methacrylate)
rpm	Revolutions per minute
SAED	Selected area electron diffraction
SEI	Solid electrolyte interface
SEM	Scanning electron microscopy
TEM	Transmission electron microscopy
THF	Tetrahydrofuran
TM	Transition metal
XRD	X-ray Diffraction
Z'	Real part of impedance
Z''	Imaginary part of impedance

LIST OF SYMBOLS

σ	Conductivity
ρ	Density
E_a	Activation energy
k	Boltzmann constant
l	Thickness
M	Atomic weight
Q	Non-ideal double layer capacitance
r	Radius
R	Resistance
T	Temperature
U_{iso}	Isotropic atomic displacement parameters
W	Warburg impedance

Chapter 1 INTRODUCTION

Lithium-based secondary batteries are one of the most widely used energy storage systems due to their high specific energy density, high energy efficiency and long service life, etc. However, conventional lithium-ion batteries (LIBs) are suffering from high flammability and relatively low energy density due to the utilization of liquid electrolyte. One of the effective approaches is to substitute solid electrolyte for liquid electrolyte, leading to all-solid-state lithium secondary batteries (ASSLBs). ASSLB is composed of one solid electrolyte layer sandwiched between two electrodes (cathode and anode). Among all solid electrolytes reported so far, lithium argyrodites, $\text{Li}_6\text{PS}_5\text{X}$ ($\text{X}=\text{Cl}, \text{Br}, \text{I}$), with high ionic conductivity and electrochemical stability, have attracted considerable attention. In this project it has been explored how optimizing the processing of argyrodites and combining them with high-capacity sulfur-based electrode materials, including CuS , S and MoS_2 , can lead to high-performance ASSLBs.

In this chapter, section 1.1 will briefly introduce the operating principles and developing history of lithium secondary batteries. Section 1.2 will present the advantages and challenges of ASSLBs. Sections 1.3 and 1.4 will give an overview of known polymer, oxide and thiophosphate solid electrolytes (with a particular focus on argyrodites) and high capacity electrode materials (e.g. CuS , S , MoS_2), respectively. Section 1.5 will present the objectives, significance, scope and outline of the thesis.

1.1 Lithium Secondary Batteries

Tremendous energy consumption in modern society has alarmed the depletion of non-renewable energy sources (e.g. coal, oil and natural gases) and environment issues (e.g. air pollution and global climate warming). Consequently, renewable energy has attracted considerable attention as alternative solutions. Since most of the renewable energy sources, e.g. solar energy and wind energy, are intermittent, exploration of energy storage system with high specific power density, high energy efficiency, long service life and high stability and reliability are heavily required. Besides, the aim to achieve a transition to a more sustainable transport system based on electric vehicles and the constantly growing need for

portable electronic devices (such as mobile phones, laptops and MP3 etc.) further highlight the utmost importance of high-performance energy storage systems.

Among all the metals, lithium has the lightest specific weight (atomic weight $M=6.94$ g/mol and density $\rho=0.53$ g/cm³) and lowest voltage of -3.04V versus standard hydrogen electrode. Since the energy density of a battery is decisively influenced by its weight and potential, lithium secondary batteries show distinctly higher volumetric and gravimetric energy density than conventional batteries like lead-acid batteries, Ni-Cd batteries and Ni-MH batteries as shown in Figure 1-1¹, and are undoubtedly one of the most promising energy conversion and storage systems.

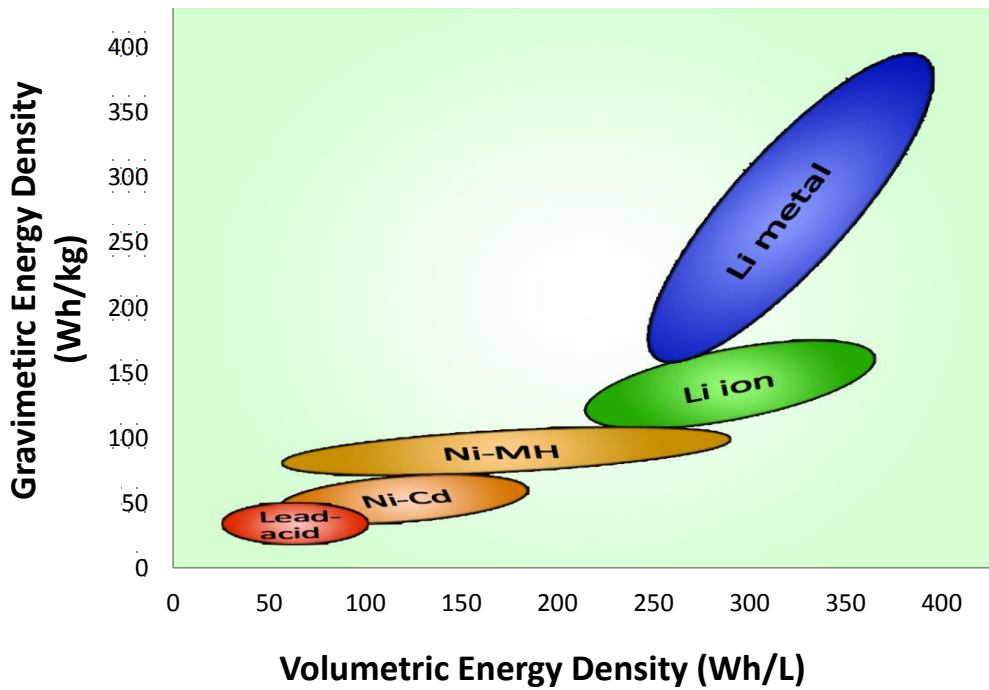


Figure 1-1 Comparison of the various battery technologies in term of volumetric and gravimetric energy density (modified after Tarascon¹).

A lithium secondary battery converts chemical energy into electrical energy and vice versa with Li^+ as the mobile charge carrier.² As shown in Figure 1-2, a lithium secondary battery is generally composed of three parts: cathode, electrolyte and anode. The electrolyte is an ionically conductive but electronically insulating material, thus separating the ion transport through the cell from electron transport through the external circuit. The anode is the source of lithium ions, while the cathode is the sink for lithium ions during discharge, and vice

versa during charge. To allow for the transfer from ionic to electronic transport not only at a two-dimensional electrode:electrolyte interface but also within the electrode material, the electrodes should conduct both electrons and lithium ions, i.e. they should be mixed (electronic and ionic) conductors.

During discharge, lithium ions would be transferred through the electrolyte from the anode to the cathode, while the electrons would flow through the external circuit to conduct work. During charge, lithium ions would go back to the anode, thus converting the electrical energy into chemical energy for storage.

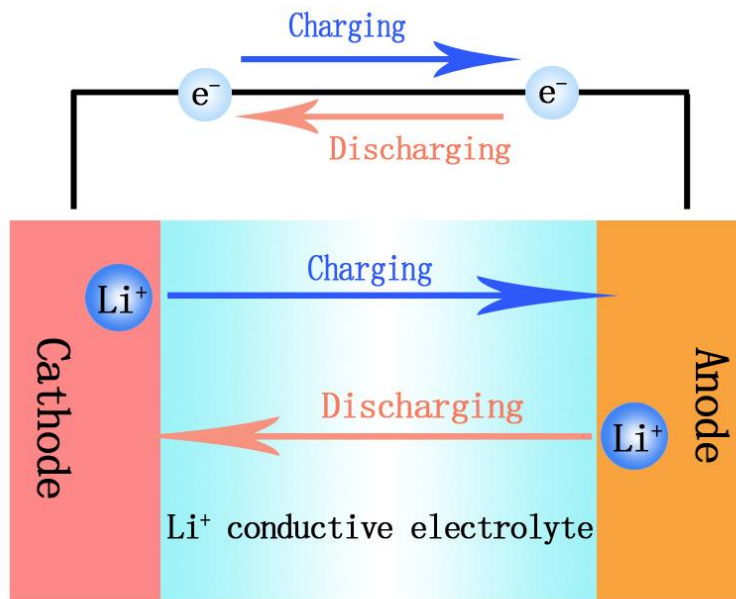


Figure 1-2 Operating principles of lithium secondary batteries.

The first lithium battery was proposed by Whittingham et al.^{3,4} in 1970s by using TiS₂ as cathode, Li as anode and lithium perchlorate in dioxolane as the electrolyte. In 1980, Goodenough developed a lithium secondary battery with LiCoO₂ as cathode and lithium foil as anode.^{5,6} This family of cathode compounds LiMO₂ (M=Co, Mn, Ni) had a high cell voltage in 4V range and is still widely used in today's batteries. However, application of such batteries was limited due to the use of metallic lithium. Metallic lithium would react with the liquid electrolyte, forming a passivation layer of decomposition products on the surface during charging, which led to non-uniform plating of lithium and formation of

dendritic lithium with prolonged deposition/dissolution cycling, as sketched in Figure 1-3.¹ The dendritic lithium might grow through the electrolyte, connect the anode to the cathode and thus cause short circuit. Therefore, the batteries using liquid electrolyte and lithium anode always suffer from poor safety and cyclability.

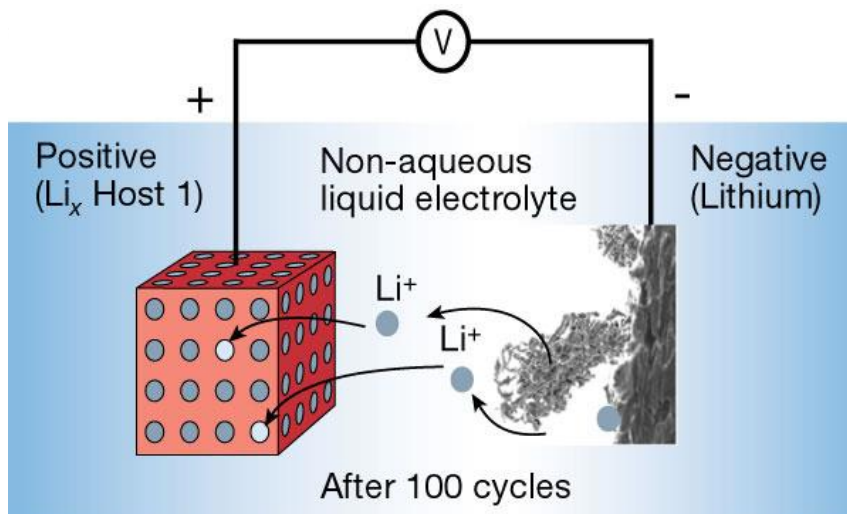


Figure 1-3 Schematic representation of the formation of lithium dendrite.¹

To address the issue of dendritic lithium formation, Armand proposed a rocking chair concept, i.e. replacing the metallic lithium anode by a second insertion material with a lower standard electrochemical potential than positive insertion electrode.^{7,8} Since both of the electrodes are lithium insertion materials, lithium-ions “rock” between cathode and anode upon charging and discharging, resulting in a “lithium-ion battery” (LIB) or “rocking chair battery”. Such proposal signified various intercalation-type anode materials, such as graphite. Actually, electrochemical intercalation of Li⁺ into graphite in organic solution has been discovered by Besenhard et al.⁹ in 1974. Later in 1976 they proposed the application of graphite in lithium batteries, which however suffered from the decomposition of liquid electrolyte in contact with graphite during charging.¹⁰ In 1980s, Yazami et al.¹¹ demonstrated the plausibility of reversible electrochemical intercalation of Li⁺ in graphite by using solid electrolyte instead of unstable liquid electrolyte. Hitherto, graphite anode is still the most commonly used negative electrode materials in commercial LIBs. In 1985, Yoshino et al.¹² designed a prototype cell combining LiCoO₂ cathode with graphite anode, based on which Sony released the first commercial LIB in 1991. Thereafter, LIBs were widely used throughout the world and soon dominated the market of conventional batteries.

However, it remains one of the key challenges for a penetration of LIBs into large-scale application that the reliance on flammable organic liquid electrolytes raises safety concerns and limits cyclability. Therefore, although development of automotive and stationary loading-leveling places a strong demand on large-scale lithium secondary batteries, hitherto LIBs are far from meeting the necessary safety and performance criteria. To mitigate these challenges originating from the organic liquid electrolyte, gel electrolyte was proposed as a way to trap the liquid electrolyte in a porous polymer matrix.¹³ Benefiting from the polymer entangling component, the resulting membrane shows a free-standing appearance in spite of the existence of the liquid electrolyte, thus reducing possibility of the leakage of the flammable liquid. On the other hand, the liquid electrolyte trapped within the pores of the polymer can promise a high ionic conductivity of the membrane comparable to that of individual liquid electrolyte.¹⁴ However, such trapping is still unable to eliminate the safety and cyclability issues raised by liquid electrolyte. A more radical solution is to replace liquid electrolyte by solid electrolyte, leading to ASSLBs, which will be reviewed in the following section (section 1.2).

1.2 All-solid-state Lithium Batteries

The term all-solid-state battery is used when all the components of a cell (i.e. cathode, electrolyte and anode) are solid. The most important aspect of this concept is the employment of solid electrolyte in replacement of liquid electrolyte, considering that most of the electrode materials commonly used in batteries are already solid. Traced back to the earlier 20th century, silver ion solid conductors have been explored.^{15,16} Based on these silver ion conductors, in 1950s several all-solid-state battery systems were realized, such as Ag/AgI/V₂O₅, Ag/AgBr/CuBr₂, Ag/AgCl/KICl₄, despite that the ionic conductivity of these silver-based solid electrolyte was quite low with a maximum room temperature value of 10⁻⁶ S/cm (AgI). While the ionic conductivity was drastically increased to 0.26 S/cm (RbAg₄I₅)¹⁷ in 1960s and fast Ag⁺-ion conducting glasses¹⁸ were intensely investigated in the 1970s – 1990s, the commercial viability of all-solid-state silver batteries were greatly limited because of the intrinsic low energy density and high cost of silver materials. Alternatively, all-solid-state lithium batteries (ASSLBs) were investigated. In 1972, all-solid-state Li/LiI/I₂ battery was already commercially applied as power sources for

pacemaker. Also in 1970s, lithium solid polymer electrolyte batteries were developed.¹⁹ However, at that time no Li^+ ion conducting solids with sufficiently high ionic conductivities and stability were known, so that the power performance of such ASSLBs was extremely limited.

In general, ASSLBs have some advantages over conventional LIBs using liquid electrolyte. One lies in their superior safety. Conventional LIBs intrinsically suffered from safety issues since liquid electrolytes normally contain combustible and corrosive solvent. Once leaking, it may catch fire. Besides, the battery may spontaneously heat up further (thermal runaway) leading to fire or even explosion, when the battery temperature exceeds a safe range due to overcharging, short circuit or external heating. In contrast, inorganic solid electrolytes are typically non-flammable, and can prevent short circuits by establishing a mechanical barrier separating the electrodes. As a result, the safety issue could be minimized.

Second, ASSLBs generally have higher reliability and have the potential to achieve longer cycle life. Solid electrolytes conduct only Li^+ ions²⁰, while liquid electrolytes allow not only Li^+ ions but also associated counter anions and molecules of the solvents passing through. These mobile species would diffuse to the surfaces of the electrodes and cause side reactions, leading to self-discharge and formation of passivation layer at the electrode/electrolyte interfaces (solid electrolyte interface).²¹ As for inorganic solid electrolytes, by limiting mobile agents to only Li^+ ions, side reaction hardly occurs in solid-state systems. As a result, remarkably long cycle life could be achieved. Jones, et al. managed to make a thin-film solid-state Li/TiS_2 battery cycling over 21000 cycles with only a 20% loss in cathode efficiency.²²

Last but not the least, all-solid-state lithium secondary batteries enlarge the selection of electrode materials. Products of some kinds of electrode materials, e.g. polysulfides^{23,24}, are soluble to liquid electrolyte and may even diffuse to the surface of the other electrode, resulting in rapid fading of capacity or the failure of the battery. Such phenomena restrict the application of some promising electrode materials. Nevertheless, due to the impermeability of solid electrolyte to polysulfides, the formation of soluble polysulfides is not a problem in all-solid-state lithium sulfur batteries. In Addition, various solid electrolytes are electrochemically stable over a wide potential range (“electrochemical

window”) so that they can be combined with high voltage cathode materials (e.g. LiCoPO_4 ²⁵, $\text{LiNi}_{0.5}\text{Mn}_{1.5}\text{O}_4$ ²⁶, etc.), which can boost the voltage and hence the energy density of batteries using standard (e.g. graphite) anodes. In contrast, liquid electrolytes generally suffer from limited cyclability due to the relatively narrow electrochemical window of liquid electrolytes and the faster kinetics of side reactions therein. Since the electrochemical windows of most solid electrolytes are wider than liquid electrolyte²⁷, ASSLBs show great potential to employ 5 V cathode materials.

Due to the advantages mentioned above, ASSLBs have attracted considerable attention, especially for electric vehicles, portable electronic equipment and electric stationary use, as shown in Figure 1-4²⁸.

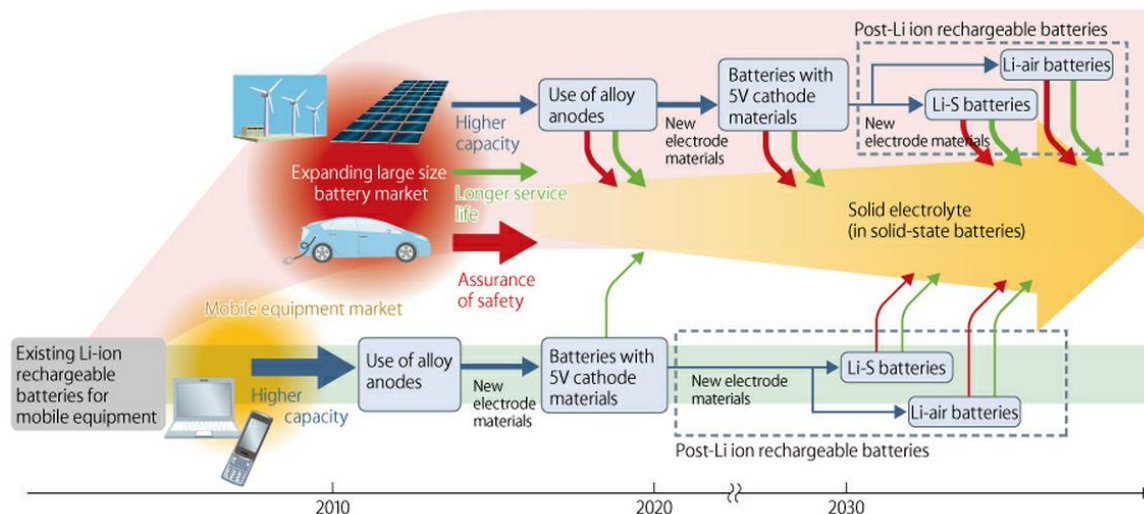


Figure 1-4 ASSLBs are being considered to take the place of batteries with liquid electrolyte for electric vehicles, mobile equipment and stationary use due to higher safety, longer service life and higher energy density.²⁸

However, some challenges need to be overcome for the commercial viability of a wider range of ASSLBs. One is caused by the limited ionic conductivity of solid electrolytes. Since the ionic conductivity of most solid electrolytes is low compared to that of liquid electrolytes, high internal resistance of ASSLBs limits their power performance. To overcome this issue, thin film batteries were realized previously, whose internal resistance decreased due to the reduction of the thickness of the solid electrolyte. The current market for ASSLBs therefore consists of niche segments such as Radio-frequency identification (RFID), medical, or remote sensor applications totaling US\$ 138 M in 2011.²⁹ Working at

non-ambient temperature could also improve the power performance of the batteries because of the increase of ionic conductivity of solid electrolyte with temperature. While this may be viable for large scale systems, the requirement to heat batteries to temperatures above ambient temperature effectively prevents the wide-spread use of such batteries for consumer applications (such as portable devices). A fundamental solution for this issue is to improve the ionic conductivity of the solid electrolytes, which has been studied for decades. It is expected that the use of fast ion conducting solids can render more powerful ASSLBs (for electric vehicles and as buffers for intermittent power supplies from renewable sources) possible, boosting the market to US\$ \$3.9 billion in 2018.²⁹ Some electrolytes with high ionic conductivity were fabricated recently, which would be discussed later in section 1.3.

Another challenge lies in the interface between electrode and electrolyte. The contact of the solid electrode with a solid electrolyte is normally worse than that with liquid electrolyte. Therefore, interface resistances are more critical for ASSLBs, limiting the power performance of batteries. What's more, if the electrode materials experiences significant volume changes during cycling, they may even lose electrical contact with the surrounding particles and become electrochemically inactive, leading to capacity fading of the all-solid-state lithium secondary batteries.

Concerning that solid electrolyte and electrodes (cathode and anode) are the main components of ASSLBs, more details on solid electrolyte and electrode materials will be reviewed in sections 1.3 and 1.4, respectively.

1.3 Solid Electrolytes

1.3.1 Overview

Solid electrolyte with high lithium ionic conductivity, low electronic conductivity and high electrochemical stability has been a limiting factor for developing high performance ASSLBs. Over the past several decades, there has been an ongoing research on solid electrolytes. In 1970s, lithium nitride (Li_3N), which has a high ionic conductivity of 6×10^{-7}

³ S/cm at room temperature, was discovered, but then found to be electrochemically unstable.^{30,31} Afterwards, various systems were studied, as shown in Figure 1-5.

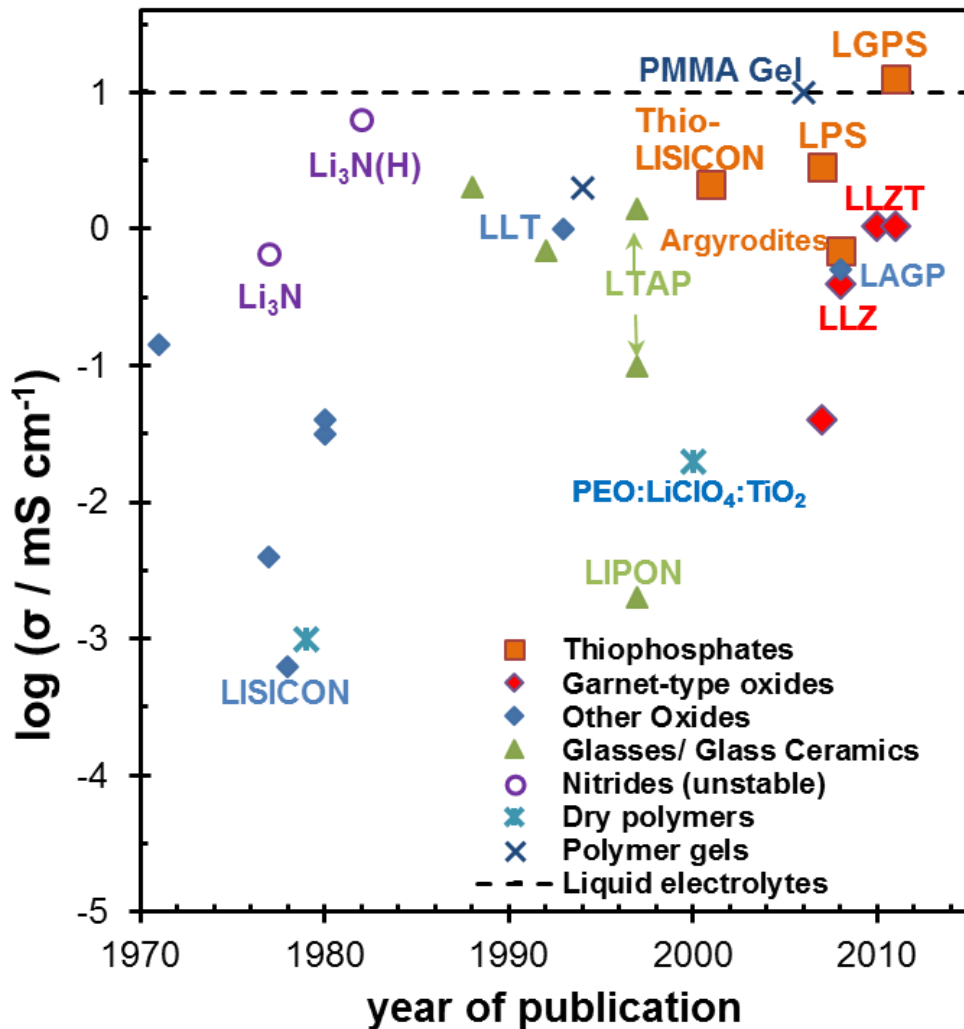


Figure 1-5 Overview of progress in the development of Li⁺ solid electrolytes. For comparison, the conductivity value for a typical liquid electrolyte is indicated as a horizontal broken line.

1) Solid polymers

Polymers are easier to process and have lower elastic moduli than ceramic solid electrolytes, thus could reduce the fabrication cost and are capable for flexible battery design.

The most commonly used “solid” polymer is poly(ethylene oxide) (PEO). PEO is a semicrystalline polymer with glass transition temperature around -60 °C and melting pointing around 65 °C.³² Above its glass transition temperature, by solvating various

lithium salt as lithium conduction media, PEO can be converted into a Li⁺ ion conductor. Examples of suitable lithium salts with weakly coordinating anions are lithium perchlorate LiClO₄^{33, 34}, lithium bis(oxalato)borate LiB(C₂O₄)₂ (LiBOB)³⁵, lithium trifluoromethanesulfonate LiCF₃SO₃ (LiTf)³⁶ and lithium bis(trifluoromethanesulfon)imide Li(CF₃SO₂)₂N (LiTFSI)³⁷. However, due to the semicrystalline nature of PEO, long range segmental motion of the chain is limited, leading to relatively low conductivity at room temperature (<10⁻⁶ S/cm). Adding a plasticizer, such as succinonitrile (SN)³⁸, polysquarate (PPS)³⁹ or ethylene carbonate (EC)/propylene carbonate (PC)⁴⁰, could reduce the crystallinity. Besides, adding ceramic fillers such as alumina⁴¹, silica⁴² or titania⁴³, not only helps to reduce crystallinity but also tends to enhance the ionic conductivity by space charge effects at the polymer-ceramic interface. Moreover, weakening the interaction between polymer chains and lithium ions, by adding weakly coordinating ionic liquid⁴⁴ or co-polymer⁴⁵, is an alternative way to increase ionic conductivity.

Alternative solid polymers to PEO have been developed recently. Most of them contain ethylene oxide units, e.g. poly(ethyleneglycol) (PEG)⁴⁶, poly(ethylene oxide) methylether methacrylate (PEOMA)⁴⁷ and tri(ethylene glycol) diacrylate (TEGDA)⁴⁸. Comparable conductivity to PEO-based electrolyte could be obtained. However, in spite of considerable studies focusing on exploring solid polymer-based electrolytes with practically high ionic conductivity, little progress has been achieved over the past decades. So far, the ionic conductivities of these electrolytes are still too low for practical use, which seriously limits their commercial viability.

2) Inorganic oxide electrolytes

Inorganic oxide materials typically have a high chemical stability towards polar solvent like water, which extends their potential application to aqueous lithium batteries and lithium air batteries. Meanwhile, given their non-reactivity in contact with O₂ or H₂O, the fabrication, storage and application of oxide solid electrolytes could be conducted in ambient air instead of an inert atmosphere, thus simplifying requirement for processing environment and hence reducing processing costs.

Based on crystal structures, inorganic oxide electrolytes includes “Perovskite” $\text{Li}_{3x}\text{La}_{2/3-x}\square_{1/3-2x}\text{TiO}_3$ (\square : A-site vacancies), Lithium-analogues of “NASICON” incl. $\text{LiM}_2(\text{PO}_4)_3$ ($\text{M}^{\text{IV}}=\text{Ge}, \text{Ti}, \text{Hf}$ and Zr), “LISICON” incl. $\text{Li}_{14}\text{ZnGe}_4\text{O}_{16}$ ^{49,50} and “Garnet” $\text{Li}_x\text{La}_3\text{M}_2\text{O}_{12}$ ($\text{M}=\text{Zr}, \text{Nb}, \text{Ta}, \text{Sb}, \text{Bi}$)⁵¹. Perovskite-type electrolytes have attracted considerable attentions due to a high ionic conductivity of 10^{-3} S/cm for single crystal.⁵² Nevertheless, Ti^{4+} tends to be reduced when contacting with Li metal, leading to increase of electronic conductivity.⁵³ Similar phenomenon could be seen on Ti-based NASICON, e.g. $\text{LiTi}_2(\text{PO}_4)_3$. Among all the garnet-type conductors, $\text{Li}_7\text{La}_3\text{Zr}_2\text{O}_{12}$ (LLZ), reported by Murugan et al.⁵⁴, exhibits the highest conductivity, though later it was found that doping is essential to maintain cubic fast-ion conducting phase instead of the less conductive tetragonal phase with an ordered Li distribution.^{55,56,57}

Besides crystalline oxides, inorganic oxide glass, e.g. “LiPON”, has been studied as well. With a typical composition of $\text{Li}_{2.88}\text{PO}_{3.73}\text{N}_{0.14}$, LiPON shows a room temperature ionic conductivity of 3.3×10^{-6} S/cm and activation energy of 0.54 eV.⁵⁸ Despite of this moderate conductivity, LiPON is widely used as solid electrolyte in thin-film batteries, taking advantage of preparation by sputtering.⁵⁹ Nevertheless, the preparation method in turn also prevents the application of LiPON in bulk batteries due to the prohibitively high cost.

3) Inorganic sulfide electrolytes

Among all solid electrolytes, inorganic sulfide electrolytes appear particularly promising for battery application due to their comparatively high ionic conductivity. Examples are glass or glass-ceramic $\text{Li}_2\text{S}-\text{P}_2\text{S}_5$ ^{60,61,62,63} including $\text{Li}_7\text{P}_3\text{S}_{11}$ ⁶⁴, “thio-LISICON” $\text{Li}_2\text{S}-\text{GeS}_2-\text{P}_2\text{S}_5$ ^{65,66}, $\text{Li}_{10}\text{GeP}_2\text{S}_{12}$ ^{67,68,69}, and Argyrodites $\text{Li}_6\text{PS}_5\text{X}$ ($\text{X}=\text{Cl}, \text{Br}$). As indicated in Figure 1-6, thiophosphates possess conductivities several orders of magnitude higher than those of solid oxides at room temperature, which renders them suitable as solid electrolyte of lithium secondary batteries. In 2011, Kamaya et al.²⁷ reported a new lithium superionic conductor $\text{Li}_{10}\text{GeP}_2\text{S}_{12}$ of 12×10^{-3} S/cm, comparable to that of liquid electrolyte (generally of the order of 10^{-2} S/cm at room temperature⁷⁰). Recently, Seino et al.⁷¹ reported a $\text{Li}_2\text{S}-\text{P}_2\text{S}_5$ glass-ceramic conductor with the highest conductivity ever achieved among solid electrolytes of 17×10^{-3} S/cm, by reducing grain boundary using heat treatment after

pelletization. In my thesis, I am focusing on lithium argyrodites. More details will be presented in section 1.3.2 and Chapter 3.

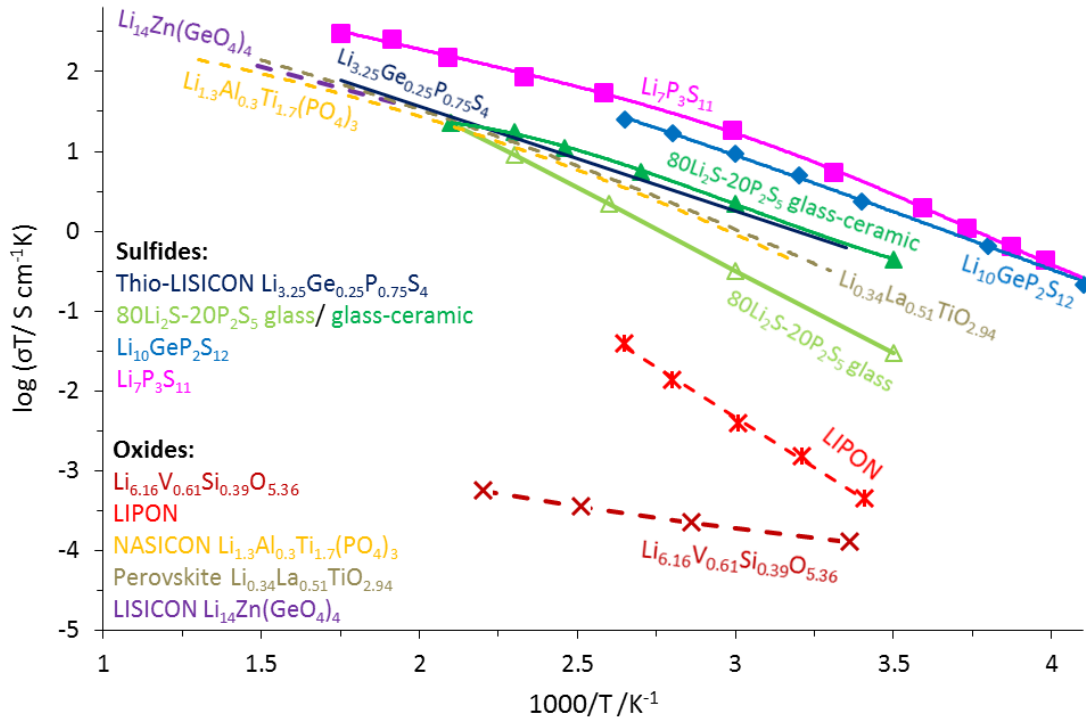


Figure 1-6 Dependence of the conductivity σ on temperature T for various Li^+ ion conducting solid sulfides and oxides shown as an Arrhenius plot $\log(\sigma T)$ vs. $1000/T$.^{67,71,72} The solid lines are curves of sulfide solid electrolytes, while the dash lines are curves of oxide solid electrolytes.

1.3.2 Lithium argyrodite electrolyte

As will be discussed more in detail below, lithium argyrodites $\text{Li}_6\text{PS}_5\text{X}$ ($\text{X}=\text{Cl}, \text{Br}$) are among the more promising solid electrolyte candidates introduced above (section 1.3.1). In my study, I will therefore focus on the application of argyrodites $\text{Li}_6\text{PS}_5\text{X}$ as the solid electrolyte in ASSLBs.

Argyrodites, named after natural mineral Ag_8GeS_6 ^{73,74}, are a large family of compounds with the general chemical formula $A_{(12-n-x)/m}^{m+}B^{n+}X_{6-x}^{2-}Y_x^-$ ($A=\text{Li}, \text{Cu}, \text{Ag}, \text{Cd}, \text{Hg}$; $B=\text{Ga}, \text{Si}, \text{Ge}, \text{Sn}, \text{P}, \text{As}$; $X=\text{O}, \text{S}, \text{Se}, \text{Te}$; $Y=\text{Cl}, \text{Br}, \text{I}$; $0 < x < 1$), where $m+$ and $n+$ are the valences of cations A and B , respectively.⁷⁵ The argyrodite structures share a common high-temperature structure (aristotype structure) in the faced-center-cubic space group $F-43m$ (that is e.g. realized at room temperature for $\text{Ag}_8\text{SnS}_6\text{Br}$ ^{76,77}) that is characterized by a

disorder of A-type cations (e.g. for $\text{Cu}_6\text{PS}_5\text{Br}$ 24 Cu per unit cell are reported to be evenly distributed over 96 sites), resulting in high ionic conductivity and low activation energy.

At lower temperatures the A ions partially or completely order leading to various lower symmetry phases, e.g. cubic $P2_13$ (e.g. $\text{Ag}_6\text{PSe}_5\text{X}^{76}$, $\text{Ag}_7\text{PSe}_6^{78}$), orthorhombic ($\text{Cu}_8\text{GeS}_6^{79}$ of $Pmn2_1$, $\text{Li}_7\text{PS}_6^{80}$ of $Pna2_1$), or monoclinic (e.g. $\text{Cu}_6\text{PS}_5\text{I}^{81}$ of Cc). Because of the ordering of the A cations in these low temperature (LT) phases, the ionic conductivity is greatly reduced compared to that of the HT modification.

Copper argyrodites ($\text{Cu}_6\text{PS}_5\text{X}$) are one of the representative compounds of argyrodites and have been intensively studied. At room temperature, crystalline structure of $\text{Cu}_6\text{PS}_5\text{X}$ belongs to HT-argyrodite with the space group of $F-43m$. The lattice parameters of $\text{Cu}_{7-x}\text{PS}_{6-x}\text{Cl}_x$, $\text{Cu}_{7-x}\text{PS}_{6-x}\text{Br}_x$, $\text{Cu}_{7-x}\text{PS}_{6-x}\text{I}_x$ are 9.687(2), 9.728(1) and 9.787(2), respectively.^{82,76,83} $\text{Cu}_6\text{PS}_5\text{X}$ exhibited high room temperature ionic conductivity of 4.7×10^{-4} S/cm for $\text{Cu}_6\text{PS}_5\text{Cl}$, 3.6×10^{-6} S/cm for $\text{Cu}_6\text{PS}_5\text{Br}$ and 2.0×10^{-4} S/cm for $\text{Cu}_6\text{PS}_5\text{I}^{76,83}$. At room temperature the electronic contribution to conductivity is small (<1% of ionic conductivity). Therefore, $\text{Cu}_6\text{PS}_5\text{X}$ is considered as an ionic conductor at room temperature. However, with the increase of temperature, electronic conductivity increases rapidly, and become equal to ionic conductivity at 300 °C for $\text{Cu}_6\text{PS}_5\text{Cl}$, 250 °C for $\text{Cu}_6\text{PS}_5\text{Br}$ and 150 °C for $\text{Cu}_6\text{PS}_5\text{I}^{76}$.

Lithium argyrodites $\text{Li}_6\text{PS}_5\text{X}$ were first reported by Deiseroth et al.^{84,80} Due to the similarity in the radii of Cu^+ and Li^+ ($\text{Cu}^+=74$ pm, $\text{Li}^+=73$ pm; all coordination number =4), lithium argyrodites can be derived simply by substituting copper in copper argyrodites by lithium, leading to the general formula $\text{Li}_{7-\delta}\text{PS}_{6-\delta}\text{X}_\delta$ ($\text{X}=\text{Cl}, \text{Br}, \text{I}$; $0 < \delta \leq 1$) with the space group of $F-43m$. The lattice parameters are 9.859(2) Å for $\text{Li}_{7-\delta}\text{PS}_{6-\delta}\text{Cl}_\delta$, 9.988(2) Å for $\text{Li}_{7-\delta}\text{PS}_{6-\delta}\text{Br}_\delta$ and 10.1448(16) Å for $\text{Li}_{7-\delta}\text{PS}_{6-\delta}\text{I}_\delta$, which are slightly larger than the corresponding $\text{Cu}_{7-x}\text{PS}_{6-x}\text{X}_x$.⁸⁰ The structure model of $\text{Li}_6\text{PS}_5\text{Br}$ is shown in Figure 1-7. Four P and sixteen S form four PS_4 tetrahedra, while the remaining S and Br then share the 4a (0, 0, 0) and 4d ($\frac{3}{4}, \frac{3}{4}, \frac{3}{4}$) anion positions. Twenty-four Li atoms are continuously distributed over the 48h-24g-48h site triplet with an occupancy maximum at the central 24g sites. A similar structure was observed for $\text{Li}_6\text{PS}_5\text{Cl}$. In contrast, $\text{Li}_6\text{PS}_5\text{I}$ is fully ordered, i.e. iodine and sulfur atoms occupy separate crystallographic positions. Such

difference in order/disorder could be attributed to the significantly different ionic radii of I^-/S^{2-} pair (I^- : 220 pm; S^{2-} : 184 pm), compared to that of $\text{Cl}^-/\text{S}^{2-}$ pair (Cl^- : 181 pm) and $\text{Br}^-/\text{S}^{2-}$ pair (Br^- : 196 pm). Measurements of ionic conductivity of $\text{Li}_6\text{PS}_5\text{I}$ yielded a relatively low value of 3.6×10^{-7} S/cm.

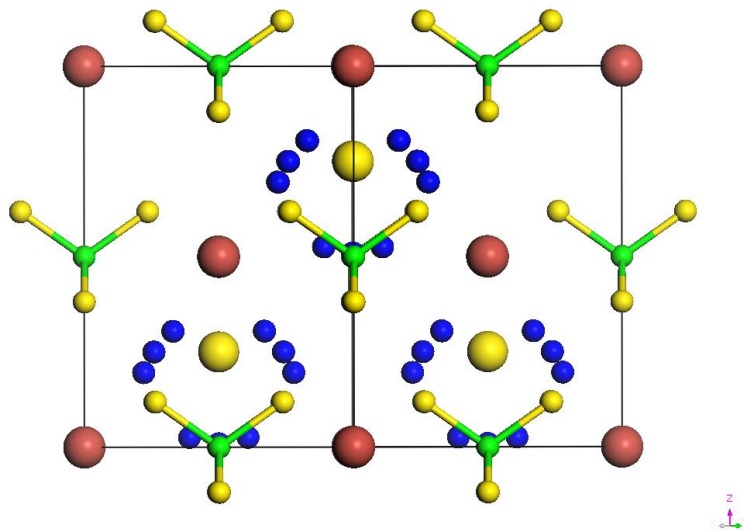


Figure 1-7 Structure model of $\text{Li}_6\text{PS}_5\text{Br}$. For the smaller spheres, the green ones stand for phosphorus atoms, and the yellow ones for sulfur atoms, while the blue ones mark the sites partially occupied by lithium atoms. The larger spheres represent the sites partially occupied by S and Br: the red ones are dominantly occupied by Br while the yellow ones by S.

The pioneering studies done by Deiseroth et al. shed light on the structure of lithium argyrodites and provide a clear description on differences among various argyrodites. However, due to the similar scattering length of Cl and S in X-ray diffraction experiments, no quantitative information on Cl/S occupancies was available when our study started. Similarly, information on the lithium atom distribution was also limited due to low X-ray scattering power. Taking the significantly different neutron scattering length of S from halide elements (Cl, Br, I), and the stronger contribution of Li atoms, neutron powder diffraction experiments on argyrodites should provide more information on structural details relevant to the ion transport mechanism. Moreover, optimizing fabrication of argyrodites has yet to be done.

In 2010, Stadler et al.⁸⁵ reported that lithium argyrodites $\text{Li}_6\text{PS}_5\text{Cl}$ and $\text{Li}_6\text{PS}_5\text{Br}$ have high ionic conductivity, low electronic conductivity and wide electrochemical window up to 5

V, while $\text{Li}_6\text{PS}_5\text{I}$ shows relatively low ionic conductivity and electrochemical instability around 2.79 V corresponding to the oxidation of LiI. The ionic conductivity and electronic conductivity of lithium argyrodite $\text{Li}_6\text{PS}_5\text{X}$ (X=Cl, Br, I) as reported was shown in Table 1-1. All-solid-state LTO/ $\text{Li}_6\text{PS}_5\text{Br}$ /Al-Li was prepared as well, yet showing high overpotential and poor cyclic performance at room temperature at C/10. At non-ambient temperature, e.g. 75 °C, the battery worked better with an initial discharge capacity of 150 mAh/g and reversible capacity of 90 mAh/g after 30 cycles at C/50. The poor performance of the batteries, in spite of the high ionic conductivity of $\text{Li}_6\text{PS}_5\text{Br}$, placed a strong demand on more studies on ASSLBs using $\text{Li}_6\text{PS}_5\text{X}$ as solid electrolyte. It should be noted that when I started my project, no other ASSLB based on $\text{Li}_6\text{PS}_5\text{X}$ as solid electrolyte had been reported.

Table 1-1 Ionic conductivity and electronic conductivity of lithium argyrodite $\text{Li}_6\text{PS}_5\text{X}$ (X=Cl, Br, I).⁸⁵

Compound	Ionic conductivity (S/cm)	Electronic conductivity (S/cm)
$\text{Li}_6\text{PS}_5\text{Cl}$	3×10^{-4}	$<3 \times 10^{-10}$
$\text{Li}_6\text{PS}_5\text{Br}$	1×10^{-4}	$<5 \times 10^{-10}$
$\text{Li}_6\text{PS}_5\text{I}$	4×10^{-7}	$<3 \times 10^{-10}$

More details on the structure and fabrication of lithium argyrodites will be discussed in Chapter 3. The applications in ASSLBs will be investigated in Chapters 4, 5 and 6.

It is noted that lithium oxide argyrodites $\text{Li}_6\text{PO}_5\text{X}$ have been investigated by Kong et al.⁸⁶ as well, with the same space group $F-43m$ but smaller lattice parameter. Despite of the similar structure, the room temperature ionic conductivity of $\text{Li}_6\text{PO}_5\text{X}$ is 2- 6 orders of magnitude smaller than that of $\text{Li}_6\text{PS}_5\text{X}$. For instance, the room temperature ionic conductivity of $\text{Li}_6\text{PO}_5\text{Cl}$ is only 10^{-9} S/cm. In accordance, the activation energy is as high as 0.66 eV. The low ionic conductivity and high activation energy of $\text{Li}_6\text{PO}_5\text{X}$ limit their potential as solid electrolytes for ASSLBs, though partial substitution of S by O may improve the chemical stability of argyrodites. The structure of arsenic-containing lithium argyrodites $\text{Li}_6\text{AsS}_5\text{X}$ have been reported as well, yet without any detail on their electrical

or electrochemical property.⁸⁰ The high toxicity of As anyways limits the application of such kind of compounds.

1.4 Electrode Materials

Whatever the employed battery technology, performance of a battery like cell potential, specific capacity and specific energy density, are to a large extent controlled by the intrinsic properties of the materials that form the positive and negative electrodes. Additionally, the cycle-life and lifetime are both influenced by the nature of the interfaces between the electrodes and electrolyte, while safety is a function of the stability of the electrode materials, electrolyte and interfaces.¹ Therefore, selection of electrode materials is significant for a good-performance lithium battery.

To provide a better understanding on how electrode materials work, section 1.4.1 will briefly introduce the relevant reversible energy storage mechanisms of electrode materials for lithium secondary batteries. An overview on some of the cathode materials will be given in section 1.4.2, followed by details on the specific cathode materials including CuS, S and MoS₂ studied in this work in sections 1.4.3, 1.4.4 and 1.4.5, respectively.

1.4.1 Reversible energy storage mechanism

For lithium secondary batteries, energy storage mechanisms may differ from varieties of electrode materials. Four key mechanisms relevant to inorganic electrode materials will be briefly introduced as follows (see Figure 1-8):^{87,88}

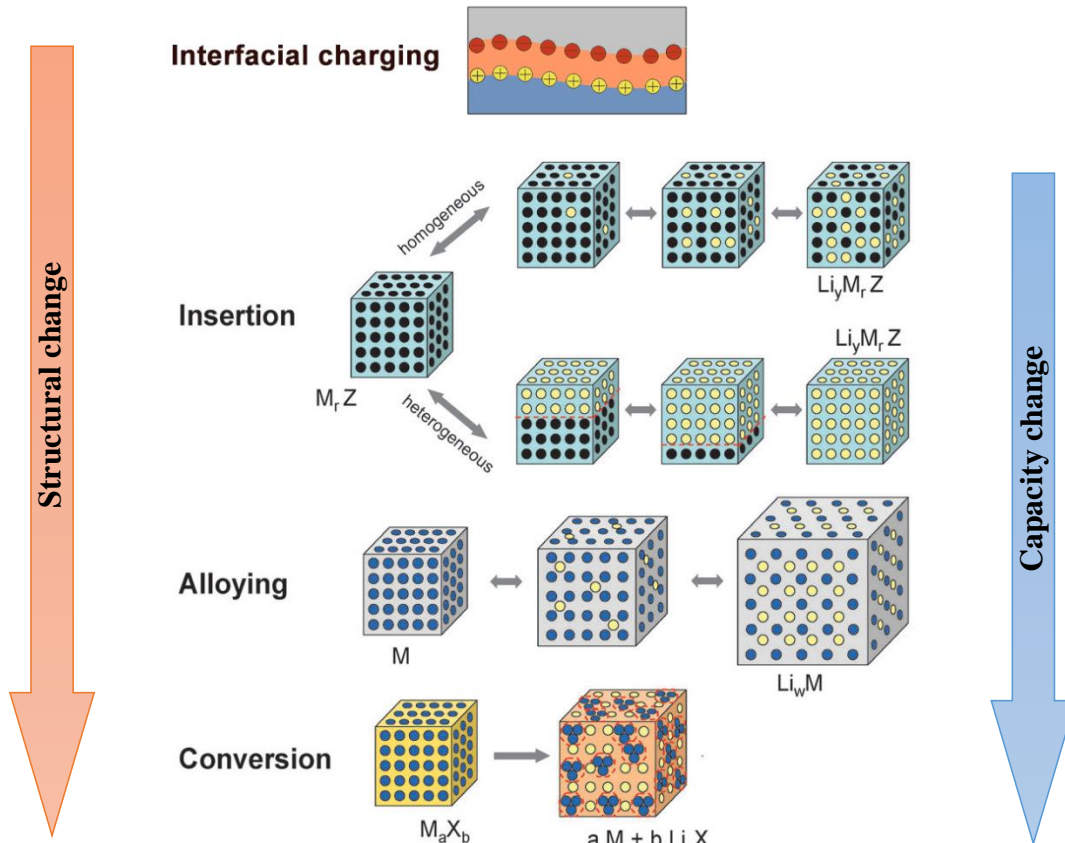


Figure 1-8 A schematic representation of various reversible energy storage mechanisms in lithium-based batteries. Black circles: voids in the crystal structure; blue circles: metal elements; yellow: lithium; red: electrons. Modified from Palacín⁸⁷ and Zu et al.⁸⁸.

1) Insertion reaction mechanism

An insertion (or intercalation) reaction indicates that lithium atoms are accommodated topotactically in the structure of the host electrode material H which is accompanied by charge transfer but without major changes in the atomic rearrangements of the host:^{89,90}



As shown in Figure 1-8, the insertion of lithium into the crystal structure can be either homogeneous or heterogeneous, which can be determined from the voltage variation during electrochemical lithiation or delithiation. If the cathode material is homogeneously lithiated/delithiated, it remains a homogeneous phase of gradually varying lithium content, and the cell voltage will vary continuously (reflecting the electrochemical potential of the phase with the respective lithium content). However, the heterogeneous

lithiation/delithiation process triggers a heterogeneous transition between phases of different lithium content and/or different structure, so that the cell voltage remains constant during the whole process. Usually homogeneous insertion materials are kinetically faster during lithiation and delithiation, yet at the cost of a composite-dependent voltage profile. Currently, the most widely used negative electrode material, graphite⁹¹, and positive electrode material, LiCoO₂⁹², are layered compounds working based on this mechanism (homogeneous insertion). Note that the weak interaction between the layers facilitates the necessary volume changes to accommodate the intercalated ions, but the volume changes and the weak interactions are also limiting the cycle life of intercalation cathodes based on layered structures. Intercalation into one-dimensional channels (e.g. in LiFePO₄⁹³, heterogeneous insertion material) leads to more stable compounds, but is easily blocked by defects anywhere along the channels.

2) Alloying mechanism

Some metallic or semi-metallic elements can electrochemically alloy with lithium at room temperature, commonly with significant structural change. Under this mechanism, number of Li atoms alloyed is not limited to one per metallic (or semi-metallic) atom, leading to a much higher capacity than those found in insertion materials. However, these materials usually encounter significant volume change during cycling resulting in poor cyclability. A typical example is silicon, which exhibits a specific capacity as high as 4400 mAh/g by forming a series of Li-Si alloys (Li₁₂Si₇, Li₁₄Si₆, Li₁₃Si₄, and finally Li₂₂Si₅) during discharging, nevertheless accompanied with a severe volume expansion of 400% (corresponding to the formation of Li₂₂Si₅)^{94,95}.

3) Conversion reaction mechanism

In a narrow sense the term “conversion reaction” commonly refers to the decomposition of one parent (transition metal) compound under the influence of (elemental) lithium into two product phases: the transition metal in the elemental state and the corresponding lithium compound. Reversible conversion reactions of transition metal oxides (TMO) with lithium were reported in 2000 by Poizot et al.:⁹⁶



In other words, the TM in the oxide phase is replaced by lithium. Later it was revealed that conversion reaction could also apply for transition metal fluorides, sulfides, nitrides, phosphides and hydrides.^{97,98,99,100,101}

In a wider sense sulfur as a cathode material can also –as commonly done- be referred to as a conversion electrode material. Sulfur is cheap, non-toxic, earth abundant and shows a high theoretical specific capacity of 1672 mAh/g corresponding to the formation of Li_2S .^{23,24} Challenges facing Li/S batteries are the low electronic conductivity of sulfur and the formation of soluble polysulfides during cycling. To overcome these challenges, encapsulating sulfur in porous carbon is explored intensively.^{102,103} In ASSLBs, where the polysulfide formation is not as much of a problem, sulfur composite cathodes are also studied¹⁰⁴. More details on sulfur as a cathode material will be reviewed in section 1.4.4.

4) Interfacial charging mechanism

Extra lithium can be stored reversibly in LiX/M nanocomposites caused by an interfacial interaction of lithium within the LiX/M matrix, leading to a distinct local charging.^{105,106} Lithium storage capacities of 100-300 mAh/g by interfacial charging have been reported for the systems such as LiF/Ti or $\text{Li}_2\text{O}/\text{Ru}$. Though the capacity is not that high compared to other mechanisms, this mechanism cannot be ignored when the material has a nanostructure with abundant grain boundary. In this work, the role of interfacial storage will be particularly relevant for the cases of MoS_2 and CuS cathode materials.

1.4.2 Overview of cathode materials

Recently, most of cathode materials used and studied are intercalation compounds, which store energy under insertion mechanism. Though studied for decades, the intercalation compounds still encounter numerous challengers. For instance, conventional cathode LiCoO_2 is widely commercialized but suffers from issues of toxicity and relatively high cost. Besides, the specific capacity is restricted to a half of theoretical capacity because of structural degradation when it is charged to values above 4.2V, where the Li content in Li_xCoO_2 falls below $x=0.5$.¹⁰⁷ Olivine compounds like LiFePO_4 are nontoxic and thermally stable and have a moderate capacity with slow fading, but their conductivity is low.¹⁰⁸

It should be mentioned that the most concerning issue facing intercalation compounds is their relatively low capacity compared to anode. Although plenty of classes of intercalation materials were synthesized in the past 30 years, no qualitative improvement on specific capacity was achieved because only one electron at most could be inserted or extracted per 3d-metal. Owing to such intrinsic limitation, various research teams have started to exploit new directions.^{109,110,111}

Materials working under conversion reaction mechanism, including transition metal oxide, fluorides, sulfides, nitrides, phosphides and hydrides, and sulfur (as introduced in 1.4.1), have attracted considerable attention. Such cathode materials are not limited to one electron per 3d-metal as conventional intercalation materials but involve up to 2 or 4 electrons per 3d-metal, which can lead to impressive capacity gains.

Primary batteries operating through the conversion reaction have come into reality long before, such as the commercialized Li/CuO, Li/(CF)_n, Li/SO₂, Li/SOCl₂, Li/FeS₂ batteries in the 1980s.¹¹² However, reversible conversion reactions were investigated more widely only after the report by Poizot et al. in 2000.⁹⁶

The electromotive force (emf) values of the transitional metal compounds are determined by both the cation and anion. For those with the same metal in the same valence state, their emf values have the following order: fluoride >> oxide > sulfide >> nitride > phosphide. For those with the same anion, the one with higher oxidation state would show higher emf value. The calculated emf values of conversion reactions between selected binary transition metal compounds and lithium are shown in Figure 1-9.^{113,114}

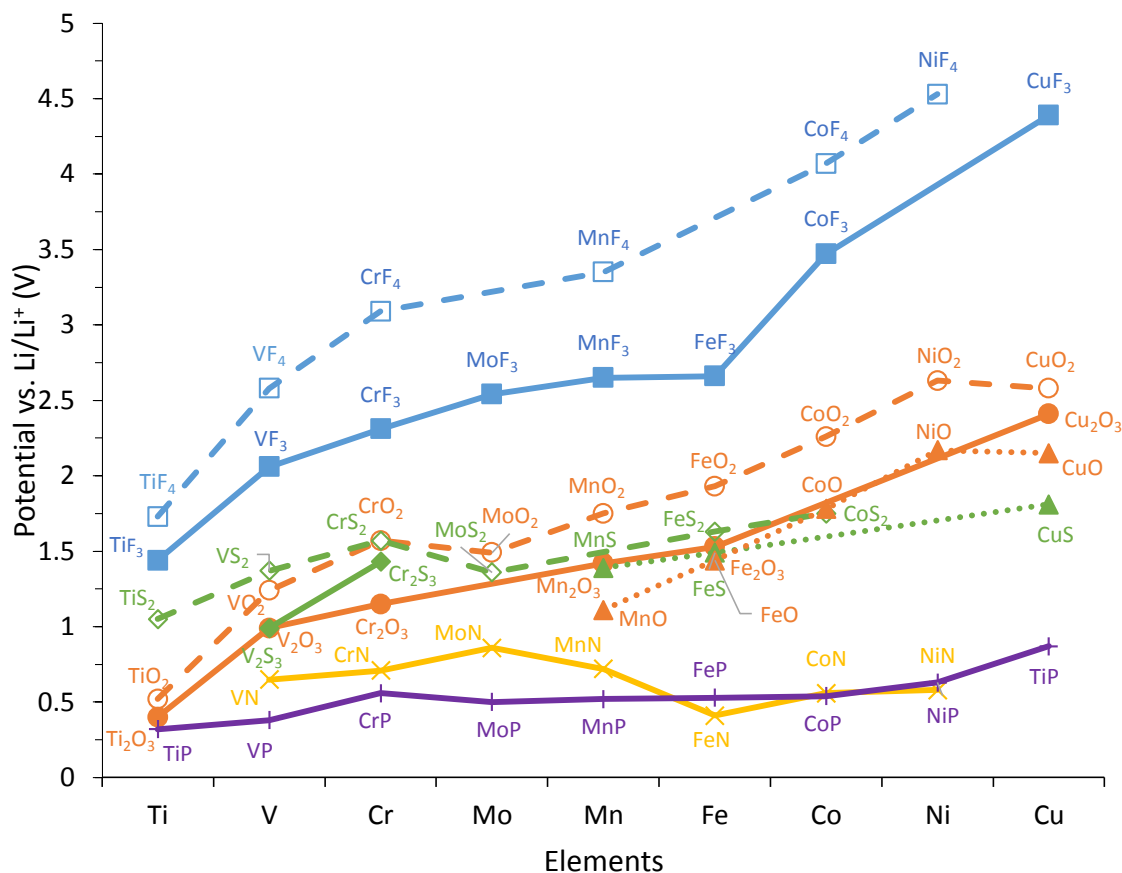


Figure 1-9 Calculated emf values of conversion reactions between selected binary transition metal compounds and lithium. Data were collected from the materials project database.^{113,114}

In spite of their high specific capacity, most conversion reaction type electrode materials suffer from high voltage polarization between the charging and discharging, due to the high activation energy and hence slow kinetics of the first order phase transformation involved in the electrode reaction. Overpotentials exceeding 1 V have been found for most of the transition metal compounds, resulting in low energy efficiency, which limits the application of these compounds.^{115,116,117,118}

To achieve high performance ASSLBs, it is natural to combine sulfide-based solid electrolyte, i.e. lithium argyrodite $\text{Li}_6\text{PS}_5\text{X}$, with sulfide-based cathode materials, making use of their chemical compatibility. Hayashi's group have reported considerable ASSLBs combining $\text{Li}_2\text{S-P}_2\text{S}_5$ glass-ceramic solid electrolyte with various sulfur-based cathode materials, e.g. CuS ¹¹⁹, NiS ^{111,120,121}, S ¹²². In this project, CuS , S and MoS_2 are explored as

cathode materials, which will be introduced in the following sections (sections 1.4.3, 1.4.4 and 1.4.5, respectively).

1.4.3 Copper sulfide

Among all transition metal sulfides, CuS has attracted lots of attentions due to its highest potential vs. Li/Li⁺ electrode (1.81 V, see Figure 1-9), relatively high theoretical specific capacity of 560 mAh/g and specific energy density of 977.7 Wh/kg⁸⁷, high electronic conductivity of >0.1 S/cm¹²³ and high Cu mobility.¹²⁴ In this section, firstly the development and reaction mechanism of CuS in both conventional lithium secondary batteries as well as ASSLBs will be reviewed. Secondly, ASSLBs using the discharged state Cu-Li₂S as their starting cathode materials will be briefly introduced.

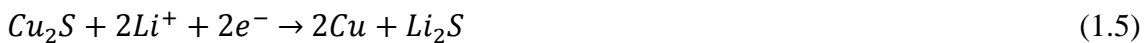
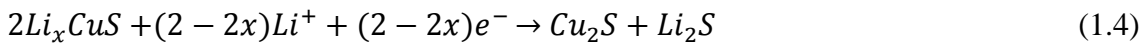
1.4.3.1 Charged state CuS

In 1970s, CuS was considered as one of the most promising cathode materials for lithium primary batteries.¹²⁵ Afterwards, in 1980s, several attempts were made to apply CuS to lithium secondary batteries.^{126,127} However, such application was limited because of the generally observed fast capacity fading and the preference for high voltage oxide cathode materials in LIBs.

Lithium batteries using CuS as cathode have two discharge plateaus around 2.1V and 1.7V, suggesting multi-step reaction during discharge, as shown in Figure 1-10¹²⁸. To understand the electrochemical reaction of CuS and therefrom the reason for rapid capacity fading, several groups have investigated the reaction mechanism in liquid electrolyte lithium-based batteries. Ex-situ XRD results by Chung et al.¹²⁸ showed little change of the pattern during the first plateau of the discharge and the formation of Cu₂S and metallic Cu during the second plateau. Accordingly, they proposed one step of intercalation:



followed by two simultaneous conversion reactions



The reaction described by Equation (1.3) takes places at the first plateau region, representing intercalation of Li^+ into CuS to form Li_xCuS . Afterwards, conversion reactions in Equation (1.4) and (1.5) occur simultaneously at the second plateau region, which leads to $\text{Cu}_{1.96}\text{S}$ and finally Cu and Li_2S . According to such intercalation-conversion reaction mechanism, Chung et al. proposed to limit the cycling voltage of the batteries to between 1.8 V and 2.6 V, i.e. within the intercalation step. In such way, the battery obtained an initial discharge capacity of 267 mAh/g and more than 70% capacity retention (~190 mAh/g) after 60 cycles.

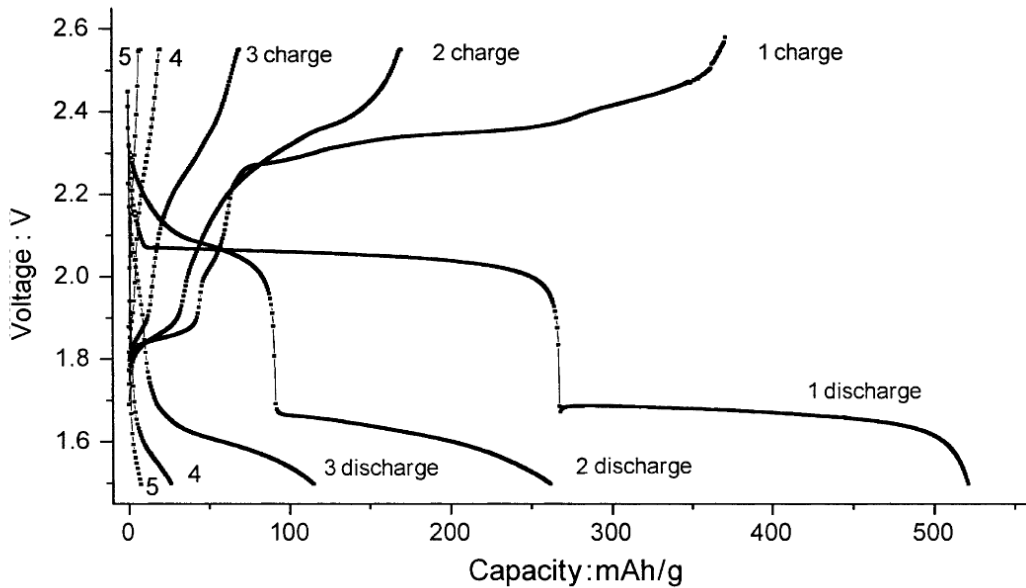


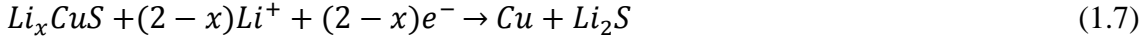
Figure 1-10 Behavior of high purity CuS electrode vs. lithium when using liquid electrolyte over five cycles between 1.5 and 2.6V range at room temperature.¹²⁸

On the other hand, D'Arbort et al.¹⁰⁹ suggested that the initial plateau is already caused by a conversion reaction:

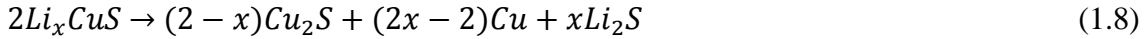


(which formally can be understood as a sum of Eqs. (1.3) and (1.4), but they cannot discern any signs of an intercalation step). This would be followed by the second conversion reaction according to Equation (1.5) explaining the second plateau.

Yamakawa et al.¹²⁹, by combining solid-state nuclear magnetic resonance (NMR) and ex-situ XRD, agreed with Chung et al.¹²⁸ on the first process being an intercalation reaction (Equation (1.3)) but proposed that the second plateau refers to a single-step electrochemical conversion process:



simultaneously accompanied by the decomposition of unstable Li_xCuS to Cu_2S , which according to these authors should be responsible for at least some of the capacity fading:



It is noted in all these studies that “ Cu_2S ” in these simplified reaction schemes has to be understood as a series of intermediary products $Cu_{2-x}S$ of Chalcocite ($x \approx 0$) or Djurleite ($x \approx 0.03-0.07$) structures.

Despite the controversy on the detailed reaction path, it is commonly agreed on that complete discharging leads to a mixture of metallic copper and Li_2S . In this mixture, the Li_2S acts as the matrix and is surrounded by large dendritic copper (more than 1 μm long).

As for the charging process, the plateaus showed a more complicated behavior due to the formation of various intermediary copper sulfide phases, i.e. Cu_2S , $Cu_{1.96}S$, $Cu_{1.8}S$, Cu_7S_4 , $Cu_{1+x}S$ ($x < 0.4$) and finally CuS .¹²⁸

Potential applications of CuS in ASSLBs, besides lithium secondary batteries using organic liquid electrolyte, have been studied by Hayashi et al.^{119,130} and Machida et al.¹³¹. Both of the groups prepared the CuS by ball milling stoichiometric or non-stoichiometric mixtures of Cu and S : Machida et al., by combining 44 wt% Cu -56 wt% S composite with Li_2S - P_2S_5 glass solid electrolyte, obtained an ASSLB with an initial discharge capacity of 547 mAh/g and reversible capacity of 602 mAh/g after 5 cycles. By ex-situ XRD, they confirmed the participation of Cu in the electrode reaction. Hayashi et al. optimized the preparation of Cu - S composite to be a molar ratio of $Cu:S=1:3$ ¹³⁰ and ball milling time of 5h¹¹⁹. Accordingly, ASSLBs using Li_2S - P_2S_5 glass-ceramic electrolyte was reported with an initial discharge capacity of 650 mAh/g and little capacity fading after 20 cycles. They proposed that for cathodes employing non-stoichiometric $Cu:S$ ratios, two reactions

proceed simultaneously at the first plateau, i.e. intercalation reaction (Equation (1.3)) together with Equation (1.9):



Equation (1.9) represents the utilization of excess S in Cu-S composite by regeneration of CuS. The second plateau is then ascribed to the conversion of the intercalation product Li_xCuS as shown in Equation (1.7).

It should be noted that all the specific capacities mentioned above are calculated based on the weight of the Cu-S composite. The theoretical specific capacity of stoichiometric CuS is 560 mAh/g, while varying the Cu:S ratio would affect its theoretical capacity (leading to e.g. a capacity of 915 mAh/g for a molar ratio of Cu:S=1:3 corresponding to the weight of Cu and S).

So far, neither of the groups have studied the reaction mechanism of stoichiometric CuS in ASSLBs. Besides, the only XRD results on CuS-based ASSLBs by Machida et al.¹³¹ could not yield any information on structural changes of the solid electrolyte, as the solid electrolyte used in their study was a glass. As a consequence, no conclusion could be drawn on whether there is any interaction between the active materials and solid electrolyte. In the thesis, I studied the reaction mechanism of CuS in ASSLBs and investigated in detail its interaction with Li_6PS_5Br . More details would be discussed in section 4.2.

1.4.3.2 Discharged state Cu-Li₂S

Besides application of CuS as cathode in lithium secondary batteries (as introduced in previous section), the composite Cu-Li₂S representing the discharged state of the cathode may also be used as the pristine electrode material. By introducing finely dispersed metallic copper, Cu-Li₂S overcomes the electronically insulating nature of the discharge product Li₂S. In addition, Cu-Li₂S can be combined with negative electrodes that do not contain lithium sources, e.g. carbon, indium, which are considered as safer and more stable anode materials compared to metallic lithium.

Hayashi et al. reported ASSLBs with Cu-Li₂S as the cathode and Li₂S-P₂S₅ glass-ceramic as the electrolyte.^{132,133} By ball milling Cu with Li₂S in an optimized molar ratio of 1:3 for

5h, they found an initial charge and discharge capacity of 580 (660) mAh/g and 490 (560) mAh/g respectively, and reversible capacity of 300 (340) mAh/g at 30th cycle. Their reported XRD patterns show the existence of CuS domains in the charged state after cycling for 10 cycles. Accordingly, the authors attribute the capacity fading to the formation of electrochemically inactive CuS domains, due to the severe volume changes of the electrode materials.

Note that the capacities were calculated based on the weight of Cu-Li₂S. To make them comparable to those of the CuS-based batteries, capacities corresponding to the weight of Cu-S are shown in brackets. Theoretically Cu-Li₂S in a molar ratio of 1:1 has a capacity of 490 (560) mAh/g, while reducing the molar ratio to 1:3 enhances the capacity to 800 (915) mAh/g.

1.4.4 Sulfur

Especially the non-stoichiometric Cu-S-based cathodes may be formally thought of as Li/S batteries, in which the introduction of CuS increases both the electronic (and presumably the ionic conductivity) at the expense of a reduced specific energy density compared to sulfur or lithium sulfide. However, in the later stage of this study it was found that Cu⁺ ions will react with solid electrolyte Li₆PS₅X (to be discussed in detail in section 4.2). Therefore, it would be interesting to compare the electrochemical performance of all-solid-state Li/S batteries to that of Li/CuS batteries. This section will review the challenges facing Li/S batteries and approaches that have been utilized to solve these issues. While replacing liquid electrolyte is one of the promising ways, a more detailed review on the studies of all-solid-state Li/S batteries will then be given.

Among the various lithium secondary battery systems, Li/S batteries represent one of the most significant contenders for next-generation battery systems with regard to their superior energy density. Sulfur, by forming Li₂S after full charge, exhibits a theoretical specific capacity as high as 1672 mAh/g, leading to a theoretical energy density of 2567 Wh/kg in spite of a relatively low voltage around 2 V vs. Li/Li⁺.^{23,24} For comparison, the currently commercialized LIB systems (e.g. C/LiCoO₂ and Li/LiMn₂O₄) have theoretical

and practical energy densities of 430 to 570 Wh/kg and 120 to 180 Wh/kg.¹³⁴ Moreover, elemental sulfur is earth abundant, inexpensive and non-toxic.¹³⁵

Nevertheless, despite these considerable advantages, Li/S batteries are hindered for further practical application due to several problems. Firstly, intermediate reaction products, polysulfides, are soluble in most of the commonly employed organic liquid electrolytes. During discharge, elemental sulfur S₈ would be gradually reduced to a series of lithium polysulfides Li₂S_n with n=8, 6, 4, 2. Long chain polysulfides would form first, e.g. Li₂S₈, Li₂S₆, while further reduction leads to shorter sulfur chain, such as Li₂S₄, Li₂S₂ and finally Li₂S, as shown in Figure 1-11.^{136,137,138} Among all these polysulfides, Li₂S₈, Li₂S₆ and Li₂S₄ are soluble in liquid electrolyte, while Li₂S₂ and Li₂S are insoluble. In liquid electrolyte Li/S cells, polysulfides formed in the cathode will at certain discharge/charge states dissolve into the liquid electrolyte, diffuse through the separator, be reduced to lower-order polysulfides by reacting with lithium anode, and then diffuse back to cathode to be re-oxidized to higher-order polysulfides. Such phenomenon is called internal shuttle effect¹³⁹. It will cause self-discharge, poor coulombic efficiency and rapid capacity fading. Besides, further reaction of polysulfides with lithium leads to the formation of insoluble and electrically insulating Li₂S or Li₂S₂^{140,141} on the surface of the anode, resulting in mass loss of active cathode materials and an increase in internal resistance and thus significant capacity fading. In addition, phase segregation of the insoluble S, Li₂S and Li₂S₂ in the cathode composite over cycling may disrupt the electronically conducting pathways inside the composite cathode and hence slow down or even stop the electrochemical process.

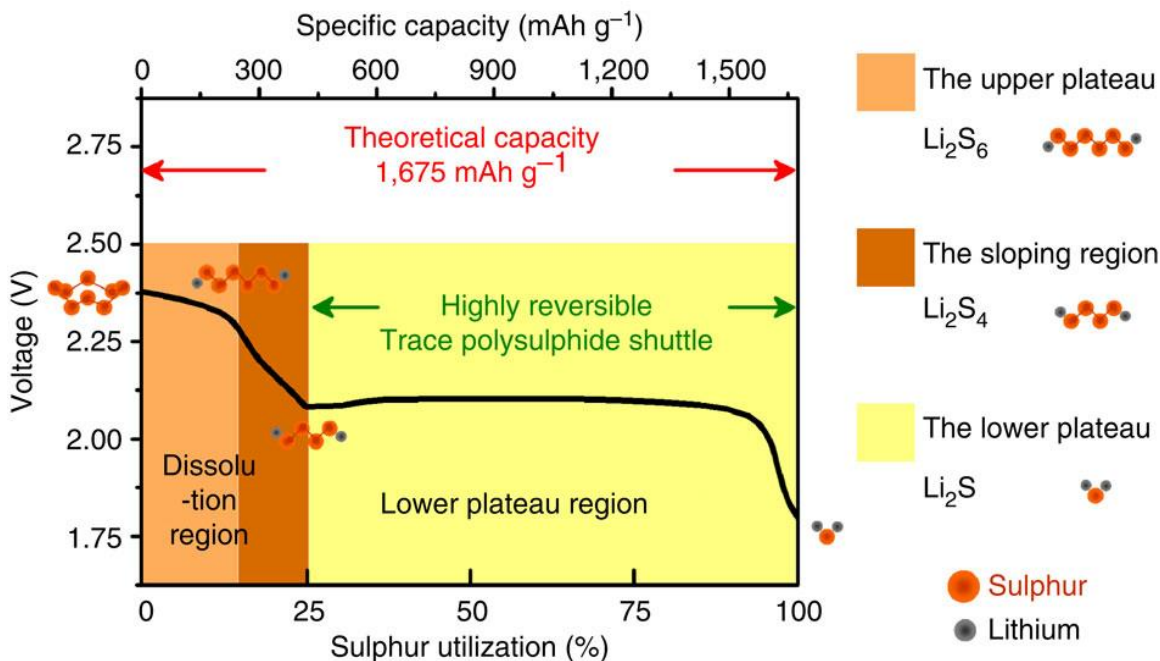


Figure 1-11 Schematic discharge reaction mechanism of Li/S batteries. The products Li_2S_8 , Li_2S_6 , Li_2S_4 are soluble in the liquid electrolyte.¹³⁶

Secondly, sulfur exhibits severe volume change during cycling (expansion by about 80% during discharge corresponding to the overall electrode reaction $\text{S} + \text{Li} \rightarrow \text{Li}_2\text{S}$). As a result, the active material may lose contact with electron- or ion-conducting components of the composite cathode mostly during charging, which leads to a poor capacity retention.

Thirdly, sulfur shows practically neither electronic conductivity ($5 \times 10^{-30} \text{ S/cm}$)¹⁴² nor ionic conductivity (10^{-13} S/cm)¹⁴³. To overcome the lack of electronic conductivity, a relatively large amount of conductive materials, e.g. carbonaceous materials (such as mesoporous carbon¹⁴⁴, graphene¹⁴⁵, etc.) or conductive polymers¹⁴⁶, need to be added to the cathode. Analogously the ionic conductivity needs to be enhanced by admixture of significant amounts of solid electrolytes or by the chemical reaction of S with solid electrolytes forming compounds that are both ion-conducting and redoxactive such as explored by Lin et al.¹⁴³ who prepared polysulfidophosphates through the reaction of sulfur with Li_3PS_4 in tetrahydrofuran (THF) solution. The resulting all-solid-state Li/polysulfidophosphates battery showed good rate capability: 735 mAh/g at 2C rate.

Among all the issues mentioned above, high solubility of polysulfide in liquid electrolyte is one of the key factors limiting the cyclic performance of Li/S batteries. To improve the cyclability of Li/S batteries, several approaches were proposed.

- Encapsulating sulfur in porous carbon or graphene.

In 2009, Ji et al.¹⁴⁴ proposed nanostructured sulfur-porous carbon composite, using highly ordered mesoporous carbon, i.e. CMK-3. Besides providing electron and Li⁺ pathway, porous carbon could encapsulate sulfur and retard the diffusion of large polysulfide anion out of electrode, thus increasing the capacity retention of Li/S batteries. Accordingly, an initial capacity of 1320 mAh/g was reported, with a reversible capacity of 1100 mAh/g after 20 cycles. Jayaprakash et al.¹⁰³ encapsulated 70 wt% of sulfur in mesoporous carbon sphere, leading to a battery with a reversible capacity of 974 mAh/g after 100 cycles. Zhang et al.¹⁴⁷ prepared sulfur-carbon sphere composite by encapsulating sublimed sulfur into micropores of carbon sphere. The resulting batteries exhibited a reversible capacity of 650 mAh/g even after 500 cycles. In addition, graphene-wrapped sulfur cathode has attracted considerable attentions as well. Yin et al.¹⁴⁵ reported a battery using polyacrylonitrile/graphene composite as cathode, with a reversible capacity of 1200 mAh/g after 50 cycles, and a superior high rate performance (800 mAh/g at 6C).

To reduce the destruction caused by the volume change of active materials during cycling, in most of the cases, pores of carbon were partially filled by sulfur, leaving some space to compromise the volume expansion of sulfur during discharge.

- Additives in liquid electrolyte.

Using additives in liquid electrolyte could protect anode from reacting with polysulfide, and hence improve the cyclability of the batteries. One of the promising additives is LiNO₃.^{148,149} LiNO₃, together with the solvent and polysulfides, could react with Li anode, forming a layer of solid electrolyte interface (SEI) on the surface of anode.¹⁵⁰ This layer could act as a protective film, preventing Li anode from reaction with the dissolved polysulfids, however, in the expense of safety due to the strong oxidation of LiNO₃. An alternative is lithium bis(oxalate) borate (LiBOB), which is more thermally stable and environmentally friendly. Xiong et al.¹⁵¹ reported a Li/S battery using an electrolyte

consisting of $\text{LiN}(\text{CF}_3\text{SO}_2)_2$ in DIOX and DME with 4 wt% of LiBOB as additive. The battery showed a reversible capacity of 756 mAh/g after 50 cycles.

- Ionic liquid-based electrolyte.

Replacing solvent of conventional organic liquid electrolyte with ionic liquid could mitigate the dissolution of polysulfides. An example is N-methyl-N-butyl-piperidinium (PP14). Yuan et al.¹⁵² reported a Li/S batteries using PP14-bis(trifluoromethanesulfonyl) imide (TFSI) as electrolyte, achieving an initial discharge capacity of 1055 mAh/g, but still a capacity fading to 750 mAh/g after 10 cycles.

Although the approaches mentioned above could effectively improve the cyclability of Li/S batteries, dissolution of polysulfide was only alleviated, but not eliminated. As a result, cyclability of the resulting Li/S batteries was still not comparable to that of conventional LIB using intercalation materials. Concerning that there is typically no solubility between solid and solid, replacing liquid electrolyte with solid electrolyte could get rid of the issues caused by dissolution of polysulfides, thus showing great potential to achieve a high performance Li/S battery.

In 2008, Kobayashi et al.¹⁰⁴ assembled all-solid-state Li/S using a thio-LISICON solid electrolyte, with sulfur composite cathode fabricated by gas-phase mixing. The resulting batteries showed a reversible capacity of 900 mAh/g after 10 cycles, at relatively low current density. In 2011, Nagao et al.¹²², by mixing sulfur composite cathode using two-step ball milling, achieved a Li/S battery with a reversible capacity of 850 mAh/g after 200 cycles at a current density of C/5 at room temperature. The solid electrolyte used is glass-ceramic $\text{Li}_2\text{S-P}_2\text{S}_5$. It should be noted that in both studies mentioned above, the sulfur content in the composite cathode is 25 wt%. To increase the sulfur content, in 2013, the same group, Nagao et al.¹⁵³, prepared sulfur composite cathode using high-temperature ball milling at 155 °C. Consequently, the sulfur content was increased to 50 wt%, while the battery still maintained a reversible capacity of 1050 mAh/g after 50 cycles at C/50. On the other hand, Agostini et al.¹⁵⁴ prepared sulfur-graphite composite by melting sulfur (ca. 23 wt% of sulfur in composite cathode). However, the resulting ASSLB with glass $\text{Li}_2\text{S-P}_2\text{S}_5$ as electrolyte only showed a reversible capacity of 400 mAh/g after 20 cycles at an operating temperature of 80 °C. Kinoshita et al.¹⁵⁵ from the same group used Vapor Grown

Carbon Fiber (VGCF) as the electronic conductor instead of acetylene black and studied the effect of ball milling time of sulfur composite cathode (30 wt% of S) on the cyclic performance of ASSLBs. By two-step ball milling sulfur and carbon for 10 h and then the complete composite for 40 h, ASSLB with Li_3PS_4 as electrolyte achieved a reversible capacity of 1200 mAh/g after 50 cycles. More recently in 2014, Nagata et al.¹⁵⁶ reported that the specific area of the conductive materials in the composite sulfur cathode has a significant impact on the battery performance. By employing activated carbon with a specific surface area as high as 3000 m^2/g as the electronically conductive component, they achieved a Li/S battery with a reversible capacity of 1600 mAh/g after 100 cycles at 1C at room temperature.

Despite this recent progress on all-solid-state Li/S batteries, ASSLBs using lithium argyrodites as solid electrolyte are not yet studied. Therefore, it should be beneficial to study ASSLBs combining sulfur with argyrodite $\text{Li}_6\text{PS}_5\text{X}$. More details would be discussed in Chapter 5.

1.4.5 Molybdenum sulfide

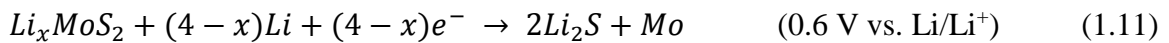
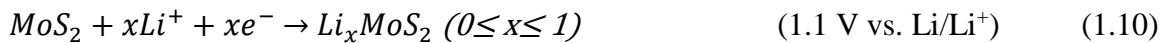
Despite of high specific capacity and energy density, sulfur shows low electronic conductivity, as discussed in the previous section (section 1.4.4). A common and to some extent effective solution is to add relatively large amounts of electronically conductive materials, such as carbon black¹⁰² and graphene¹⁴⁵. Recently, it was found that a high-performance Li/S battery can also be achieved by fully discharging a battery using MoS_2 as cathode. In such way, MoS_2 will effectively turn into a sulfur cathode with embedded finely dispersed metallic Mo nanoparticles.^{157,158} These Mo nanoparticles provide an electrical pathway to facilitate the electrode reaction. In this project, all-solid-state $\text{MoS}_2/\text{Li}_6\text{PS}_5\text{Br}/\text{In-Li}$ battery was investigated as a novel type of Li/S battery. This section will introduce the state of knowledge in the literature about the structure of MoS_2 , lithium secondary batteries using MoS_2 as electrode materials, and the electrode reaction in such batteries.

Crystalline MoS_2 usually has layer structure wherein Mo atoms are sandwiched between two layers of S atoms with covalent bonds and hexagonally packed into a stack; the

adjacent MoS₂ slabs are held together by van der Waals interaction. Based on the number of stacks in a unit cell, MoS₂ can be classified into three polymorphs, i.e. 3R, 2H and 1T, where the digit represents the number of MoS₂ stacks in a unit cell, and R, H and T stand for rhombohedral, hexagonal and trigonal, respectively. Both 3R and 2H have trigonal prismatic coordination of the Mo atom, while 1T has an octahedral Mo coordination. Natural MoS₂ predominantly has the stable 2H structure, while synthetic MoS₂ often shows the metastable 3R polymorph. After chemical/electrochemical alkali-intercalation or exfoliation, MoS₂ will experience a phase transition to 1T.¹⁵⁹ The metallic 1T-MoS₂ phase is metastable and will transform back to semiconducting 2H-MoS₂ upon moderate heat treatment¹⁶⁰ or long time aging¹⁶¹, etc.

Besides widespread use as a lubricant¹⁶² as well as hydrogen storage material¹⁶³, photo catalyst¹⁶⁴ or transistor¹⁶⁵, MoS₂ has been intensively studied as electrode material for lithium secondary batteries. For this application, MoS₂ shows advantages of high theoretical capacity of 670 mAh/g, high energy density, low cost, high safety and facile synthesis. Actually, liquid electrolyte MoS₂/Li batteries have been the first commercialized lithium secondary batteries (MOLICELTM) in the world, manufactured by Moli Energy Ltd. in the early 1980s. Nevertheless, these batteries experienced severe safety issues, including catching fire (mainly because of the lithium anode), and were recalled from the market.¹⁸

During the first discharge, lithium batteries using MoS₂ as the cathode material have two plateaus around 1.1 V and 0.6 V vs. Li/Li⁺, representing one intercalation and one conversion reaction.¹⁵⁷



The intercalation process contributes ~167 mAh/g to the theoretical capacity, corresponding to one Li⁺ per Mo atom. Still only at the early stage of the discharge ($x < 0.1$), Li⁺ ions intercalate into the interlaminal spaces of 2H-MoS₂ with little distortion to the structure. On further intercalation ($0.1 \leq x \leq 1$) an irreversible phase transition from 2H-Li_xMoS₂ with the trigonal prismatic Mo coordination of 2H-MoS₂ to 1T-Li_xMoS₂ with the

octahedral Mo coordination of 1T-MoS₂ occurs.^{166,167} Charging back from this stage will still form MoS₂, but the product will adopt the 1T-MoS₂ polymorph instead of 2H-MoS₂.

During the second step of discharge, which accounts for a theoretical capacity of 503 mAh/g, 1T-Li_xMoS₂ undergoes a conversion reaction, leading to metallic Mo and Li₂S at the end of the discharge. HRTEM showed that the Mo crystallites exhibit a particle size between 3 – 6 nm.¹⁵⁷ Such nano-sized particles introduce large area Mo/S or Mo/Li₂S interfaces, where Li⁺ could reside. Therefore interfacial charge storage may contribute to an excess (pseudo-)capacitive discharge capacity, leading to practical capacities that are higher than the theoretical capacity if the discharge voltage limit is set close to 0 V.

It is important to note that the conversion step of the MoS₂ electrode reaction is no longer reversible, different from what is found for most transition metal sulfides such as CuS¹⁶⁸, NiS¹²¹, FeS¹⁶⁹, CoS₂¹⁷⁰, etc. During the subsequent charge cycles, MoS₂ (1T-MoS₂ or 2H-MoS₂) will not form any more. Instead, metallic Mo will become inert and no longer participate in the cycling, effectively turning the battery into a Li/S battery:^{157,158}



where Mo is retained in the equation to highlight its inertness, though practically it does not take part into the reaction. The metallic molybdenum in the Li/S battery significantly increases the electronic conductivity of the otherwise insulating cathode (S and Li₂S), thus improving the rate performance of the battery. For liquid electrolyte batteries, the Mo nanoparticles can also serve to immobilize the soluble polysulfides and enhance the cyclic performance of the batteries.¹⁵⁸ As mentioned above capacitive storage at the Mo/Li₂S also plays an important role at low voltages. Chen et al.¹⁵⁷ proposed that the redox reaction of S/S²⁻ ends at or above 1 V, while below 1 V additional Li⁺ ions would then be mainly stored at the Mo/Li₂S interface.

Despite of the great interest in MoS₂ for decades, the poor cyclic performance and rate capability of MoS₂ in liquid electrolyte batteries have been major limitations for the practical application. Recently, massive studies focused on the fabrication of nanostructured MoS₂ combined with conductive carbon/graphene to reduce the particle size and improve the electronic conductivity. Guo et al.¹⁷¹ fabricated MoS₂@CMK-3

nanocomposites via a simple nanocasting technique using CMK-3 carbon as the template. The incorporation of MoS₂ into CMK-3 with high specific surface area favors a faster lithium insertion and therefore higher rate capability. The Li/MoS₂ batteries using these nanocomposites showed a reversible capacity of 602 mAh/g at 250 mA/g ($\approx C/3$) after 100 cycles, and still retained a capacity of 564 mAh/g at higher rate of 2 A/g ($\approx 3C$). Archer et al.¹⁷² prepared hierarchical MoS₂-amorphous carbon composite by hydrothermal method. It was found that the amount of amorphous carbon greatly influences the battery performance. With optimized 22 wt% of carbon, the battery showed a reversible capacity of 755 mAh/g after 100 cycles at 100 mA/g. More recently, Guo et al.¹⁷³ synthesized MoS₂-graphene nanosheets by a lithiation-assisted exfoliation process followed by a hydrazine monohydrate vapor reduction technique. The graphene not only provides fast electronic and ionic transport for the electrode reaction but also prevents the agglomeration of MoS₂ nanosheets during the cathode composite preparation and/or of the Mo metal nanoparticles formed during the first discharge. A reversible capacity of 915 mAh/g was obtained up to 700 cycles. Excellent high rate capability was also observed, e.g. at a rate of 20 A/g (30C) still a capacity of 339 mAh/g could be achieved.

As mentioned above, most of the batteries using nanostructured MoS₂ reach a capacity higher than theoretical capacity if the discharge is extended to low voltages, which could be attributed to the following three factors. First, formation of Mo nanoparticles (and graphene in some cases) favors interfacial Li⁺ storage. Second, polymeric SEI layer may reversibly form around the metallic particles (so that the electrolyte should partly be counted as an active material).¹⁷⁴ Third, a non-negligible amount of carbon/graphene is typically incorporated in the electrode but not taken into account into the calculation of the specific capacity.

In contrast to the in depth studies on MoS₂ as electrode materials for liquid electrolyte lithium batteries, few reports have been published on the application of MoS₂ in ASSLBs. Julien et al.^{175,176} presented an ASSLB using disordered MoS₂ as cathode in combination with B₂O₃-Li₂O-Li₂SO₄ solid electrolyte. The resulting battery showed an initial capacity of 160 mAh/g and 145 mAh/g up to 90 cycles, at a low current of 15 $\mu\text{A}/\text{cm}^2$. However, the voltage scale was 1.4-2.0 V, which fell beyond the typical MoS₂ electrode reaction

voltage of 1.1 V (intercalation) and 0.6 V (conversion reaction). The CV curve of the ASSLB¹⁷⁶, with two peaks around 2.5 V and 2.1 V, is also deviated from the typical CV curve of the liquid electrolyte batteries. The author proposed that the higher disordering of the starting MoS₂ cathode materials is the reason for the higher discharge and charge voltage.

In this project, all-solid-state MoS₂/Argyrodites/In-Li batteries were designed and studied. Since MoS₂/Li battery can be treated as a Mo-S/Li battery after the first discharge, replacing the liquid electrolyte by a solid electrolyte again can eliminate the problems caused by the dissolution of polysulfides, thus further improving the cyclability of the battery. More details will be discussed in Chapter 6.

1.5 Objectives and Significance of the thesis

In view of the above review, research gaps for the current study of sulfide materials in ASSLBs are summarized below:

- Conventional LIBs are facing safety concerns and limited cyclability due to the reliance on flammable organic liquid electrolyte.
- ASSLBs that replace organic liquid electrolyte by solid electrolyte can significantly improve the safety and cyclability of the batteries. However, more investigations on solid electrolytes with high ionic conductivity, low electronic conductivity, high electrochemical/chemical stability are still required.
- Interfaces among active materials, solid electrolyte and electronically conductive materials still need to be optimized.
- Although lithium argyrodites Li₆PS₅X show great potential among inorganic solid electrolytes, fabrication conditions have yet to be optimized and details on the structure and electrochemical properties as a function of preparation conditions are to be clarified.
- Despite potentially higher chemical compatibility of argyrodites Li₆PS₅X with sulfur-based electrode materials, no ASSLBs combining argyrodite electrolyte with sulfur-based cathode materials, including CuS, S and MoS₂, have been reported so far. Besides the high ionic conductivity of the sulfur-based solid electrolytes, their

combination with sulfur-based electrode materials (of rather similar Fermi energy) appears promising also from the point of minimizing charge transfer impedances.

- Reaction mechanism of CuS as a cathode materials is discussed controversially even for conventional LIBs. No study has been done so far on the reaction mechanism of CuS in ASSLBs.

The overall goal of this project was therefore to optimize fabrication of argyrodites and develop high-energy density ASSLBs integrating lithium argyrodites as the solid electrolyte. Therefore the specific objectives of the thesis project have been:

- To study the structure and electrochemical properties of lithium argyrodites $\text{Li}_6\text{PS}_5\text{X}$, and optimize the fabrication of argyrodites.
- To design and realize high energy density ASSLBs using argyrodites electrolyte exploring combinations with various high capacity sulfide materials, i.e. CuS, S and MoS_2 .
- To investigate effects of original states of cathode materials on the performance of ASSLBs.
- To investigate the reaction mechanism of CuS in ASSLBs.

The results of the thesis may not only yield a better understanding of argyrodites but also provide a guideline for their fabrication. Moreover, it is shown up how to realize high-performance ASSLBs based on the lithium argyrodites solid electrolytes, providing insight into competitive cyclic performance and the underlying fundamentals governing the performance of such ASSLBs. Additionally, the study aims to shed light on the so far controversially discussed reaction mechanism of CuS cathode materials revealing a special mechanism for the case of ASSLBs.

It is one of the main strengths of lithium-based secondary batteries that a wide range of reaction chemistries and detailed designs can be employed to optimize battery performance for specific applications. As a consequence there is a wide range of choices when selecting candidate materials for the three essential battery components (cathode, electrolyte and anode). Among this wide range of choices, based on an initial evaluation of promising materials combinations, this thesis specifically focuses on lithium argyrodites as the solid

electrolytes and only sulfur-based materials are considered as cathode materials. For the anode side, lithium or indium-lithium alloys are used and optimizing the anode is considered beyond the scope of this project.

In the following part of the thesis, Chapter 2 will give the details of experimental methods used in the preparation and characterization of materials and devices. Chapter 3 details the fabrication, structure and electrochemical properties of lithium argyrodites $\text{Li}_6\text{PS}_5\text{X}$, while in Chapters 4 - 6 ASSLBs using CuS , S and MoS_2 as cathode are discussed, respectively. The final Chapter 7 summarizes the conclusions and indicates the work for further work.

Chapter 2 EXPERIMENTAL DETAILS

This chapter will detail the preparation of solid electrolyte Lithium argyrodites $\text{Li}_6\text{PS}_5\text{X}$ (section 2.1) and various composite cathode powders, including CuS (section 2.2.1), Cu- Li_2S (section 2.2.1), MoS_2 (section 2.2.4) and S (section 2.2.3), followed by the assembly of ASSLBs (section 2.2.4). For characterization, X-ray diffraction, neutron powder diffraction, scanning electron microscopy, transmission electron microscopy, electrochemical impedance and electrochemical cycling will be introduced in section 2.4.

All the following materials preparations and battery assemblies were conducted in glove box under argon atmosphere, due to the sensitivity of argyrodites, Li_2S , lithium and lithiated metal sulfides to both oxidation and humidity.

2.1 Preparation of Lithium Argyrodites

Lithium argyrodites with the nominal composition $\text{Li}_6\text{PS}_5\text{X}$ ($\text{X}=\text{Cl}, \text{Br}$) were fabricated by ball milling and subsequent heat treatment. Stoichiometric mixtures of reagent-grade Li_2S (Alfa Aesar, 99.9%), P_2S_5 (Loba Chemie, 98%) and LiX (LiCl and LiBr , Sigma-Aldrich, 99.9%), together with 18 of 10 mm zirconia balls, were put into a 45 ml zirconia bowl and milled using a high-energy planetary ball mill (Fritsch Pulverisette 7) under a rotating speed of 500 rpm for 20h. The resulting precursor mixture was pelletized, annealed at 300 °C for 5h under argon atmosphere and ground again for further applications.

To investigate the effect of ZnO on the chemical stability of lithium argyrodites, ZnO (Sigma Aldrich, < 100 nm) was mixed with crystalline $\text{Li}_6\text{PS}_5\text{Br}$ in a molar ratio of $\text{Li}_6\text{PS}_5\text{Br}:\text{ZnO}=10:1$ by ball milling at 230 rpm for 2 h.

2.2 Preparation of Various Composite Cathode Powders

To avoid moisture absorption during fabrication, transportation and storage, the raw materials, including carbon, Cu, CuS and MoS_2 , were dried in a vacuum oven (that is attached to the glove box) at 80 °C for 24 h under argon atmosphere and kept in the glove box prior to use. For all the composite cathode powder preparations, the high-energy ball

mill employed was Fritsch Pulverisette 7 equipped with 45 ml Zirconia bowls, while the balls-to-powder weight ratio was 15:1.

2.2.1 Cu-Li₂S composite cathode powder

A mixture of reagent grade Cu (Merck) and Li₂S in a molar ratio of 1:1 was ball milled at 500 rpm for 5h. Composite cathode powders were then prepared by mixing Cu-Li₂S as prepared above, Li₆PS₅Br and super P carbon in a weight ratio of 40:56:4 by mortar grinding or ball milling at 500 rpm for 30 min.

2.2.2 CuS composite cathode powder

To reduce the particle size, commercial CuS powder (Sigma-Aldrich, 99%) was ball milled at a rotating speed of 500 rpm for 20h. The resulting CuS powder was mixed with Li₆PS₅Br and super P carbon in a weight ratio of CuS:Li₆PS₅Br:C = 40:56:4 by ball milling at 500 rpm for 30 min.

2.2.3 Sulfur composite cathode powder

Sulfur was mixed with super P carbon in a weight ratio of 2:1 and ball milled at 500 rpm for 5h. Lithium argyrodite Li₆PS₅Br was then added, leading to a total weight ratio of S:Li₆PS₅Br:C = $p : (100 - 1.5 p) : 0.5 p$ with $p = 20, 25, 30$ or 40 . The resulting mixture was then ball milled at 500 rpm for 30 min.

2.2.4 MoS₂ composite cathode powder

MoS₂ (Sigma-Aldrich, 99%) was mixed with super P carbon and Li₆PS₅Br in a weight ratio of MoS₂:Li₆PS₅Br:C=40:56:4. The mixture was then ball milled at 500 rpm for 30 min.

2.3 Assembly of All-solid-state Lithium Batteries

The respective composite cathode powder and Li₆PS₅Br solid electrolyte were pelletized in a 13 mm die under a pressure of 6000 kg/cm² (see Figure 2-1). Depending on different states of charge/discharge of the active materials, there are two types of anode compositions can be selected: As a lithiated sulfide cathode material (discharged state), i.e. Cu-Li₂S, indium metal was used, considering that the cathode is already a source of lithium.

On the other hand, for the cathodes based on non-lithiated (charged state) sulfides, i.e. CuS, S and MoS₂, indium-lithium alloy was adopted as the source of lithium. The corresponding negative electrode was then attached to the electrolyte side of the cathode-electrolyte pellet and the stack was sealed in a 13 mm Swagelok cell. Figure 2-2 exhibits the schematic diagram of ASSLBs assembled as described above.

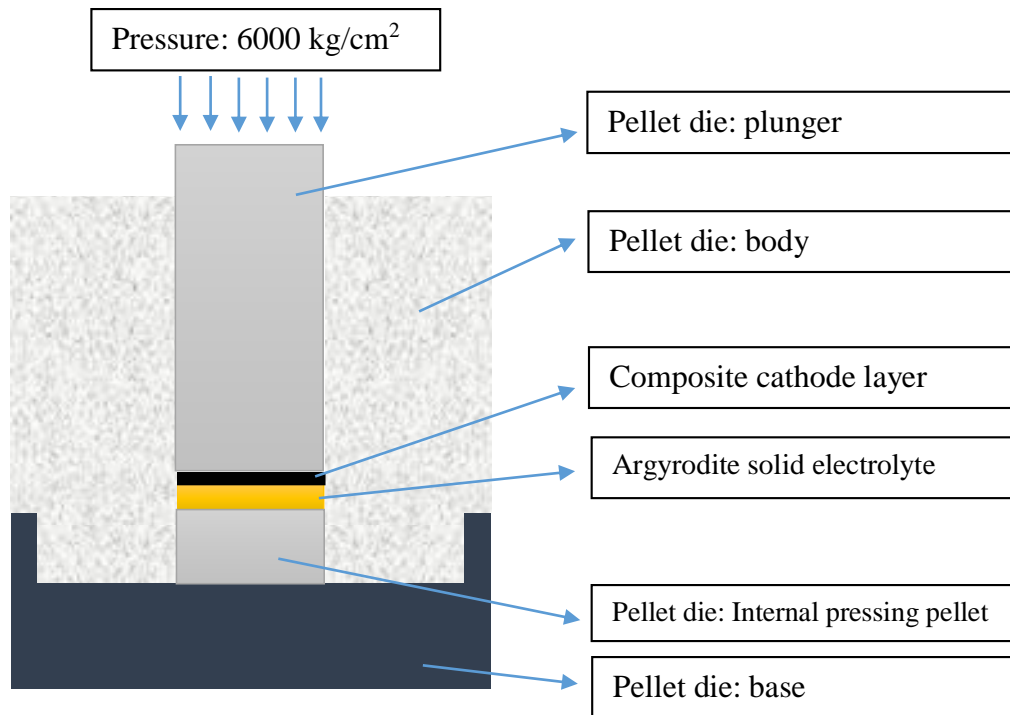


Figure 2-1 Schematic diagram of preparing the pellet of the respective composite cathode powder and the solid electrolyte using 13 mm pressing die set.

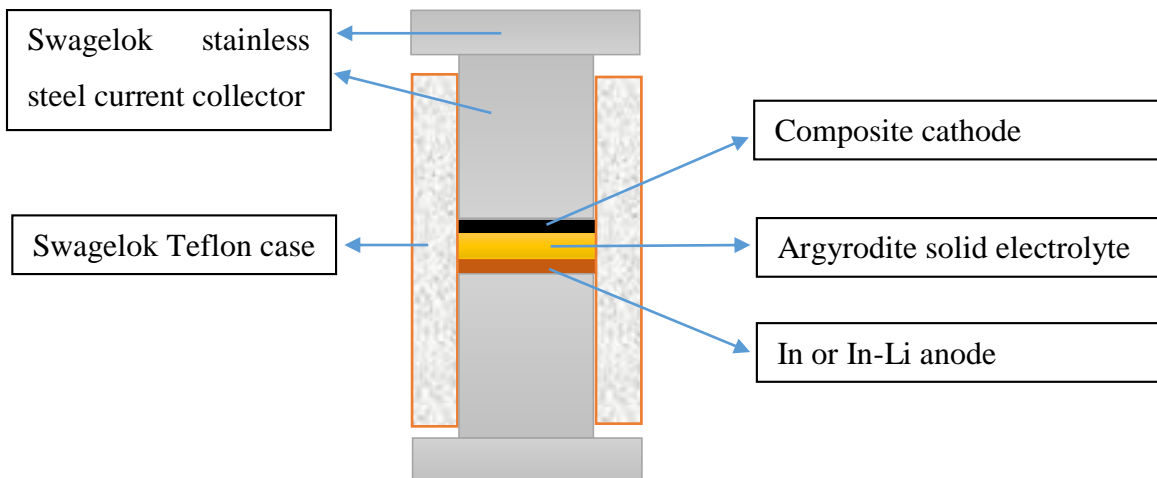


Figure 2-2 Schematic diagram of assembly of ASSLBs in Swagelok cell.

2.4 Characterization Methods

2.4.1 X-ray Diffraction (XRD)

XRD is one of the most widely used methods for structure characterization. To study the structure of argyrodites as well as to monitor structural changes of active materials and argyrodites solid electrolyte during cycling, XRD measurements were conducted using a high resolution X-ray powder diffractometer (Bruker D8 Advance) with Cu K_{α} radiation (weighted average wavelength: 0.15418 nm), equipped with a fast linear detector (X'Celerator). To protect the samples from moisture and air, samples were pelletized in the glove box with diameter larger than 13 mm, mounted on a piece of glass, covered by a Mylar film, and sealed with epoxy, as shown in Figure 2-3. During the measurement, XRD data were collected in the 2θ range of 10° to 100° , with a nominal scan rate of 0.75 s/step and a step size of 0.02° . To correct the broad Mylar peaks in the resulting XRD patterns, XRD data of an individual piece of Mylar film were collected under the same measurement conditions, with a zero diffraction plate as the sample holder. This allowed to subtract the Mylar film pattern from the XRD data of the samples. Adding a constant background corresponding to the integrated intensity of the Mylar peaks ensured that the quality measures of Rietveld refinement for the resulting patterns were not biased by this subtraction.

Phase formation of $\text{Li}_6\text{PS}_5\text{Br}$ was investigated by in situ X-ray powder diffraction (PANalytical, X'Pert Pro MPD) using Cu K_{α} radiation equipped with a high temperature chamber (ANTON PAAR, HTK 1200). The $\text{Li}_6\text{PS}_5\text{Br}$ ball-milled precursors was pelletized and transferred to the chamber of the XRD with N_2 protective atmosphere. Thereafter, the sample was heated to 250°C at a rate of $5^{\circ}\text{C}/\text{min}$, and then cooled down at a rate of $20^{\circ}\text{C}/\text{min}$. XRD measurement was performed with a temperature interval of 10°C . The 2θ range is 10° to 80° .

Rietveld refinement was employed for quantitative analysis of the XRD data, using the generalized structure analysis system (GSAS)¹⁷⁷ with the graphical user interface EXPGUI¹⁷⁸.

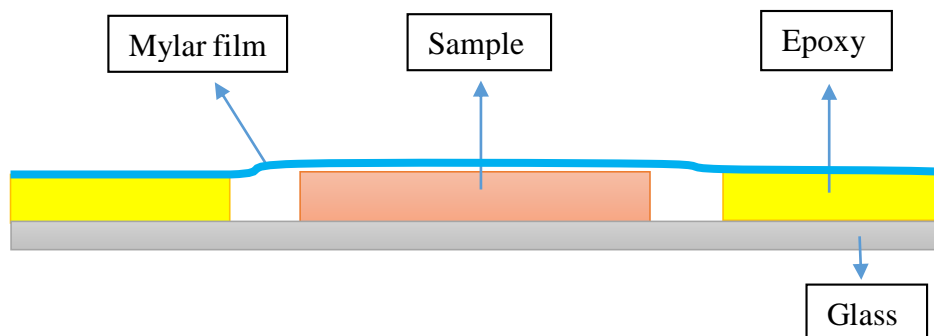


Figure 2-3 Schematic diagram of sealing of sample for ex-situ XRD measurement.

2.4.2 Neutron Powder Diffraction (NPD)

Formation of $\text{Li}_6\text{PS}_5\text{Cl}$ during heat treatment was monitored by *in-situ* neutron diffraction using the high resolution diffractometer, Echidna, at the Australian Nuclear Science and Technology Organization (ANSTO) with a wavelength of $1.54072(2) \text{ \AA}$ (determined using NBS 676 Al_2O_3 standard) at room temperature. Before measurement, the ball-milled samples were pelletized, sealed in a 9 mm vanadium can under argon atmosphere and then transferred to the instrument. During measurement, NPD data were collected every minute, while the samples were heated up to $550 \text{ }^\circ\text{C}$. Quantitative analysis of the NPD data was conducted using GSAS with graphical user interface EXPGUI.

2.4.3 Scanning Electron Microscopy (SEM)

The morphologies of samples were studied by Field-Emission Scanning Electron Microscopy (Zeiss Supra 40 VP). Since most of the samples are air-sensitive and hygroscopic, to limit exposure time of the samples to air during sample transfer, the samples were stuck on the sample holder with carbon tape and kept in a sealed container in the glove box, under the protection of Ar atmosphere. The container, together with the samples, was then transported to the SEM room. Thereafter, the samples were taken out immediately from the container and mounted in the SEM chamber, followed by chamber evacuating.

2.4.4 Transmission Electron Microscopy (TEM)

Existence of Mo metal nanoparticles in MoS_2 cathodes after cycling was confirmed using TEM (JEOL 2000FX). The MoS_2 composite cathode powder at charged state after 100

cycles was placed into deionized water (DI water) and sonicated for 1 min. By this treatment the water-soluble lithium compounds in the composite cathode powder, such as solid electrolyte $\text{Li}_6\text{PS}_5\text{Br}$ and Li_2S , will be dissolved, leaving behind the components insoluble in water (e.g. C, Mo, MoS_2 , if they exist). The resulting solution was centrifuged and the insoluble black residue was used for TEM measurement.

2.4.5 Electrochemical Impedance Spectroscopy (EIS)

Ionic conductivity of argyrodites was measured using EIS (Schlumberger Solartron SI1260) in a frequency range of 10 MHz to 1 Hz. Argyrodite powder was pelletized by cold pressing at a pressure of 6000 kg/cm² into pellets of 10 mm diameter and about 3 mm thickness. The pellets were then employed to assemble Pt/ $\text{Li}_6\text{PS}_5\text{X}$ /Pt cells using a Kiel type cell (Ionic Systems) in the glove box. Throughout the impedance measurement, Ar gas flow was supplied to the Kiel cell.

The impedance data were analyzed using the Frequency Response Analyzer (FRA) software. The equivalent circuit used to fit was shown in Figure 2-4. There, R_1 represents the bulk resistance (bulk capacitance could not be measured in the available frequency range), R_2 is the grain boundary resistance, Q represents the non-ideal double layer capacitance, and W is the Warburg impedance representing ionic diffusion.

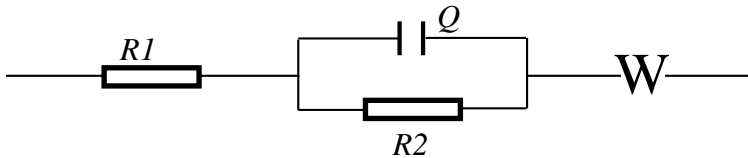


Figure 2-4 Equivalent circuits used to fit the impedance data

As the electronic conductivity in Argyrodites is known to be negligible⁸⁵, the ionic conductivity can be calculated from the bulk resistance R_1 using the equation below:

$$\sigma = \frac{l}{\pi r^2 R_1} \quad (2.1)$$

where σ is the ionic conductivity of the sample, l and r are the thickness and radius of the pellet, respectively.

Activation energy E_a for lithium ionic conduction was then obtained from conductivities σ measured at different temperatures T by Arrhenius equation:

$$\ln(\sigma T) \propto -\frac{E_a}{k} \frac{1}{T} \quad (2.2)$$

k is the Boltzmann constant.

2.4.6 Electrochemical cycling

The electrochemical stability of argyrodites was studied by cyclic voltammetry (CV) using a potentiostat/galvanostat (Arbin BT2000). The $\text{Li}_6\text{PS}_5\text{X}$ powder were pelletized by cold pressing with a diameter of 13 mm and assembled as a stainless-steel/ $\text{Li}_6\text{PS}_5\text{Br}$ /Li cell. The potential sweeps were applied with a scanning rate of 2 mV/s from -0.5 V to 4 V.

To study the electrode reaction, CV measurements were performed on ASSLBs using various cathode materials at a scanning rate of 0.02 mV/s.

Galvanostatic cyclic performance of ASSLBs was investigated using the potentiostat/galvanostat. The applied current values were adjusted based on the targeted C rate of the active materials. For a C rate of 1 C the current is chosen to theoretically fully discharge or charge a battery within one hour. Correspondingly, for a current density of 1C the discharging or charging of a battery should take 1h (if the battery reaches the theoretical capacity), while for C/10 it takes 10h. It should be noted that all the current densities and specific capacities mentioned in Chapter 4-7 were calculated based on the weight of the respective active materials, unless indicated specifically. All voltages discussed in this manuscript are to be understood with respect to Li/Li^+ , unless pointed out specially. The potential of indium vs. Li/Li^+ is 0.6 V.

Chapter 3 PROPERTIES OF LITHIUM ARGYRODITES $\text{Li}_6\text{PS}_5\text{X}$

Lithium argyrodites $\text{Li}_6\text{PS}_5\text{X}$ have attracted considerable attention due to their high ionic conductivity and wide electrochemical window. However, the dependence of their structure and electrochemical properties on the preparation conditions has yet to be investigated. The preparation methods have not yet been optimized. In this chapter, phase formation of the lithium argyrodites starting from the ball-milled samples was monitored, and the reliance of the structure on the heat treatment history will be discussed (section 3.1). The variation of conductivity as a function of the annealing temperature, which is traced back to a change in stoichiometry and halide distribution (as will be shown in section 3.2).^{179,180} The structure, electrochemical stability and morphology of the resulting lithium argyrodite fabricated at the optimized temperature will be demonstrated in sections 3.3, 3.4 and 3.5, respectively.¹⁸¹ Efforts to improve the chemical stability of lithium argyrodite will be presented in section 3.6.

3.1 Phase formation during heat treatment

To monitor the phase formation of argyrodite during heating treatment, *in-situ* neutron powder diffraction (NPD) was performed by our group starting from ball-milled $\text{Li}_6\text{PS}_5\text{Cl}$ precursor.^{179,180} Before the measurement, the $\text{Li}_6\text{PS}_5\text{Cl}$ ball-milled precursor was pelletized and sealed in a 9 mm vanadium can under argon atmosphere. Thereafter, the sample was heated from room temperature to 150 °C at a rate of 1.5 °C/min, held at that temperature for 20 min, then further heated with the same heating rate up to 550 °C and finally cooled down to 90 °C. Throughout this heat treatment, NPD diffractograms were collected every minute.

Figure 3-1(a) shows the 2-D intensity color map representation of the *in-situ* NPD patterns for the formation of $\text{Li}_6\text{PS}_5\text{Cl}$ from its ball-milled precursors. The solid black line indicates the variation of temperature with time. Selected NPD patterns in Figure 3-1(a) are shown in Figure 3-1(b). Before the heat treatment, the ball-milled precursor mixture was partially amorphous with minor crystalline Li_2S and LiCl . With increasing temperature, argyrodite started to form around 80 °C, and became dominant at 150 °C, where Li_2S vanished already.

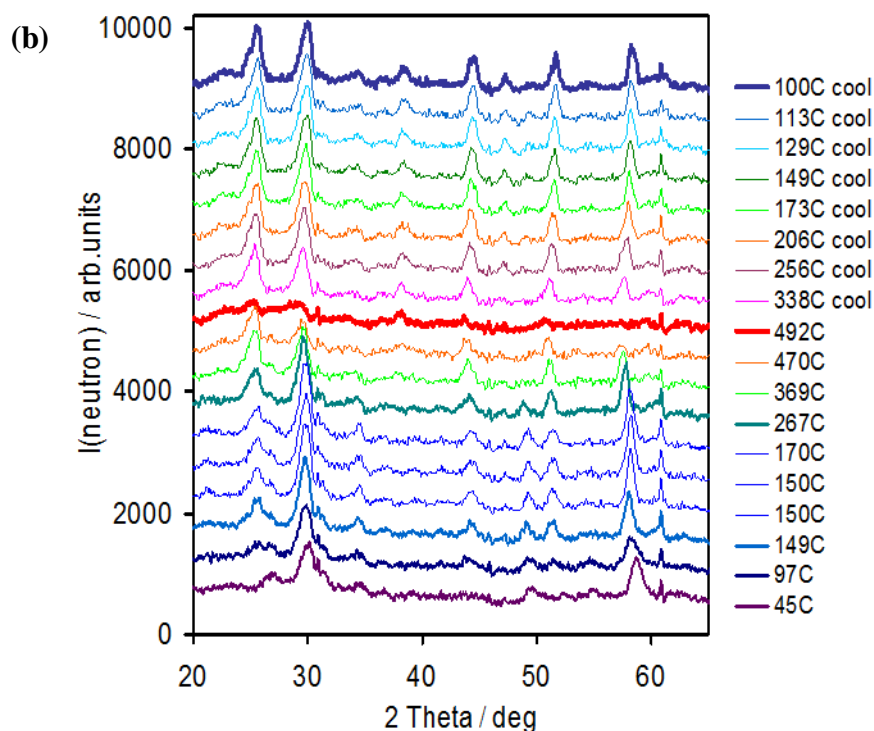
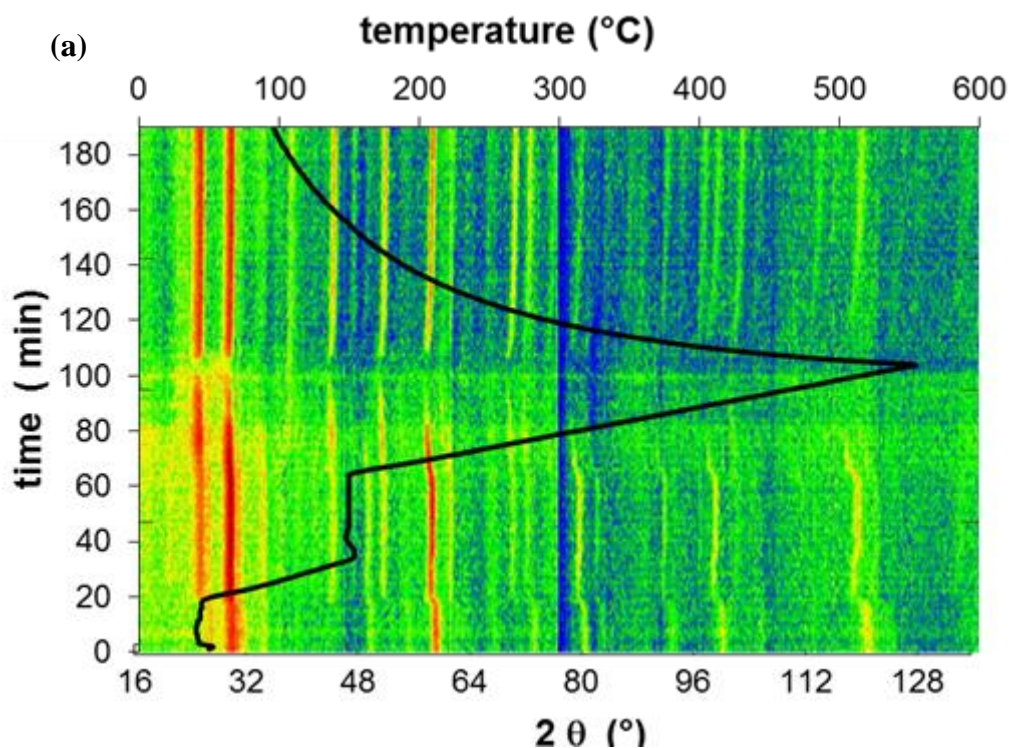


Figure 3-1 (a) 2-D intensity color map of in-situ NPD pattern during the phase formation of $\text{Li}_6\text{PS}_5\text{Cl}$ from ball-milled precursors. The changes of color from blue to red represent the increase of intensity. The solid black line demonstrates the variation of temperature with time during the measurement. (b) Detailed NPD patterns at selective temperature extracted from in-situ NPD results in (a).¹⁷⁹

On the other hand, peaks corresponding to LiCl disappeared at 190 °C. Further increasing the temperature to 490 °C, however, led to amorphization/melting of the sample. During cooling, argyrodite phase crystallized again.

Comparing the NPD patterns of argyrodite at the beginning of heating (low temperature) to those at high temperature, intensity and position of individual peaks vary significantly. While some variation in the peak position is to be expected from thermal expansion during heating, the observed changes in peak intensities already suggest that $\text{Li}_{7-x}\text{PS}_{6-x}\text{Cl}_x$ argyrodite formed at various temperatures should not be of identical structure. This could be tentatively ascribed to the variation in argyrodite stoichiometry most probably with respect to the halide content x (and the correlated lithium content). Concerning that scattering length of Cl (9.577 fm) and S (2.847 fm) are significantly different, these two elements should be distinctly distinguishable from NPD results (while Cl^- and S^{2-} are isoelectronic and hence practically undistinguishable in X-ray diffraction studies). Therefore, Rietveld refinement should be helpful in solving the structures of argyrodite $\text{Li}_{7-x}\text{PS}_{6-x}\text{Cl}_x$. Refinement results of NPD patterns at low temperature indicated that essentially no Cl is incorporated in the first argyrodite phase formed at the beginning of the heating cycle, leading to Li_7PS_6 . In contrast, around 490 °C (before amorphization of argyrodite) Cl content increased to a stoichiometric argyrodite phase with $x \approx 1$, i.e. $\text{Li}_6\text{PS}_5\text{Cl}$. The close matching of the refined structure model with experimental NPD patterns supports the proposed formation of argyrodites with different Cl content during heat treatment.

Figure 3-2 shows the details of refinement results, revealing the temperature dependence of lattice parameter a , fraction of Cl on site Cl(2) and total Cl content x . The red diamonds and blue triangles represent the data corresponding to heating and cooling, respectively. As shown in Figure 3-2 (a), at the beginning of the formation of argyrodites, the lattice parameter a is larger than reported values for $\text{Li}_{7-x}\text{PS}_{6-x}\text{Cl}_x$ by Kong et al.⁸⁰ In contrast, the values are closer to that expected by interpolating between literature data for the cubic high temperature modification of Li_7PS_6 (HT- Li_7PS_6) and the pseudo-cubic lattice parameter of the orthorhombic LT- Li_7PS_6 . On heating the increase of the lattice parameter a exhibits an unusual non-linearity above 190 °C. The slower increase of a might suggest a second order phase transition. Above 350 °C, the thermal expansion trend becomes linear again. On

cooling the same trend is maintained down to 320 °C, followed by only a slight change of the slope at lower temperatures. Although the sample was cooled to 90 °C in this in-situ measurement, the refined lattice constants closely match the reported lattice parameter for $\text{Li}_{7-x}\text{PS}_{6-x}\text{Cl}_x$ at room temperature (23 °C) when factoring in the thermal expansion trend.

As mentioned above, a major advantage of NPD studies is that the Rietveld refinements of these data can even yield the variation of Cl/S site occupancies and hence the overall halide content x as a function of temperature as shown in Figure 3-2 (b). Below 190 °C, Cl could hardly be detected. However, when the temperature exceeds this point, the Cl content rapidly increases and approaches $x=1$ above 430 °C, in line with the slope change of the temperature-dependent lattice parameters shown in Figure 3-2 (a). During cooling, this Cl-uptake is partially reversed reaching $x\approx 0.5$ around 320 °C. On further cooling the refined Cl content slightly increases again and then stabilizes at a value of $x\approx 0.65$. Thus it has to be expected that the Cl content can be controlled by varying the annealing temperature and possibly also by the cooling rate.

Figure 3-2 (c) exhibits the fraction of Cl on the site Cl(2) to total Cl in argyrodites at different heating/cooling temperature. Position Cl(1) represents the site $3/4, 3/4, 3/4$, while position Cl(2) represents the sites $0, 0, 0$. Around 200 °C, where Cl-containing argyrodites start to form, most of the Cl atoms are residing at the Cl(1) site. With the increase in annealing temperature, the fraction of Cl atoms residing on Cl(2) rapidly increases and reaches 50% around 350 °C. During cooling, the fraction of Cl on site Cl(2) keeps on increasing (while the overall Cl content somewhat reduces as discussed above), resulting in a value around 60% at the end of the cooling cycle. Hence, it appears that for kinetic reasons Cl uptake occurs mainly onto the Cl(1) site, while on annealing the thermodynamically preferable Cl occupancy of the Cl(2) site increases.

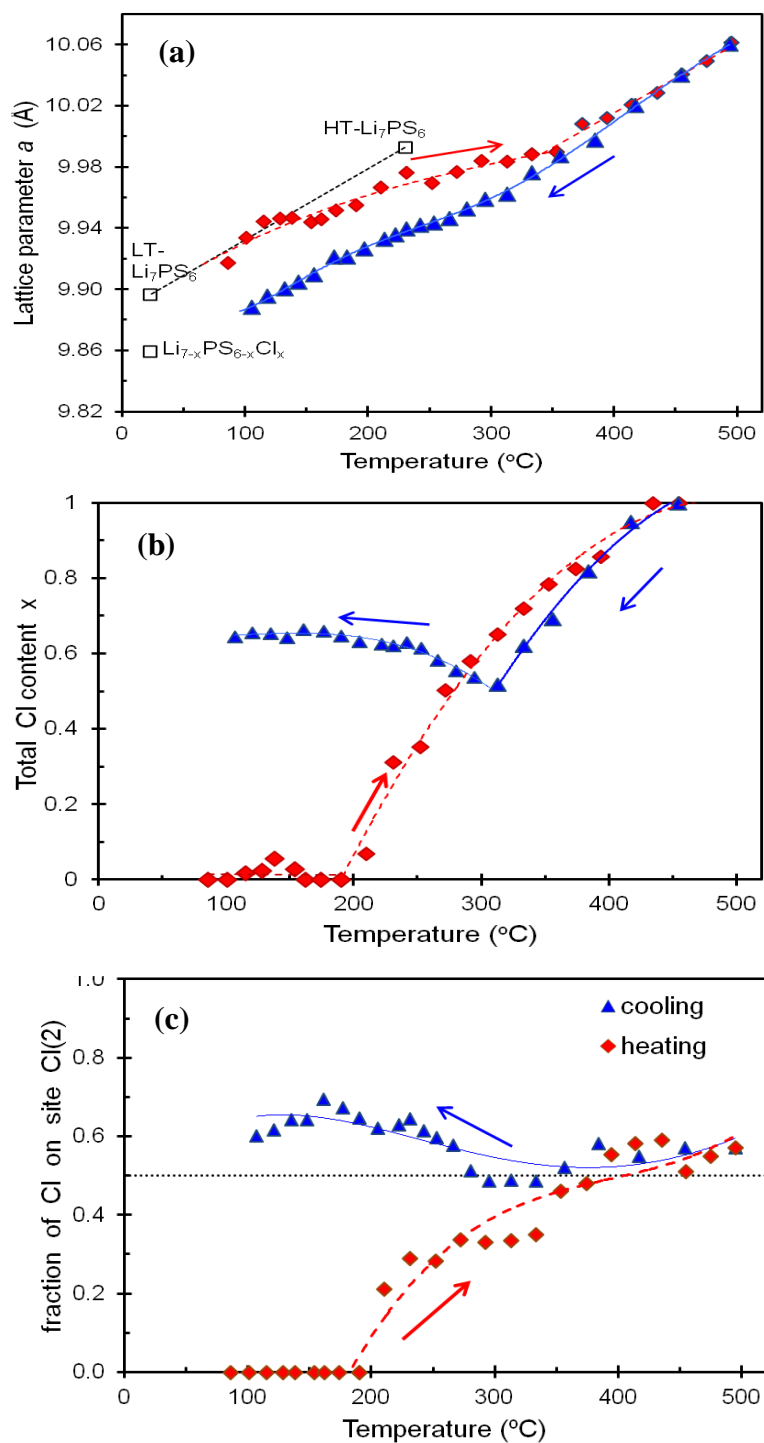


Figure 3-2 Rietveld refinement results of NPD demonstrating the temperature dependences of (a) lattice parameter a , (b) Cl content x in the main argyrodite phase $\text{Li}_{7-x}\text{PS}_{6-x}\text{Cl}_x$, and (c) Cl distribution (fraction of Cl residing in position Cl(2) to total Cl in argyrodites). In all the figures, the red diamonds represent data during heating, while the blue triangles represent data during cooling.¹⁷⁹ The open squares in figure (a) are data from literature for $\text{Li}_{7-x}\text{PS}_{6-x}\text{Cl}_x$, low-temperature modification of Li_7PS_6 (LT- Li_7PS_6) and high-temperature modification of Li_7PS_6 (HT- Li_7PS_6), as denoted in the figure⁸⁰.

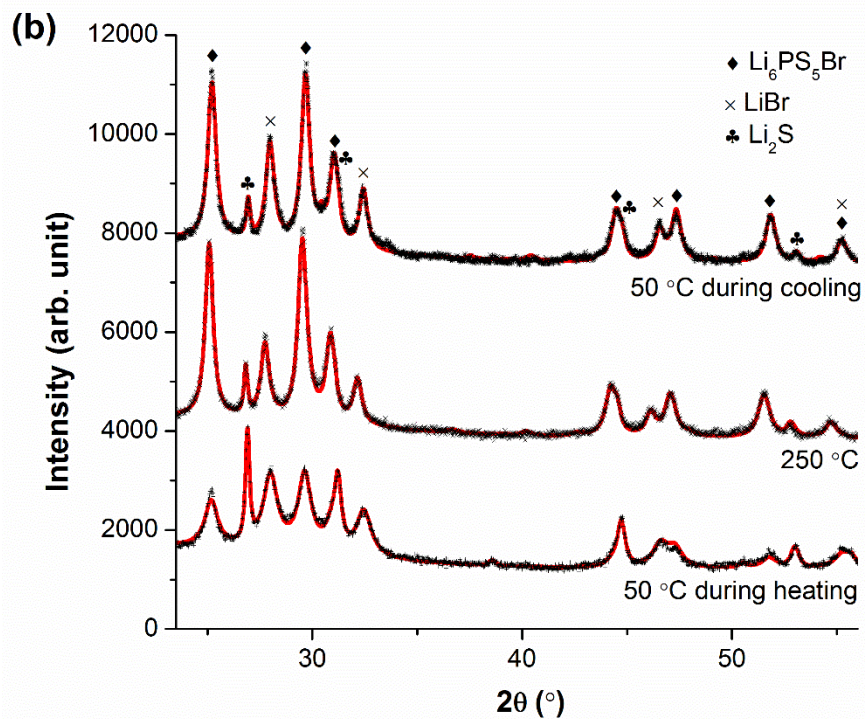
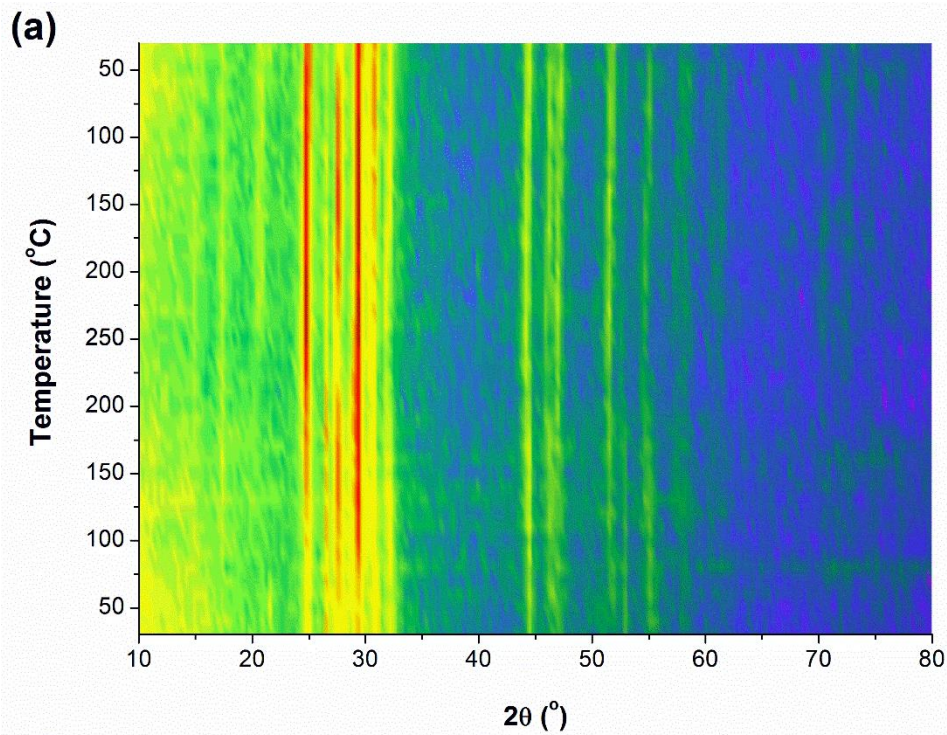


Figure 3-3 (a) 2-D intensity color map of in-situ XRD patterns during the phase formation of $\text{Li}_6\text{PS}_5\text{Br}$ from ball-milled precursors. The changes of color from blue to red represent the increase of intensity. (b) Rietveld refinement results of the samples at the beginning of heating ($50\text{ }^{\circ}\text{C}$), at the maximum temperature ($250\text{ }^{\circ}\text{C}$) and at the end of cooling ($50\text{ }^{\circ}\text{C}$).

Similarly, *in-situ* XRD measurement of a ball-milled $\text{Li}_6\text{PS}_5\text{Br}$ precursor mixture was performed to monitor the phase formation during heat treatment. The sample was heated to $250\text{ }^\circ\text{C}$ at a rate of $5\text{ }^\circ\text{C}/\text{min}$, and then cooled down to room temperature. XRD measurement was taken in a temperature interval of $10\text{ }^\circ\text{C}$. Figure 3-3 shows the 2-D intensity color map of *in-situ* XRD patterns, and the refinement results at selected stages (at the beginning of heating ($50\text{ }^\circ\text{C}$), the end of heating ($250\text{ }^\circ\text{C}$) and the end of cooling ($50\text{ }^\circ\text{C}$)). Even at the early stage of heating ($50\text{ }^\circ\text{C}$), a substantial amount of Br-containing argyrodite could be observed besides Li_2S and LiBr . With the increase in temperature, the peak intensities of Li_2S and LiBr rapidly decrease, while those of argyrodite considerably increased, suggesting that more argyrodites formed during the heat treatment. Rietveld refinement of the XRD patterns revealed that the Br content gradually increases during heating, reaching a maximum value of $x \approx 0.69$ for $\text{Li}_{7-x}\text{PS}_{6-x}\text{Br}_x$ at $250\text{ }^\circ\text{C}$, which is similar to what observed for $\text{Li}_{7-x}\text{PS}_{6-x}\text{Cl}_x$ sample. During cooling, the Br uptake slightly reduced. Over the heating cycle the Br-distribution gradually evolved from Br almost exclusively on the Br(2) site to a more equilibrated distribution.

3.2 Conductivity vs. annealing temperature

In the previous section 3.1, phase formation of $\text{Li}_6\text{PS}_5\text{Cl}$ and $\text{Li}_6\text{PS}_5\text{Br}$ starting from the ball-milled precursors was discussed. Halide content and ordering of argyrodites were found to be altered with the variation of annealing temperature. Considering that ordering is a key factor that influences ionic conductivity of ionic conductors, it should be plausible to hypothesize that annealing temperature should play a significant role in the achievable ionic conductivity of the resulting argyrodites. In this section, ionic conductivity of $\text{Li}_6\text{PS}_5\text{Cl}$ and $\text{Li}_6\text{PS}_5\text{Br}$ at various annealing temperature will be investigated.^{179,180}

Ionic conductivity of argyrodites was measured by electrochemical impedance spectroscopy (EIS) using Pt/ $\text{Li}_6\text{PS}_5\text{X}$ ball-milled precursor/Pt cell in the frequency range of 10MHz to 1Hz. The samples were heated to various temperatures, i.e. $150\text{ }^\circ\text{C}$, $200\text{ }^\circ\text{C}$ and $250\text{ }^\circ\text{C}$, and then cooled down to room temperature and heated again. Impedance data were collected with a temperature interval of $10\text{ }^\circ\text{C}$, with a stabilization time of 20 min for

each temperature. Bulk resistance, total resistance and thus ionic conductivity were obtained by fitting the impedance data, as mentioned in section 2.4.5.

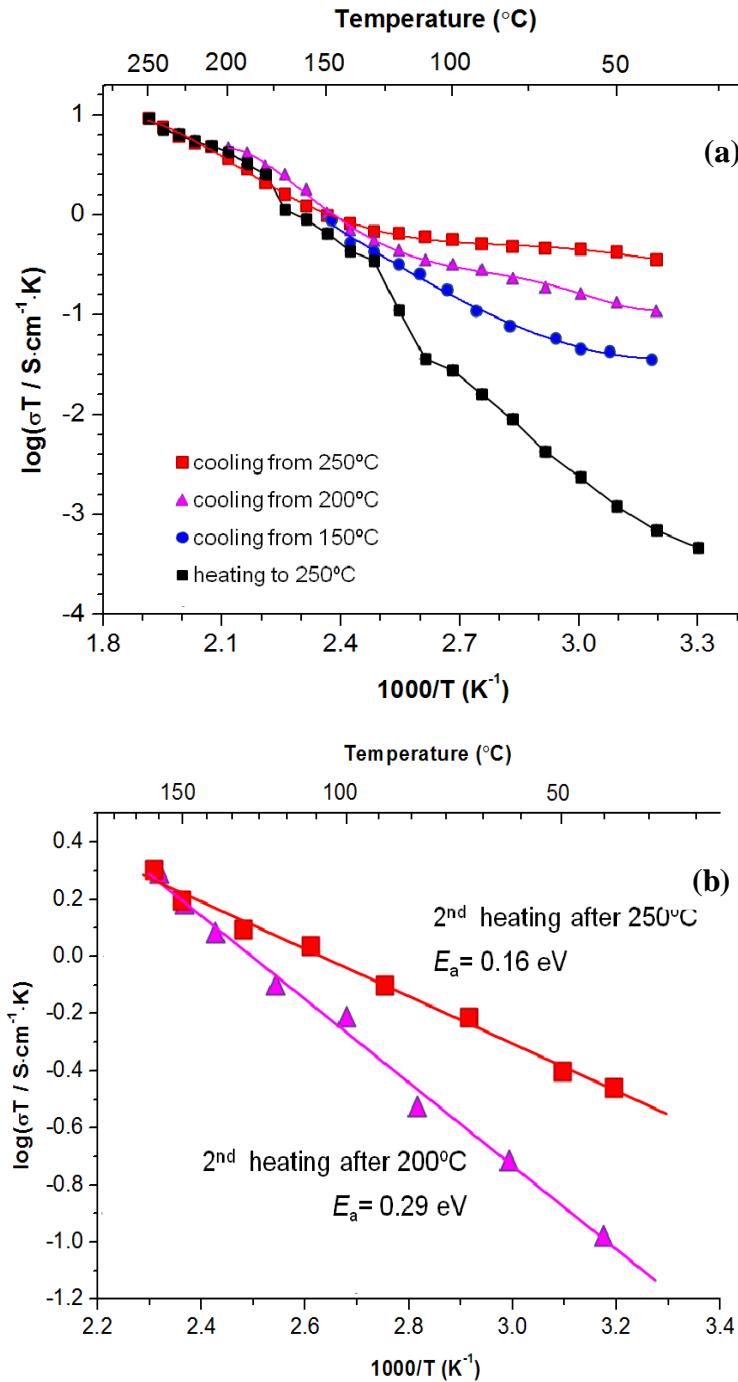


Figure 3-4 (a) Arrhenius plot of the ionic conductivity of $\text{Li}_6\text{PS}_5\text{Cl}$ heating to various temperatures, i.e. 150 $^{\circ}\text{C}$, 200 $^{\circ}\text{C}$, and 250 $^{\circ}\text{C}$, and their relevant cooling curves. For the heating curve, to avoid duplication, only the curve heating to 250 $^{\circ}\text{C}$ is shown. (b) Arrhenius plot of the ionic conductivity of $\text{Li}_6\text{PS}_5\text{Cl}$ at the 2nd heating. The samples were annealed at different temperatures during the 1st heat treatment, i.e. 200 $^{\circ}\text{C}$ and 250 $^{\circ}\text{C}$.¹⁷⁹

Figure 3-4 (a) shows the temperature dependence of the ionic conductivity of $\text{Li}_{7-x}\text{PS}_{6-x}\text{Cl}_x$ starting from ball-milled precursors and heated up to various annealing temperatures (150 °C, 200 °C, and 250 °C) in the form of Arrhenius plots. As the heating curves of the three annealing temperature overlap in the shared temperature range, to avoid duplication, only the heating curve corresponding to 250 °C is shown (dark squares). As indicated in the *in-situ* NPD (section 3.1), at the beginning of heat treatment (30 °C), the ball-milled precursor was partially amorphous with little or no argyrodite phase present. Correspondingly, the initial ionic conductivity of the sample was only 3×10^{-5} S/cm. When the temperature was increased to ~110 °C, ionic conductivity rapidly increased, due to the formation of argyrodite phase. Above 180 °C, the rate of conductivity increase slows down, which could be tentatively ascribed to the rapid incorporation of Cl into the argyrodite in the intermediate temperature range, forming $\text{Li}_{7-x}\text{PS}_{6-x}\text{Cl}$. At 250 °C, an ionic conductivity as high as 2×10^{-2} S/cm could be obtained.

Regarding to the cooling cycle, cooling curves with respect to different annealing temperatures (150 °C, 200 °C, and 250 °C) are shown as blue round dots, pink triangles and red squares respectively in Figure 3-4 (a). With the increase of annealing temperature, room temperature ionic conductivity of argyrodite significantly increased, from 1.1×10^{-4} S/cm (150 °C), 3.6×10^{-4} S/cm (200 °C) to 1.1×10^{-3} S/cm (250 °C). Meanwhile, the activation energy (E_a) reduced at higher temperature. To minimize the influence of variation of Cl content/distribution during cooling (see Figure 3-2), activation energy was evaluated by the Arrhenius curves of the second heating, as shown in Figure 3-4 (b). The activation energy drops drastically from 0.29 eV for the sample annealed at 200 °C, to 0.16 eV for the sample annealed at 250 °C.

Recalling from the previous section (section 3.1) that lattice parameter and halide content and distribution vary with the annealing temperature, the increase in ionic conductivity and the decrease of activation energy can be ascribed to these structural differences among argyrodite phases prepared at different annealing temperatures.

3.3 Structure

Based on the discussion in sections 3.1 and 3.2, it can be concluded that lattice parameter, halide content and distribution and thereby room temperature ionic conductivity of $\text{Li}_6\text{PS}_5\text{X}$ depend on the annealing temperature. While heating the argyrodites to a temperature more than 430 °C leads to the halide content $x=1$, x will still decrease during cooling. Therefore, an annealing temperature of 550 °C, as originally reported by Kong et al.⁸⁰, is not necessary for achieving a phase with high ionic conductivity. Considering that around 300 °C the Cl content is already close to the room temperature product of $\text{Li}_6\text{PS}_5\text{Cl}$ heated up to 550 °C ($x \approx 0.65$, as shown in Figure 3-2 (b)), the heat treatment temperature could be reduced to 300 °C. The revised fabrication processes for $\text{Li}_6\text{PS}_5\text{X}$ (X=Cl, Br) can therefore be described as follows: stoichiometric mixtures of Li_2S , P_2S_5 and LiX are ball milled at a rotating speed of 500 rpm for 20 h. The as-prepared precursor mixture is pelletized and annealed at 300 °C for 5h.

A Rietveld refinement of XRD data for a sample of $\text{Li}_6\text{PS}_5\text{Br}$ prepared in this way is shown in Figure 3-5. $\text{Li}_6\text{PS}_5\text{Br}$ was successfully fabricated, with only a minute amount of LiBr . The lattice constant of $\text{Li}_6\text{PS}_5\text{Br}$ is 9.9748(1) Å, slightly smaller than the literature data (9.988(2) Å)⁸⁴ for $\text{Li}_{6.192}\text{PS}_{5.24}\text{Br}_{0.757}$. Atomic coordinates (x, y, z), site occupancy (n) and isotropy atomic displacement (Uiso) of $\text{Li}_6\text{PS}_5\text{Br}$ are listed in the Table 3-1. Anion sites (1), i.e. 4d ($\frac{3}{4}, \frac{3}{4}, \frac{3}{4}$), is mainly occupied by S atoms (73%), while anion site (2), i.e. 4a (0, 0, 0), is dominantly occupied by Br atoms (72%). The actual composition of this sample is therefrom $\text{Li}_{6.01}\text{PS}_{5.01}\text{Br}_{0.99}$ with little Br deficit, while the phase $\text{Li}_{6.192}\text{PS}_{5.24}\text{Br}_{0.757}$ reported by Deiseroth et al.⁸⁴ exhibits a more prominent deviation from stoichiometry, which might also be the reason for the slight difference in the lattice constants between these two samples.

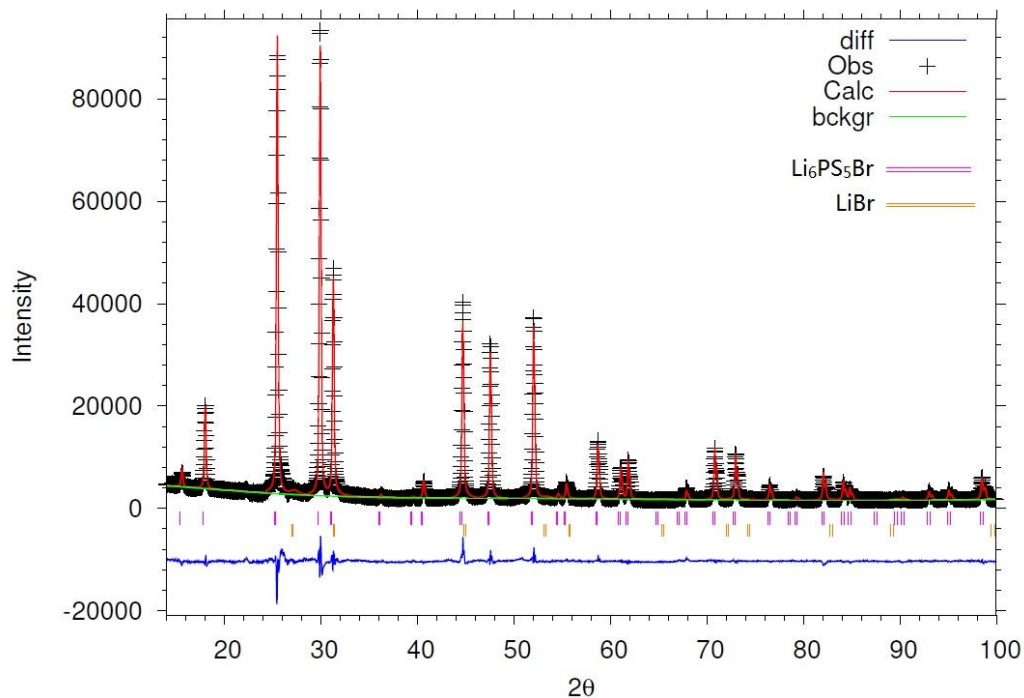


Figure 3-5 Rietveld refinement of XRD data for $\text{Li}_6\text{PS}_5\text{Br}$ ($R_{wp} = 6.3\%$)

Table 3-1 Atomic coordinates, site occupancy factors (n) and isotropic atomic displacement parameters (U_{iso}) of $\text{Li}_6\text{PS}_5\text{Br}$ obtained from Rietveld refinement using XRD and neutron data.

	x	y	z	n	$U_{iso} (\text{Å}^2)$
Li(1)	0.3110	0.0176	0.6890	0.44	0.019
Li(2)	0.2500	0.0029	0.7500	0.13	0.076
P	0.0000	0.5000	0.0000	1	0.024
S(1)	0.7500	0.7500	0.7500	0.73	0.032
Br(1)	0.7500	0.7500	0.7500	0.27	0.032
S(2)	0.0000	0.0000	0.0000	0.28	0.036
Br(2)	0.0000	0.0000	0.0000	0.72	0.036
S(3)	0.1217	-0.1217	0.6217	1	0.037

3.4 Electrochemical stability

Electrochemical stability of $\text{Li}_6\text{PS}_5\text{Br}$ was evaluated by cyclic voltammetry.¹⁸¹ The only two distinct peaks in Figure 3-6, correspond to the cathodic deposition of lithium metal (0V to -0.5V) and its anodic dissolution (0 V to 0.7 V), indicating that $\text{Li}_6\text{PS}_5\text{Br}$ is essentially stable over the entire voltage range from -0.5 V to 4 V. However, there is a very small broad peak around 2 V, probably caused by the oxidation of free S^{2-} ions, as the oxidation potential of the free S^{2-} ions is calculated to be 2.2 V vs. Li/Li^+ .¹⁸² The small feature around 4 V might correspond to the oxidation of free Br^- ions.

Similarly, a wide electrochemical window for $\text{Li}_6\text{PS}_5\text{Cl}$ is reported in ref.¹⁸³. On the other hand, DFT studies by Holzwarth et al.¹⁸⁴ and our group suggest that $\text{Li}_6\text{PS}_5\text{Cl}$ is only metastable with respect to decomposition into Li_3PS_4 , Li_2S , and LiCl .

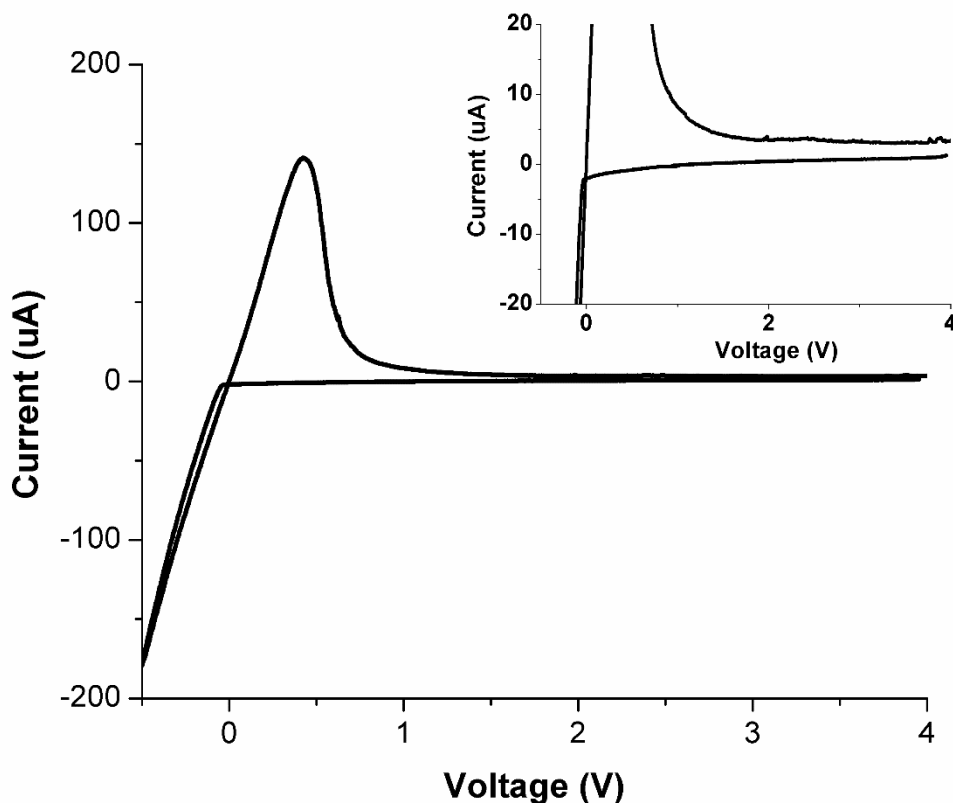


Figure 3-6 Cyclic voltammogram of $\text{Li}/\text{Li}_6\text{PS}_5\text{Br}/\text{stainless steel}$ cell at a scanning rate of 2 mV/s between -0.5 V and 4 V. Inset: enlarged voltammogram in the current range -20 μA to 20 μA .

3.5 Morphology

Figure 3-7 shows the SEM image of a $\text{Li}_6\text{PS}_5\text{Br}$ pellet. The annealed $\text{Li}_6\text{PS}_5\text{Br}$ pellet was mortar-ground and pelletized at a pressure of 6000 kg/cm^2 before the SEM analysis. Mortar-ground μm -sized $\text{Li}_6\text{PS}_5\text{Br}$ particles were aggregated after pelletization, leaving the individual crystallites with a size up to 100 nm (as the contrast in the SEM image). No distinct holes or gaps appeared on the pellet. Therefore, the pellet should be sufficiently compact to effectively separate the electrodes and prevent short-circuiting of the battery.

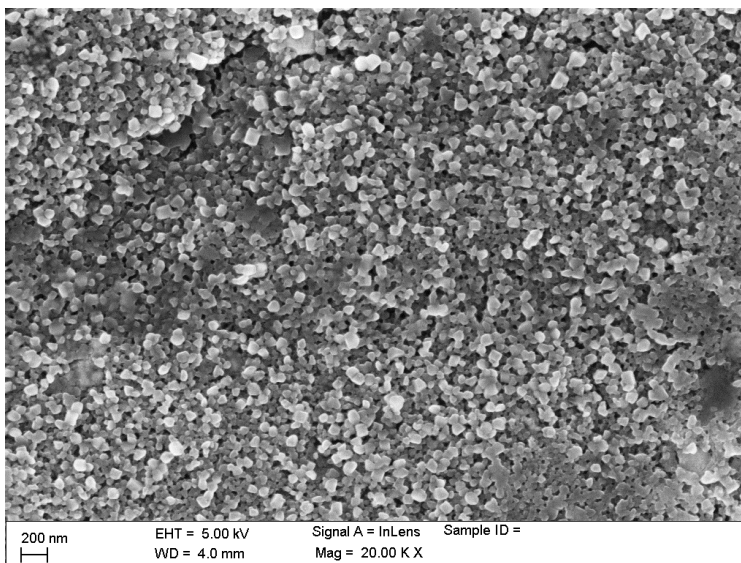
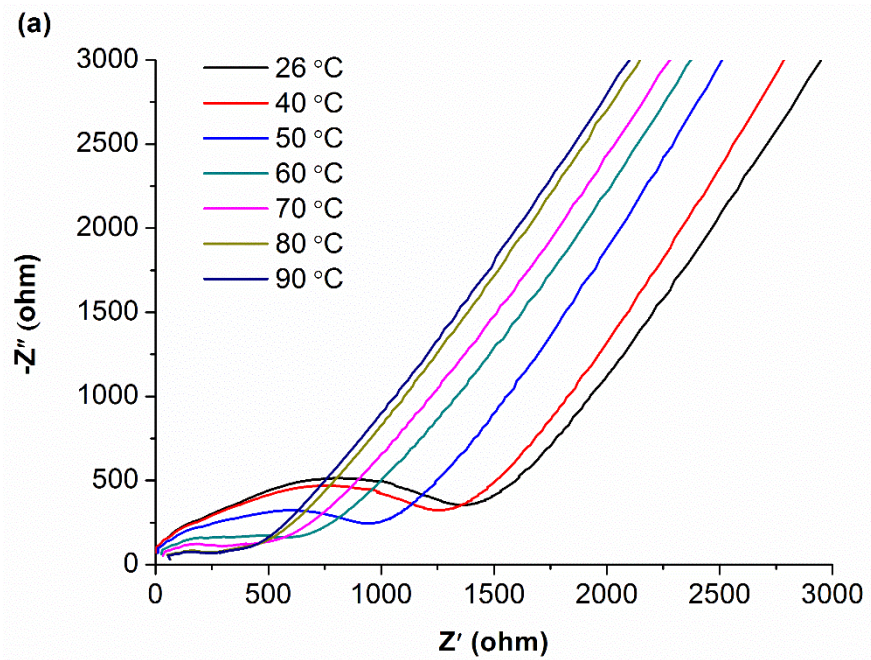


Figure 3-7 SEM image of a $\text{Li}_6\text{PS}_5\text{Br}$ pellet

3.6 Chemical stability

Most of the thiophosphate solid electrolytes, including lithium argyrodites, are sensitive to moisture (and to a lower extent to oxygen). As a consequence, an inert atmosphere is required during the fabrication, storage and application of argyrodites. The ASSLBs need to be properly protected from (humid) air, which may be a serious limiting factor for industrial application of argyrodites in lithium-based batteries. Improvement of chemical stability of argyrodites will, therefore, simplify the fabrication of argyrodites, enhance the cyclability and shelf life of the ASSLBs, and widen the application to other lithium-based batteries.

Here enhancement of the chemical stability of lithium argyrodites was explored by mixing the crystalline $\text{Li}_6\text{PS}_5\text{Br}$ with ZnO nanoparticles in a molar ratio of $\text{Li}_6\text{PS}_5\text{Br}:\text{ZnO}=10:1$, leading to $10\text{Li}_6\text{PS}_5\text{Br}-\text{ZnO}$. Metal oxides such as ZnO that can react with H_2S gas (generated when the thiophosphate is exposed to humid air) and form water-stable sulfides may be expected to reduce H_2S release and improving the practical chemical stability of thiophosphate-based solid electrolytes. Figure 3-8 shows the Nyquist plots of the impedance data of $10\text{Li}_6\text{PS}_5\text{Br}-\text{ZnO}$ at various temperatures and the Arrhenius plot of the total ionic conductivity. At room temperature, the bulk ionic conductivity is $7.6 \times 10^{-4} \text{ S/cm}$ while the total conductivity is $1.4 \times 10^{-4} \text{ S/cm}$, suggesting that adding ZnO has only a minor detrimental effect on the ionic conductivity of lithium argyrodites. Based on the Arrhenius plot of the total ionic conductivity, the activation energy of the $10\text{Li}_6\text{PS}_5\text{Br}-\text{ZnO}$ is 0.22 eV, which is similar to that of crystalline lithium argyrodite, as discussed in section 3.2.



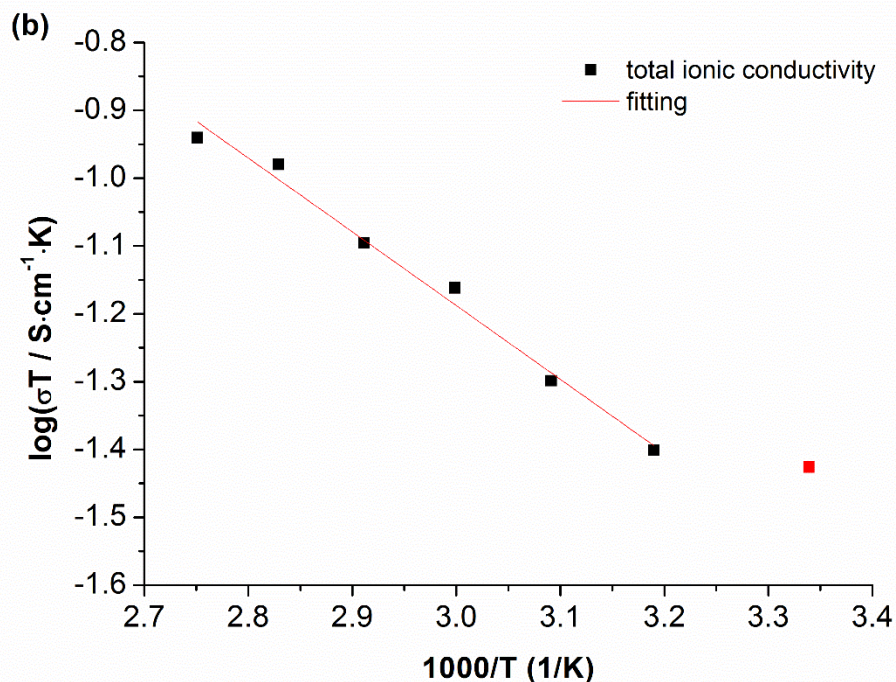


Figure 3-8 (a) Nyquist plots of the impedance data and (b) Arrhenius plot of the total ionic conductivity of the $10\text{Li}_6\text{PS}_5\text{Br-ZnO}$ sample. The frequency scale is 10 MHz to 5 kHz.

Hydrolysis of $10\text{Li}_6\text{PS}_5\text{Br-ZnO}$ was studied by measuring the impedance of the sample before and after exposure to air for 2 min and 5 min. As shown in Figure 3-9, the resistance of the sample significantly decreased with exposure time. By visual observation, the sample surface already became wet within one minute of exposure time. The increase of conductivity should therefrom be ascribed to the hydrolysis of the surface of the sample. Accordingly, adding ZnO into $\text{Li}_6\text{PS}_5\text{Br}$ is not significantly improving the hydrolysis of lithium argyrodite. These findings are in contrast to the reports by Hayashi et al.¹⁸⁵ who claimed that adding M_xO_y (e.g. ZnO, Fe_2O_3 , Bi_2O_3) into Li_3PS_4 glass greatly improves the chemical stability against humid air. While it may be correct that the metal oxides can absorb the generated H_2S gas when Li_3PS_4 glass is exposed to the air and then form metal sulfides (and this report actually employs the amount of H_2S as the measure to quantify the hydrolysis stability), absorbing the H_2S formed by the hydrolysis seems not to be an effective way in mitigating further decomposition reaction (unless the produced metal sulfides form a dense protective film on the thiophosphate). Therefore, the reasons for the claimed improved chemical stability of $\text{Li}_3\text{PS}_4\text{-M}_x\text{O}_y$ but the inefficiency of the same approach in mitigating fast hydrolysis of $10\text{Li}_6\text{PS}_5\text{Br-ZnO}$ need to be further investigated.

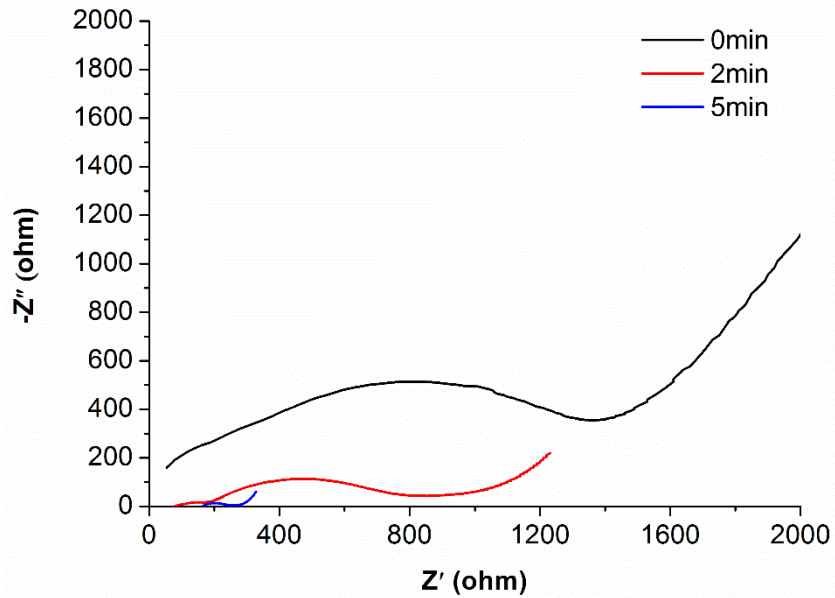


Figure 3-9 Nyquist plot of the $10\text{Li}_6\text{PS}_5\text{Br-ZnO}$ sample before exposure and after exposed to the air for 2 min and 5 min. The measurements were performed at room temperature with a frequency range of 10 MHz to 5 kHz.

Chapter 4 ALL-SOLID-STATE BATTERIES USING CUS OR CU-LI₂S AS CATHODE

Despite of the high ionic conductivity and high electrochemical stability of lithium argyrodites Li₆PS₅X (X=Cl, Br) (as discussed in Chapter 3), there are few studies on realizing ASSLBs using argyrodites solid electrolyte, among which none is employing sulfide cathodes. In this chapter, ASSLBs using Li₆PS₅Br solid electrolyte in combination with CuS or Cu-Li₂S cathode will be studied.^{181,186} Effects of original states of composite cathodes on the battery performance will be investigated in section 4.1, including the way to prepare the composite cathode (section 4.1.1), and the original states of dis/charge of the batteries (section 4.1.2). To gain a deeper understanding of the capacity fading of the batteries, reaction mechanism of CuS in the ASSLBs, especially interaction of CuS with Li₆PS₅Br during cycling, will be studied in section 4.2. Thereafter, reasons for the capacity fading of the ASSLBs will be discussed in section 4.3.

4.1 Effects of Original States of Composite Cathodes

4.1.1 Composite cathodes prepared by mortar grinding or ball milling

The morphologies of composite cathode powders prepared by mortar grinding or ball milling were studied using SEM. As shown in Figure 4-1, composite cathode powder prepared by mortar grinding shows argyrodite and copper particles with a diameter larger than 5 μm surrounded by smaller particles (Li₂S, C) of around 1 μm. Ball milling could effectively reduce the particle size of argyrodite, leaving copper particles of up to 5 μm as the largest particles (Fig. 3c). EDX analysis revealed that the mortar-ground sample still contained large carbon particles, while the carbon distribution in ball-milled composites was much more uniform, probably due to the exfoliation of carbon during ball milling.

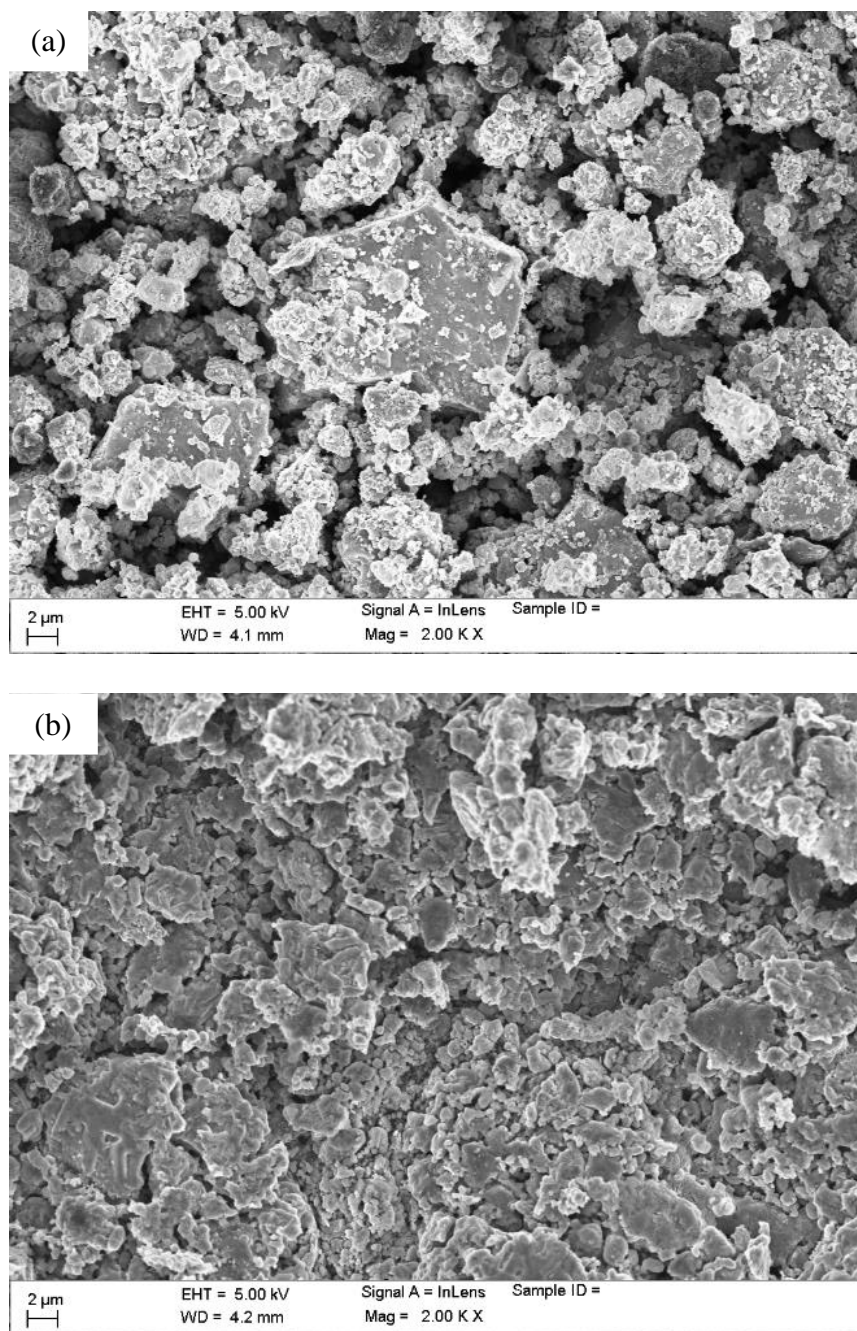


Figure 4-1 SEM images of composite cathode powders prepared by (a) mortar grinding and (b) ball milling.

Room temperature cyclic performances of all-solid-state Cu-Li₂S/Li₆PS₅Br/In batteries with composite cathode materials prepared by mortar grinding and ball milling were determined between 0.65 V and 3.1 V vs. Li/Li⁺ (0.05 – 2.5 V vs. In-Li) at a current density of 50 mA/g based on the weight of Cu-Li₂S (C/10, corresponding to ca. 442 μ A/cm²). Charging and discharging curves of the resulting batteries during the first cycle are shown

in Figure 4-2 (a). The battery using the mortar-ground composite cathode had a practical initial charge capacity of 380 mAh/g and discharge capacity of 310 mAh/g, whereas ball-milling of the cathode composite greatly increases the practically achievable specific charge and discharge capacity of the battery to 500 mAh/g and 445 mAh/g respectively, and reduces the overpotential. The initial charge capacity is slightly larger than the theoretical capacity of 490 mAh/g. The excess charge capacity may tentatively be ascribed to a minor oxidation of S^{2-} ions as suggested by the cyclic voltammogram in Figure 3-6. The enhanced initial capacity may be traced back to the reduced particle size and higher uniformity after ball milling. Contact among the components in the composite cathode powder, i.e. Cu-Li₂S, Li₆PS₅Br and carbon, is improved and thus the substantial volume changes of Cu-Li₂S during charging and discharging should be slightly less damaging, so that more of the cathode materials remain active, making it possible to achieve higher practical capacity.

During the initial discharging, two pronounced plateaus at around 2.0 and 1.5 V vs. Li/Li⁺ are observed for the battery with ball-milled composite cathode in agreement with reports by Hayashi et al.¹⁸⁷. However, their batteries achieved higher capacity over 490 mAh/g because of the non-stoichiometric mixture of Cu and Li₂S.

Figure 4-2 (b) compares the variation of the discharge capacity over the first 20 cycles for the ASSLBs with composite cathode prepared by mortar grinding and ball milling. The initial discharge capacity of the battery with ball-milled composite cathode (445 mAh/g) was 135 mAh/g higher than that of the battery with mortar-ground cathode. However, the higher initial charge and discharge capacity also mean larger volume change of the cathode materials during charge and discharge, so that the reversible capacities of both batteries in subsequent cycles were similar, dropping to ca. 70 mAh/g over 20 cycles. Thus ball milling clearly increases the initial capacity of the battery, but has no significant effect on the reversible capacity.

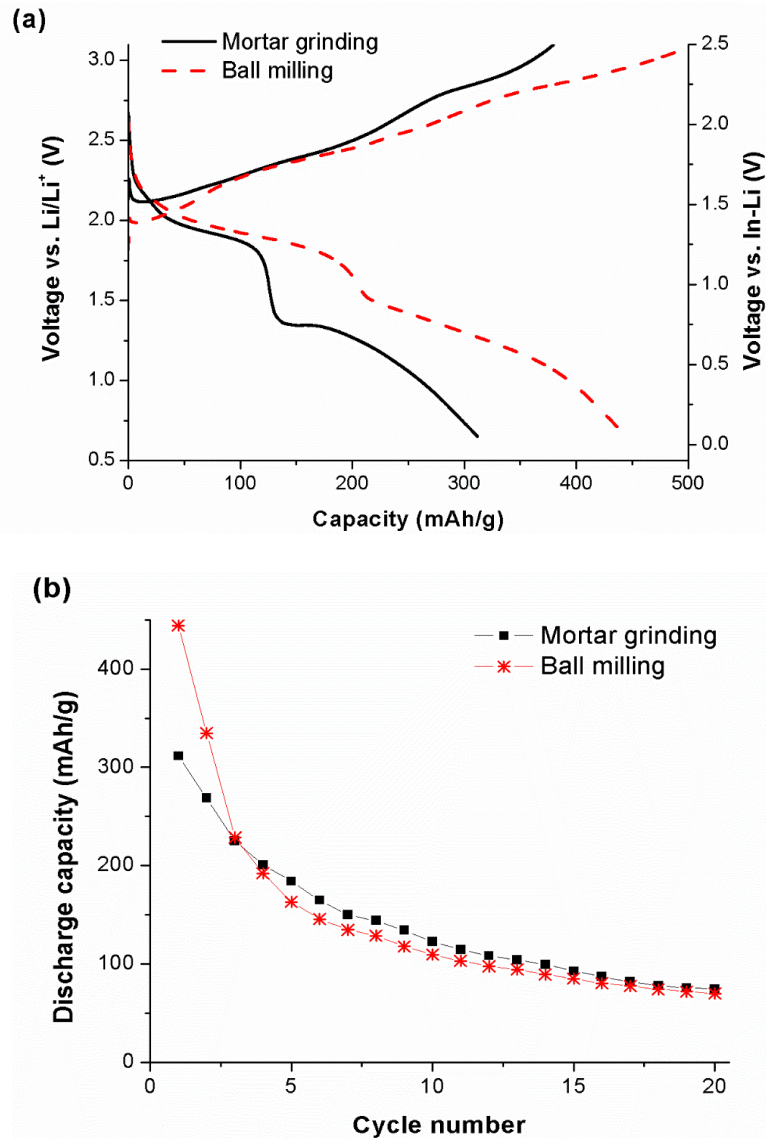


Figure 4-2 (a) Charging and discharging curves and (b) discharge capacity of the first 20 cycles of all-solid-state $\text{Cu-Li}_2\text{S/Li}_6\text{PS}_5\text{Br/In}$ batteries with composite cathodes prepared by mortar grinding and ball milling. The current density is 50 mA/g ($C/10$) and the voltage range is 0.65 V to 3.1 V vs. Li/Li^+ ($0.05 - 2.5 \text{ V}$ vs. In-Li).

Rate performance of the all-solid-state $\text{Cu-Li}_2\text{S/Li}_6\text{PS}_5\text{Br/In}$ battery was then characterized by studying the battery performance under varying charge/discharge rates of $C/2$, $C/5$, $C/10$, $C/20$ and $C/50$. The charging and discharging current was set to be the same and changed every 5 cycles. The resulting discharge capacity of the battery is shown in Figure 4-3. For the highest C rate $C/2$ (250 mA/g), the battery based on mortar-ground composite cathodes showed slightly increased specific capacity with prolonged cycling and a discharge capacity of 80 mAh/g was observed at the 5th cycle. Given that most of this capacity was

contributed by the first stage of the discharge, while most of the volume change is caused by the second conversion stage, less volume change and hence less damage was done to the battery during the first 5 cycles (For the reaction mechanisms of CuS cathodes see section 4.2). On the other hand, coarse particles broke down into smaller particles during cycling, which under the existing compression allowed for an improved contact, leading to the increase of capacity. Lowering the current density led to a recovery of the capacity to 235 mAh/g, 225 mAh/g, 230 mAh/g and 240 mAh/g at C rates of C/5, C/10, C/20 and C/50 respectively. For the battery using ball-milled composite cathode cycling at C/2, a four times higher initial discharge capacity of 105 mAh/g was achieved, suggesting that ball milling could greatly help with high rate performance. However, for these batteries the capacity started to fade from the second cycle already, since the higher capacity partly originated from the conversion reaction and the associated volume change started to damage the battery. Lowering the C rates again increases the capacity of the battery.

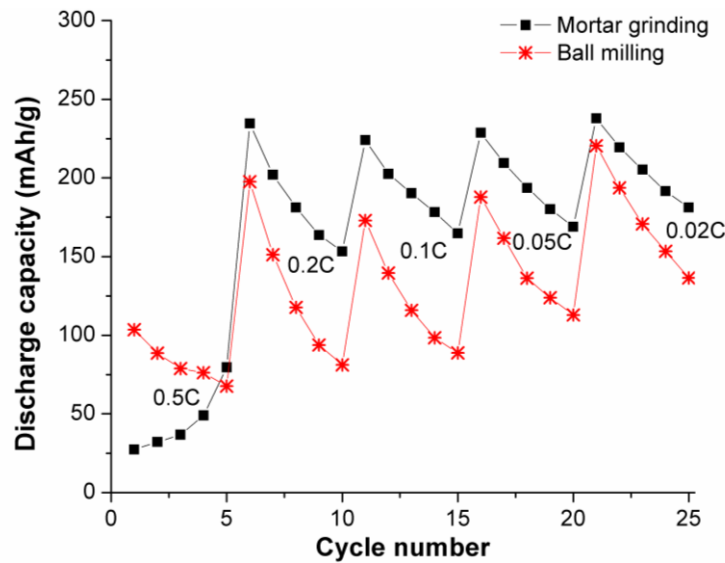


Figure 4-3 Discharge capacity of ASSLBs with composite cathodes prepared by mortar grinding and ball milling charged and discharged at various C rates, i.e. C/2, C/5, C/10, C/20 and C/50. The charge and discharge current was set to be the same and changed every 5 cycles.

Discharge curves of the battery using mortar-ground composite cathode at various C rates are shown in Figure 4-4(a). Two discharge plateaus at the voltage of 1.9 V and 1.3 V could be seen at a C rate of C/5, representing the two-step reaction of CuS. With the reduction of cycling rate, the second plateau gradually vanished while the first plateau grew. When the discharge rate was reduced to C/50 after 20 cycles, the second plateau totally disappeared.

The first plateau contributed to a discharge capacity of about 210 mAh/g, 85% of the theoretical capacity (245 mAh/g), i.e. about 0.85 Li^+ was inserted into the CuS during the first step of discharging. When the battery was cycling at the same C rate of C/10 (see Figure 4-4 (b)), a similar reduction of the second plateau could also be observed. Such a phenomenon of a fast decay of the conversion step while maintaining nearly full capacity for the intercalation step was also observed by Hayashi et al.¹⁸⁸.

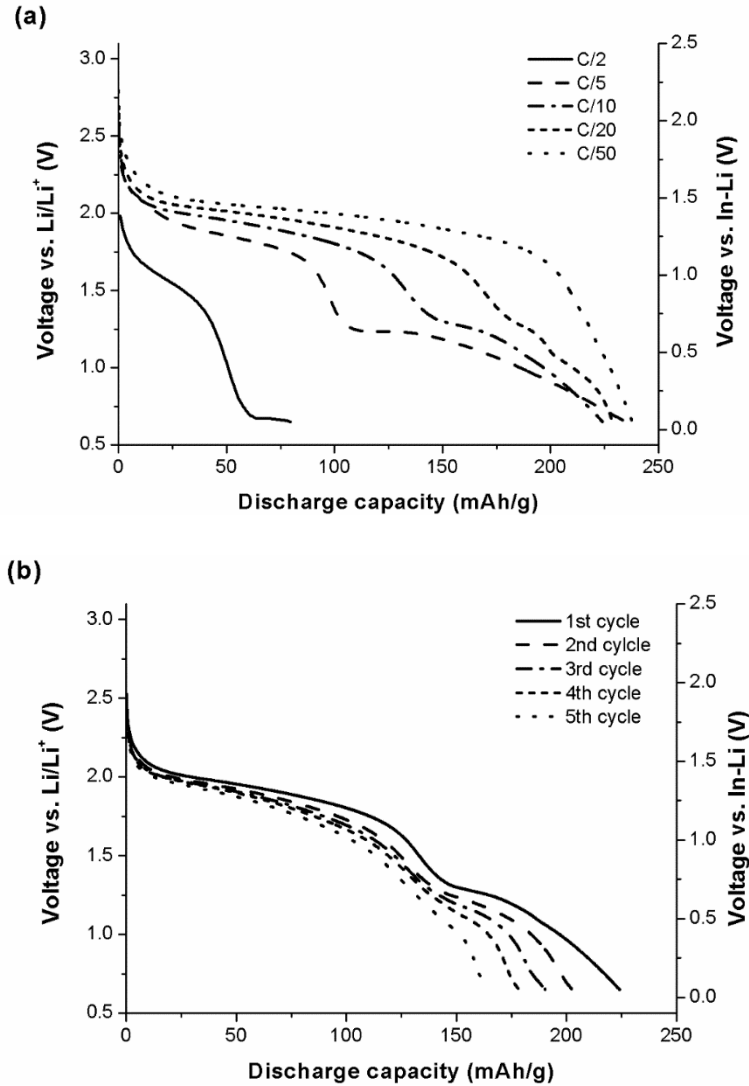


Figure 4-4 (a) Discharge curve of the battery using mortar-ground composite cathode during the cycling experiment shown in Figure 4-3; (b) Detailed cycling data for the mortar-ground sample at C/10 rate (cycles 11-15) from the experiment as shown in Figure 4-3.

4.1.2 Battery assembly in charged or discharged state

In the previous section (4.1.1), we discussed the effects of preparation methods of composite Cu-Li₂S cathode, i.e. mortar grinding or ball milling, on the cyclic performance of ASSLBs. Cu-Li₂S (discharged state) is the lithiated product of CuS (charged state). In this section, I compare the batteries studied above that were assembled in the discharged state with batteries assembled in the charged state, i.e. using CuS as the starting cathode material. Therefrom it is discussed whether the initial state of charge of the cathode materials affects the cyclic performance of the ASSLBs.

Room temperature performance of all-solid-state CuS/Li₆PS₅Br/In-Li batteries cycling between 0.65 V and 3.1 V at C/50 rate (i.e. current density of 11.2 mA/g corresponding to the weight of CuS) is summarized in Figure 4-5. The battery showed an initial discharge capacity of 650 mAh/g, slightly exceeding the theoretical capacity of CuS (560 mAh/g), the excess capacity of 90 mAh/g (at <1.2 V) can be attributed to interfacial storage in the nano-structured Cu:Li₂S:C:electrolyte composite formed during discharge. The interfacial charging mechanism was introduced in section 1.4.1. Hayashi et al. reported an all-solid-state Cu-S/Li₂S-P₂S₅ glass ceramic/In-Li battery with an even higher initial discharge capacity, but they employ a Cu:S ratio 1:3 ratio in their ball-milled cathode composite, so that the battery effectively becomes a Li/S battery.¹⁸⁹

The first charging capacity of our batteries reached, however, only 250 mAh/g, less than half of the initial discharge capacity. As the second discharge capacity matches the first charge capacity, the rapid capacity fading of the battery has to be ascribed to problems in the charging process: The first discharge plateau is prominently visible in the first discharge cycle, but almost absent in the subsequent discharge cycles. Therefrom it may be assumed that the re-formation of CuS is a critical step. After the 3rd cycle, the battery performance became relatively stable and a reversible capacity of 90 mAh/g was maintained at the 20th cycle.

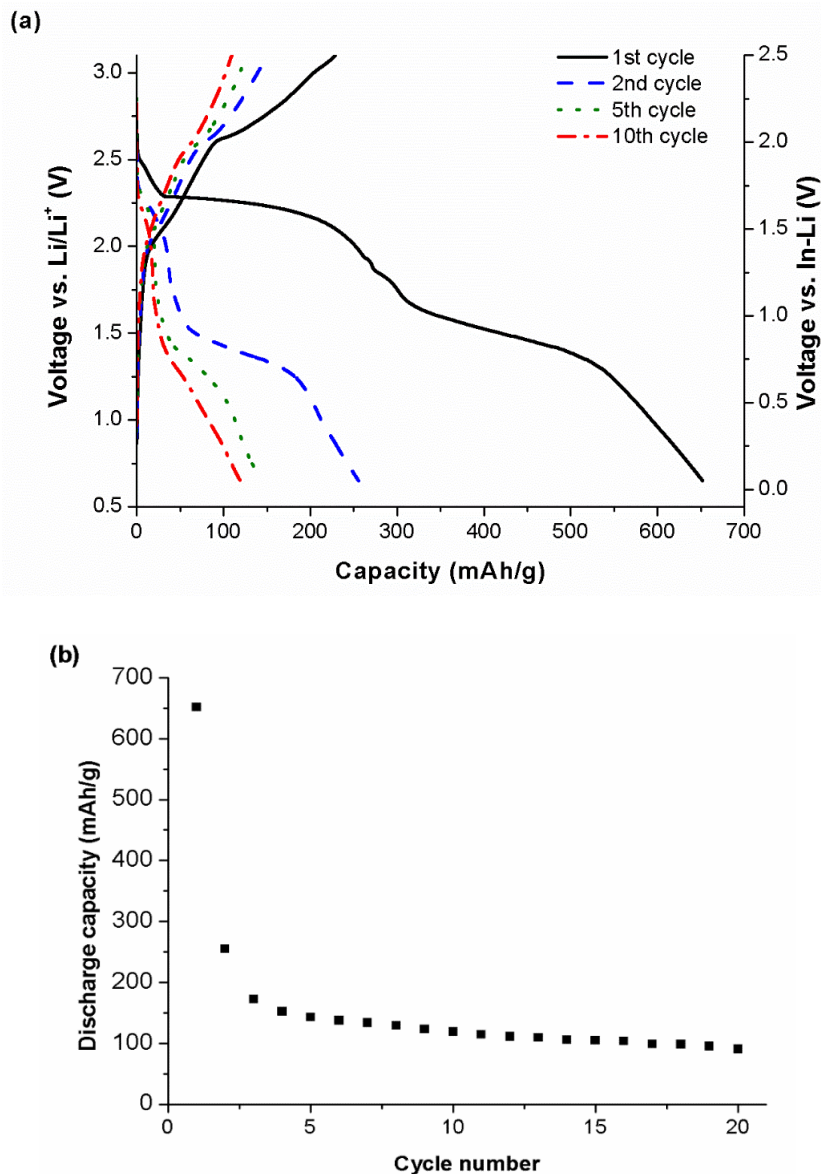


Figure 4-5 (a) Discharge and charge curves and (b) discharge capacity of ASSLB using ball-milled CuS cathode. The battery was cycled between 0.65 V and 3.1 V at a current density of 11.2 mA/g (C/50).

All-solid-state CuS/Li₆PS₅Br/In-Li cells were also tested at a C/10 rate, the same as that used for Cu-Li₂S battery shown in Figure 4-2. A comparison of the cyclic performance of the ASSLBs using CuS or Cu-Li₂S as cathode is shown in Figure 4-6. To make these two batteries at different states comparable, specific capacities were both calculated based on the weight of CuS; in other words, for Cu-Li₂S cathode, the discharge capacity corresponds to the theoretical weight of CuS formed when the cathode is fully charged.

The ASSLB using CuS cathode achieved an initial discharge capacity of 440 mAh/g, but faded rapidly to 85 mAh/g at the second cycle. The reversible discharge capacity was 45 mAh/g up to 20 cycles. Such cyclic performance was by far worse than that of the same battery cycling at a lower C rate of C/50 (see Figure 4-5), suggesting a significant discharge/charge rate dependence of the battery performance. The performance was also substantially inferior to that of ASSLB assembled in discharged state, i.e. Cu-Li₂S, as demonstrated in Figure 4-6. This could be tentatively ascribed to the different nature of the initial volume change of the active material, i.e. volume expansion or shrinkage. It is noted that before cycling, the pellet of cathode and solid electrolyte should be under compressive condition due to the pelletization process. In addition, the battery with CuS cathode will experience a severe volume expansion after the initial discharge. This volume expansion will further increase the internal compressive stress, leading to crack formation and poor capacity retention. In contrast, the Cu-Li₂S cathode will undergo a volume shrinkage first (after the first charge), which could be partially compensated by the internal compressive stress originated from pelletization, resulting in a superior cyclic performance.

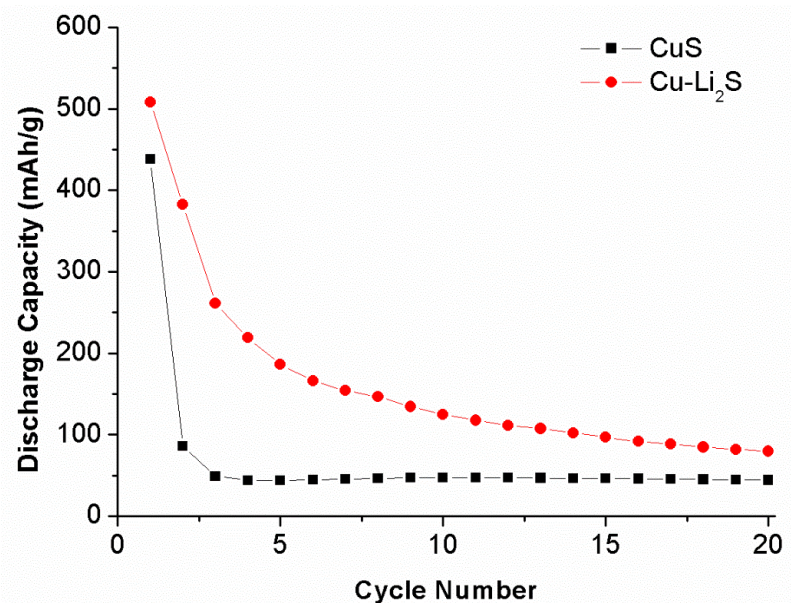


Figure 4-6 Comparison of discharge capacity of ASSLB using ball-milled CuS or Cu-Li₂S as cathode. Both batteries were cycled between 0.65 V and 3.1 V at a rate of C/10 at room temperature. Capacities of both batteries were calculated with respect to the weight of CuS.

4.2 Special Role of Cu⁺ in ASSLBs

To understand the reasons for the capacity fading of ASSLBs using CuS or Cu-Li₂S as cathode materials in combination of Li₆PS₅Br solid electrolyte, it is essential to monitor structural changes of the composite cathode during cycling. However, so far no study has been published on the reaction mechanism of stoichiometric CuS in ASSLBs and no evidence has been presented that solid electrolytes are stable in such kind of batteries (see section 1.4.3). Here, we investigate the structural changes of the CuS composite cathode in all-solid-state CuS/Li₆PS₅Br/In-Li batteries by *ex-situ* XRD.

To this end all-solid-state CuS/Li₆PS₅Br/In-Li batteries were discharged to different stages (0 mAh/g=before discharge, 100 mAh/g, 200 mAh/g, 300 mAh/g and 560 mAh/g=fully discharged) and *ex-situ* XRD measurements were conducted on the resulting composite cathode. The XRD patterns in Figure 4-7 show only two phases at the beginning of the discharge process, i.e. Li₆PS₅Br and covellite-type CuS (*P6₃/mmc*). The small amount of amorphous carbon present in the cathode is not clearly discernible from such patterns. The Bragg peaks of CuS exhibit a significant size broadening due to the effective ball milling of the relatively soft CuS, which helps to shorten the migration path for charge carriers in the cathode and therefore facilitate the electrode reaction. With the progress of discharge, peaks corresponding to CuS are further broadened and reduced in intensity indicating a shrinking size and reduced total amount of CuS crystallites. At the discharge state of 300 mAh/g, CuS could hardly be observed any more.

According to the literature reaction mechanisms^{109,128,129} discussed in the introduction (see section 1.4.3), any Li₂S formation should be accompanied by either the appearance of Cu and/or Cu₂S. However, from the XRD pattern recorded after partial discharge stage of 100 mAh/g, a significant amount of Li₂S could already be noticed, yet without any sign of Cu or Cu₂S. Consequently, a peculiar reaction mechanism has to be considered for CuS in all-solid-state batteries using argyrodite solid electrolytes.

A closer look at the argyrodite peaks then revealed that, while there are no signs of decomposition of the electrolyte into different crystalline or amorphous phases, peak positions and individual peak intensities vary significantly but reversibly over the

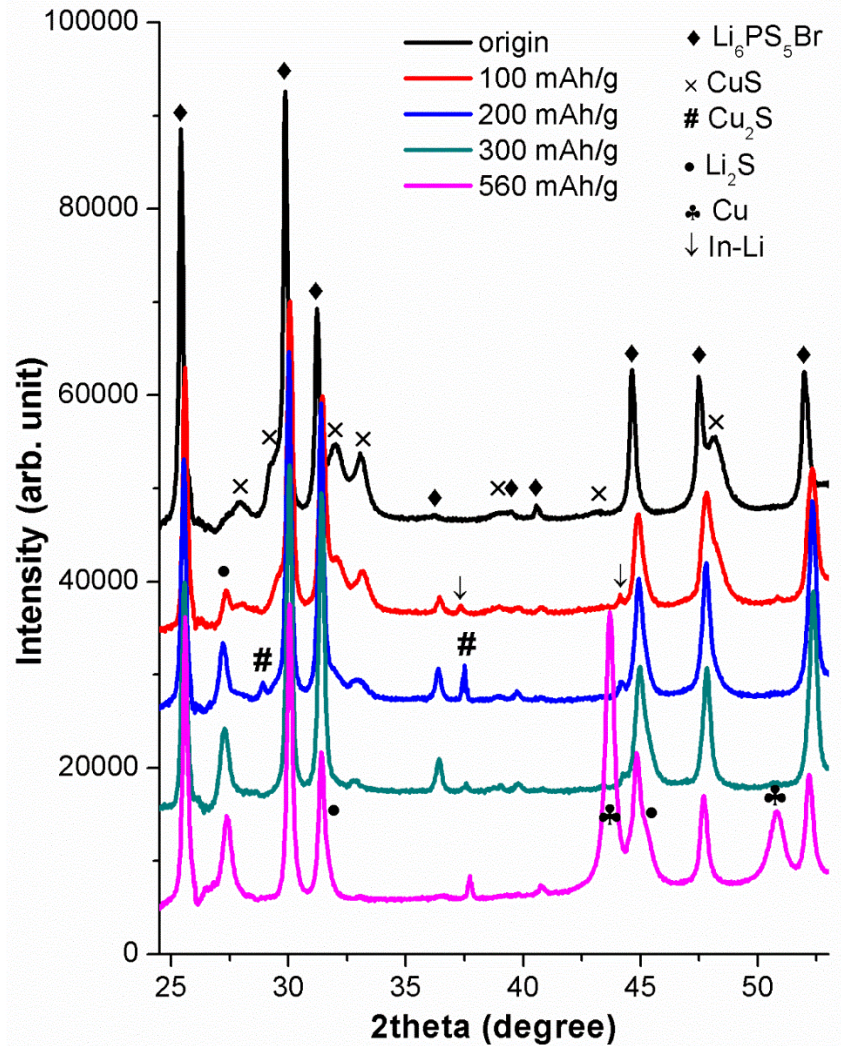


Figure 4-7 XRD patterns of the cathode discharged to different capacity, i.e. 0, 100, 200, 300, 560 mAh/g (top to bottom).

discharge cycle. This intensity variation is seen for all argyrodite peaks, but particularly for those peaks where the intensity is mainly determined by the Li distribution. For example, the (400) peak around $2\theta=36^\circ$ has only low intensity in the initial argyrodite, grows rapidly during discharge (100 and 200 mAh/g) but shrinks again after full discharge. Additionally, the peak shifts indicate a reduced lattice parameter of argyrodite phase during discharge. Both types of changes in the XRD patterns suggest that $\text{Li}_6\text{PS}_5\text{Br}$ actively takes part in the discharge reaction. Considering that $\text{Li}_6\text{PS}_5\text{Br}$ is isostructural to $\text{Cu}_6\text{PS}_5\text{Br}$ ($F4-3m$, with a slightly smaller lattice parameter $a=9.73\text{\AA}^{82,190}$) and the similarity of Cu^+ to Li^+ ions (radii of $\text{Cu}^+=74\text{ pm}$ vs. $\text{Li}^+=73\text{ pm}^{84}$), it appears plausible to propose that Cu^+ formed by the

reduction of Cu^{2+} partially replaces Li^+ in $\text{Li}_6\text{PS}_5\text{Br}$ leading to $\text{Cu}_y\text{Li}_{6-y}\text{PS}_5\text{Br}$. A similar substitution might occur for Li_2S , resulting in $\text{Cu}_z\text{Li}_{2-z}\text{S}$.

For the intermediate stages of the discharge, detailed Rietveld refinements factoring in the possible substitution of Cu^+ for Li^+ in argyrodite and Li_2S resulted in a considerably enhanced quality of the fit. As an example, the Rietveld refinement for the cathode

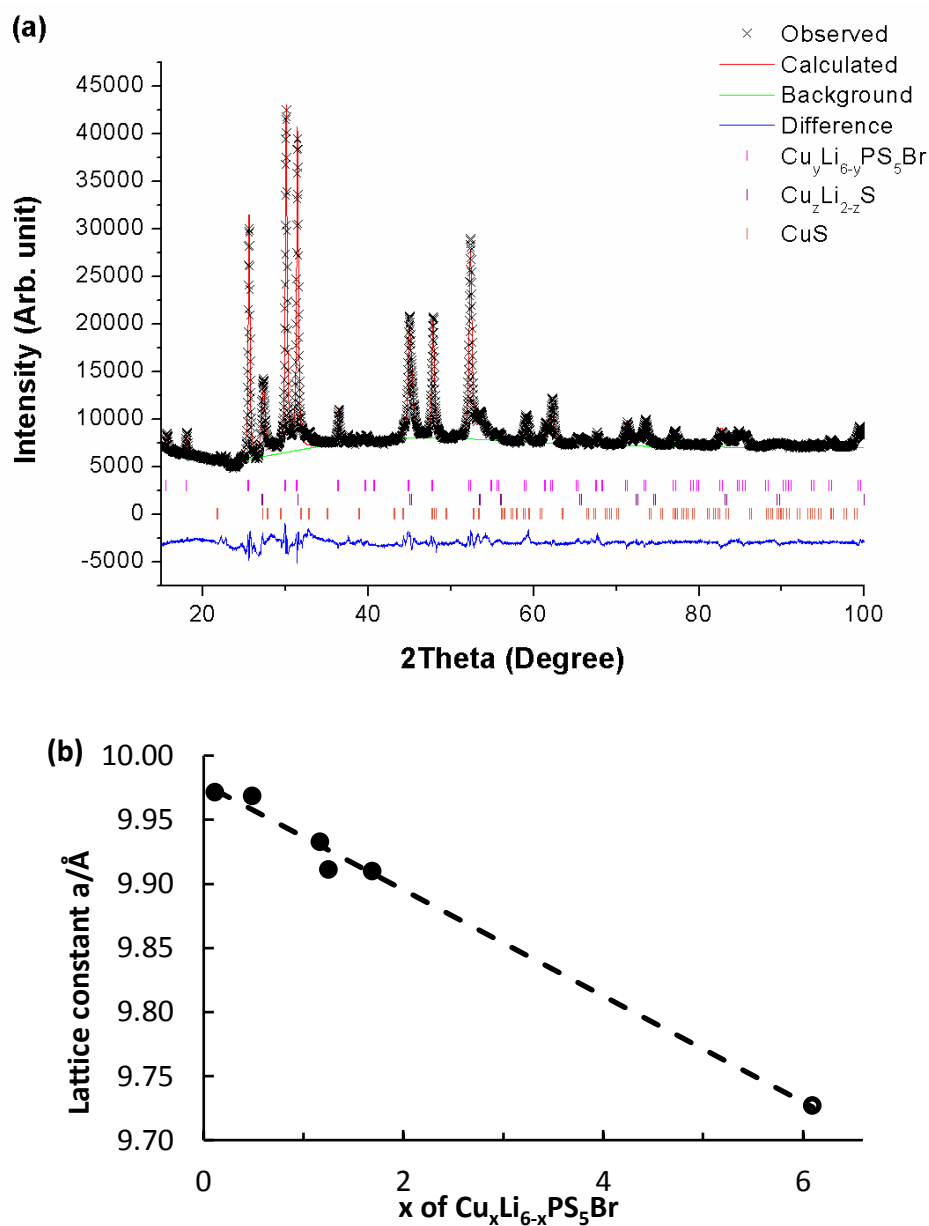
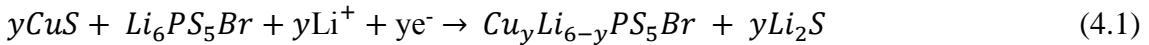


Figure 4-8 (a) Rietveld refinement fitting plots of composite cathode discharged to 300 mAh/g as an example. (b) Correlation between the variation of copper content y of $\text{Cu}_y\text{Li}_{6-y}\text{PS}_5\text{Br}$ and its cubic lattice (filled symbols). Open symbol refers to literature data for $\text{Cu}_6\text{PS}_5\text{Br}$.

discharged to 300 mAh/g is shown in Figure 4-8 (a). A plausible Cu⁺ content up to a maximum value of $y=1.6$ for the argyrodite $Cu_yLi_{6-y}PS_5Br$ is found for this stage of discharge. Figure 4-8 (b) demonstrates the variation of the copper content y with the refined cubic lattice parameter a . The clear correlation between the variations of y (from refined Cu occupancies) and the observed cubic lattice parameter corroborates the proposed formation of $Cu_yLi_{6-y}PS_5Br$.

Figure 4-9 shows the dependence of the $Cu_yLi_{6-y}PS_5Br$, CuS, Cu_2S , $Cu_zLi_{2-z}S$ and Cu weight fractions as well as the copper content y on discharge stage (0, 100, 200, 300 and 560 mAh/g). The refinement of a possible copper content in $Cu_zLi_{2-z}S$ yields a significant Cu content ($z\approx 0.33$) only for 300 mAh/g. The mass fraction of argyrodite significantly increased as the discharge process proceeded and reached a maximum of 74.5% at half discharge and then reduced to its original value at full discharge. This increase of the mass fraction can again be explained by the incorporation of heavy Cu atoms, in line with the independently observed variation of the copper content.

At an early stage of the discharge (100 mAh/g), a considerable amount of Cu⁺ ions has already been incorporated ($y=1.07$). From the weight ratio of $CuS:Cu_yLi_{6-y}PS_5Br:Li_2S=30.8:63.6:5.4$, it can be estimated that 36% of the copper are present as Cu⁺ while the remaining 64% are Cu²⁺, which corresponds to a consistent discharge state of 101 mAh/g. Moreover, the absence of a noticeable peak shift of CuS lets a substantial intercalation appear unlikely.¹²⁹ Thus, it can be concluded that at the early stage of the discharge process, Cu⁺ ions are predominantly located in argyrodite $Cu_yLi_{6-y}PS_5Br$ but not in Li_xCuS or $Cu_zLi_{2-z}S$. The cathode reaction at the early stage should hence follow Equation (4.1):

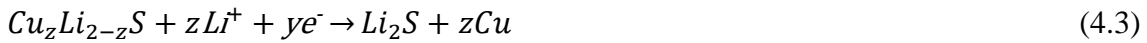
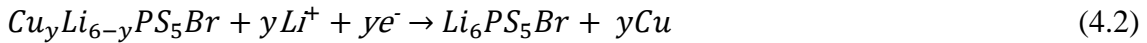


Further discharging to 200 mAh/g led to the appearance of Cu_2S , an increase of the weight fraction of Li_2S and a reduction of the weight fraction of CuS, while the copper content y of the argyrodite phase was almost constant and no metallic copper was observed. Accordingly, it was concluded that Cu_2S and Li_2S were formed directly from the conversion of CuS according to Equation (1.6)¹²⁴. It should be noted that “Cu₂S” here is

meant to represent a series of intermediate copper sulfides. From the refined weight ratio of $\text{CuS}:\text{Cu}_y\text{Li}_{6-y}\text{PS}_5\text{Br}$ ($y=1.07$): $\text{Cu}_2\text{S}:\text{Li}_2\text{S}=16.3:64.7:7.6:11.4$, around 63% of the Cu^{2+} is reduced to Cu^+ , corresponding to a discharge state of 177 mAh/g, slightly below the experimental discharge state (200 mAh/g). The missing Cu^+ might be present in Li_xCuS . A slight increase of the lattice parameters for “CuS” points in the same direction.

When the discharge state reaches 300 mAh/g (approximately half discharge, at the beginning of the 2nd plateau), only a minute amount of CuS is found and still no metallic copper could be detected, suggesting that most of the Cu is present as Cu^+ . At this stage the Cu content of the argyrodite increased to $y=1.59$ (70% of the total amount of Cu). Most of the remaining Cu^+ is now found in $\text{Cu}_z\text{Li}_{2-z}\text{S}$ ($z\approx 0.33$) structurally related to Li_2S , no longer in Li_xCuS or Cu_2S as had been the case for the 200 mAh/g diffractogram at 200 mAh/g.

After full discharge (560 mAh/g), the refined Cu content y in the argyrodite phase significantly reduces from 1.6 (at 300 mAh/g) to 0.4, suggesting that Cu^+ for Li^+ exchange in argyrodite is reversible. At this stage, metallic Cu and Li_2S are the predominant phases besides argyrodite, in line with the literature findings for CuS electrodes in liquid electrolyte batteries. Consequently, the final stage of the discharge reaction can be described by the following equations:



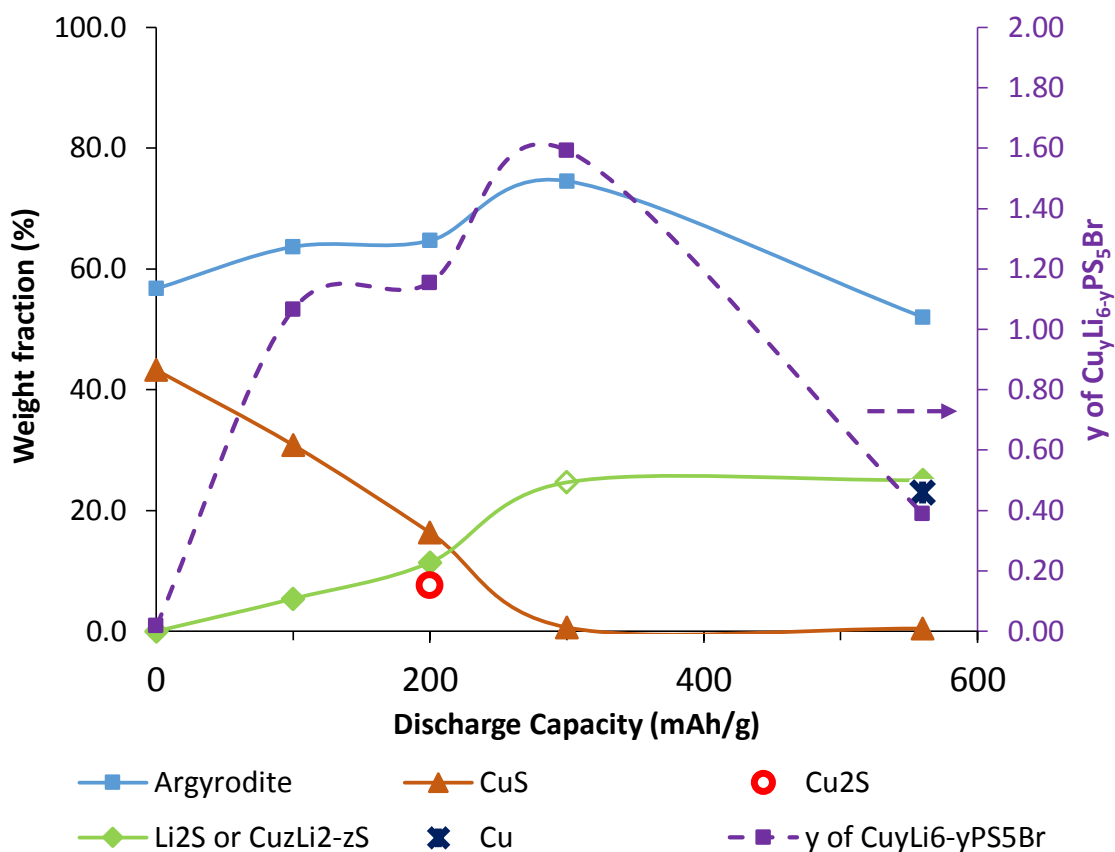


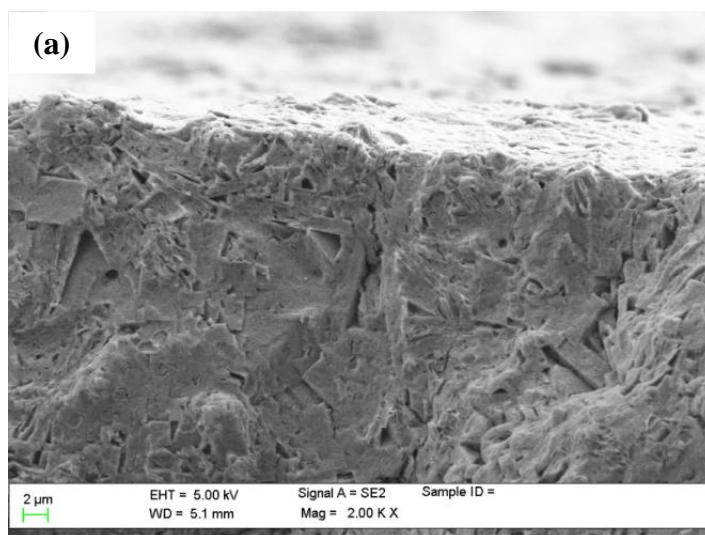
Figure 4-9 Rietveld refinements results showing dependencies of weight fraction of $\text{Cu}_y\text{Li}_{6-y}\text{PS}_5\text{Br}$, CuS , Cu_2S , $\text{Cu}_z\text{Li}_{2-z}\text{S}$ and Cu , and the copper content y of $\text{Cu}_y\text{Li}_{6-y}\text{PS}_5\text{Br}$ on discharge capacity. The closed diamonds represent Li_2S , while the open diamond represents $\text{Cu}_z\text{Li}_{2-z}\text{S}$.

In conclusion, ASSLBs combining CuS cathode with $\text{Li}_6\text{PS}_5\text{Br}$ electrolyte show different electrode reactions from those using liquid electrolyte. The argyrodite-type solid electrolyte $\text{Li}_6\text{PS}_5\text{Br}$ reversibly takes part in the electrode reaction from the beginning of discharge, by substituting Li^+ for Cu^+ , forming $\text{Cu}_y\text{Li}_{6-y}\text{PS}_5\text{Br}$. A maximum value of $y=1.59$ was observed around half discharge, where Cu^{2+} is fully reduced to Cu^+ . Further discharging of the batteries lead to the decrease of y , due to the reduction of Cu^+ to Cu . In addition, a reversible Cu^+ for Li^+ exchange in $\text{Cu}_z\text{Li}_{2-z}\text{S}$ occurs as a function of the state of discharge (reaching a maximum at around 300 mAh/g). Such a reversible cation exchange should be easily possible due to the similar ionic radius ($\text{Cu}^+=74$ pm vs. $\text{Li}^+=73$ pm⁸⁴), the same structure of Li^+ and Cu^+ argyrodites and the high ionic mobility of both Cu^+ and Li^+ .

4.3 Capacity fading analysis

To gain a deeper insight into the reasons for the rapid capacity fading of the CuS/Li₆PS₅Br/In-Li batteries, morphologies of the cross section of the cathode of the batteries before cycling, after the first discharge and after the first charge were studied by SEM. As shown in Figure 4-10 (a), the cathode composite appears dense and crack-free before cycling, suggesting that the pelletization process is effective. However, after the initial discharge, the cathode morphology significantly changed (Figure 4-10 (b)). Besides micrometer-scale argyrodite particles, nanostructured Cu and Li₂S can be discerned after the conversion reaction. The solid-solid interfaces not only give rise to significant pseudocapacitive effects, but together with the first cracks (due to the strong volume expansion associated with the conversion reaction) also limit the power performance of the battery in subsequent cycles. Despite such cracks, at this stage the cathode is still rather dense ensuring reasonable inter-particle contact so that the theoretical discharge capacity was achieved.

After the subsequent charge process, the severe volume shrinkage of the active cathode materials leads to more prominent cracks and pores (Figure 4-10 (c)). The disintegration of the composite cathode obviously causes a drastic capacity fading.



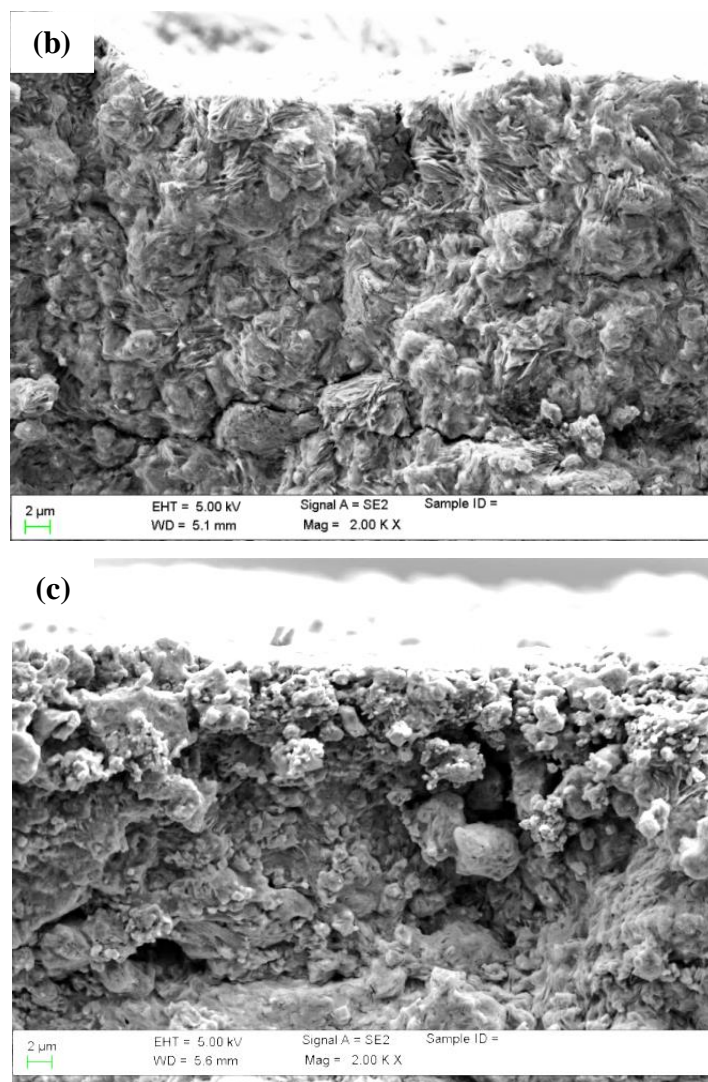


Figure 4-10 SEM images of the cross section of the cathode of the all-solid-state $\text{CuS}/\text{Li}_6\text{PS}_5\text{Br}/\text{In-Li}$ battery (a) before cycling and after (b) 1st discharge and (c) 1st charge between 0.05V and 2.5V.

Rietveld refinement of the composite cathode at the end of the 20th discharge cycle (Figure 4-11) confirms the formation of $\text{Cu}_y\text{Li}_{6-y}\text{PS}_5\text{Br}$ ($F4-3m$) ($y=0.93$), $\text{Cu}_z\text{Li}_{2-z}\text{S}$ ($Fm-3m$) ($z=0.56$) and a minor amount of Cu. The intermediate product $\text{Cu}_z\text{Li}_{2-z}\text{S}$ of the conversion stage corresponds to a volumetric expansion of 34% compared to CuS (or a shrinkage of 22% compared to Cu-Li₂S). The existence of $\text{Cu}_z\text{Li}_{2-z}\text{S}$ at the end of the discharge cycle suggests that the active material is more and more detached from $\text{Li}_6\text{PS}_5\text{Br}$ and carbon, causing high interfacial resistance and incomplete conversion reaction. Only a minute amount of copper (0.2 weight %) is found after 20 cycles. While there may be some undetected X-ray amorphous copper, it appears more likely that this is also a consequence of an incomplete conversion reaction during the later stages of cycling.

In addition, measurement of the internal resistance of the battery during discharge showed an increase of internal resistance up to the middle of the discharge cycle, followed by a reduction on further discharge. Taking into account that a replacement of Li^+ by Cu^+ would reduce the ionic conductivity of $\text{Li}_6\text{PS}_5\text{Br}$ ($\text{Cu}_6\text{PS}_5\text{Br}$ has a room temperature ionic conductivity of ca. 10^{-5} Scm^{-1})^{82,190,191} and that a reduced conductivity is generally observed for the simultaneous presence of two mobile charge carriers (commonly termed “mixed alkali effect” or “mixed mobile ion effect”¹⁹²), the change of internal resistance is consistent with the proposed mechanism. Such an increase of internal resistance will reduce the power performance of such batteries. It may be tentatively assumed that analogous mixed mobile ion solid electrolytes will also influence the performance of other previously studied CuS-based all-solid state batteries.

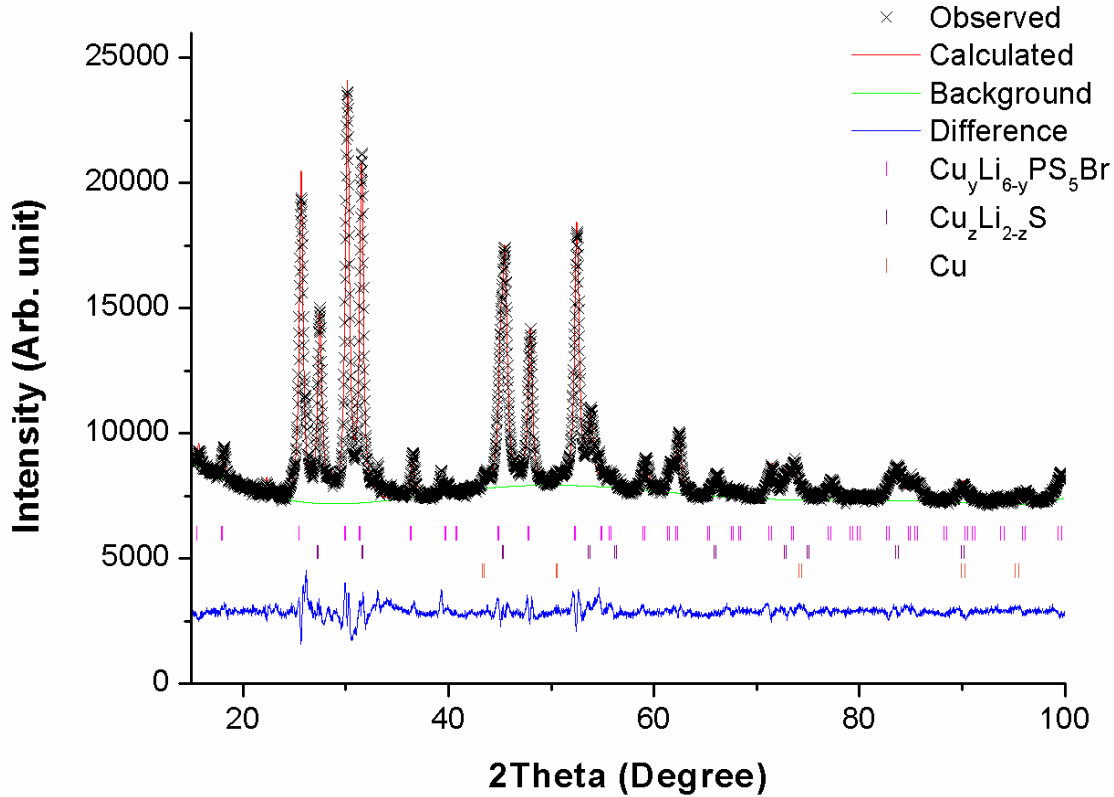


Figure 4-11 Rietveld refinements of the composite cathode after 20 cycles (discharged state) between 0.05V and 2.5V at C/10.

The rapid capacity fading will - as mentioned above - be affected by the severe volume change (ca. 80%) associated to the overall conversion reaction $2 \text{Li} + \text{CuS} \rightarrow \text{Cu} + \text{Li}_2\text{S}$ during discharge, so that the active cathode materials detaches from $\text{Li}_6\text{PS}_5\text{Br}$ (ensuring

ion path) or carbon (ensuring sufficient electronic conductivity). The deteriorating interface condition of Cu-Li₂S or CuS with Li₆PS₅Br and carbon, combined with intrinsically slow kinetics of the conversion reaction, leads to a rapid increase of the overpotential of the battery and thus to an incomplete electrode reaction. The incorporation of Cu⁺ into Li₂S and Li₆PS₅Br giving rise to a mixed mobile ion effect as well as the lack of metallic copper (needed as conductive phase in the discharged state) will further increase the overpotential.

Chapter 5 ALL-SOLID-STATE S/LI₆PS₅BR/IN-LI BATTERIES

As discussed in the previous chapter, CuS or Cu-Li₂S as a high capacity cathode material has the disadvantage that intermediately formed Cu⁺ partially substitutes Li⁺ in lithium argyrodite, deteriorating its conductivity and contributing to a fast capacity fading of ASSLBs using lithium argyrodite solid electrolyte. Therefore, Cu compound that can generate Cu⁺ during cycling should be avoided as a constituent of the cathode materials in battery designs involving argyrodites (or related thiophosphate solid electrolytes). Accordingly, in this chapter, elemental sulfur will be employed as cathode materials instead of CuS. An enhanced cyclic performance of the resulting ASSLBs with a reversible capacity of 1080 after 50 cycles is achieved.¹⁹³

XRD patterns of the pristine sulfur and ball-milled sulfur-carbon composite are shown in Figure 5-1. For the pristine sulfur, all the diffraction peaks can be readily indexed to the orthorhombic phase of α -S. During high-speed ball milling with carbon, sulfur melts and re-solidifies as an amorphous phase, leaving only some broad peaks attributed to the carbon in the XRD pattern of the S/C composite. According to Ji et al.¹⁴⁴ and Nagao et al.¹²² this amorphization of sulfur increases the practical specific capacity of sulfur cathodes in both conventional liquid electrolyte and all-solid-state lithium batteries. This may be tentatively attributed to the intimate contact of S with the carbon and/or the introduction of more defect energy during ball milling. It can also not be excluded that sulfur reacts with functional groups on the surface of super P carbon analogous to the “inverse vulcanization” discussed by Simmonds et al.¹⁹⁴. While Nagao et al. obtained a mixture of amorphous sulfur by ball milling twice¹²² or by high temperature ball milling¹⁵³, we achieved comparable results in one step ball milling at room temperature by choosing a higher ball milling speed of 500 rpm instead of 370 rpm. Consequently, the second ball milling step for the composite cathode after adding the solid electrolyte serves only the purpose of ensuring a homogeneous mixing and thus could be reduced to 30 min (compared to 5h employed by Nagao et al.), which minimizes structural damage to the argyrodite phase resulted from ball milling.

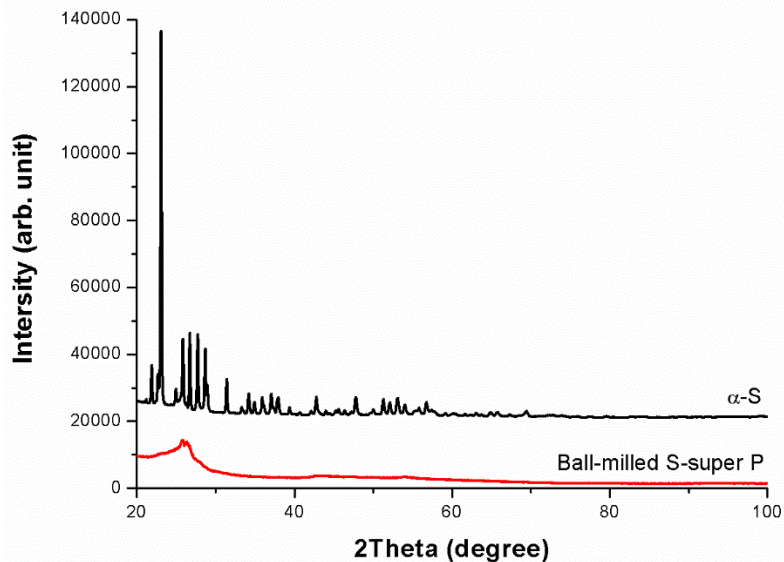


Figure 5-1 XRD patterns of pristine sulfur and ball-milled sulfur-carbon composite.

The microstructures of the pristine sulfur, super P carbon, ball-milled sulfur-carbon composite and composite cathode powder after removing $\text{Li}_6\text{PS}_5\text{Br}$ (by dissolving it in water) were investigated using SEM, as shown in Figure 5-2. The pristine sulfur contained particles larger than $10\ \mu\text{m}$ in size (see Figure 5-2 (a)), while the particle size of the pristine carbon (see Figure 5-2 (b)) was smaller than $100\ \text{nm}$. After the first ball milling, sulfur and carbon were uniformly mixed (denoted as 1st S-C), forming dense μm -sized particles, as shown in Figure 5-2 (c) and (d). Because of the low melting point of sulfur and the high ball milling speed (500 rpm), sulfur melts during high-energy ball milling. The molten sulfur then fills the pores in the carbon phase and surrounds the carbon, forming dense meso-scale particles.

To study the distribution of solid electrolyte within the composite cathode powder (after the second ball milling) by SEM, $\text{Li}_6\text{PS}_5\text{Br}$ was removed by immersing the powder in DI water, leaving only the sulfur-carbon composite (denoted as 2nd S-C residue). Compared to the dense 1st S-C sample, the 2nd S-C residue was highly porous, as shown in Figure 5-2 (e) and (f). As sulfur and carbon are insoluble in water, these pores can be attributed to the dissolved $\text{Li}_6\text{PS}_5\text{Br}$. The pores in the 2nd S-C residue (corresponding to the original $\text{Li}_6\text{PS}_5\text{Br}$ particles) range in size from $50\ \text{nm}$ to $500\ \text{nm}$ and are interconnected, which should ensure effective ion migration pathways within the cathode. This is a key factor for the power performance of ASSLBs, especially in the case of non-ion conducting active

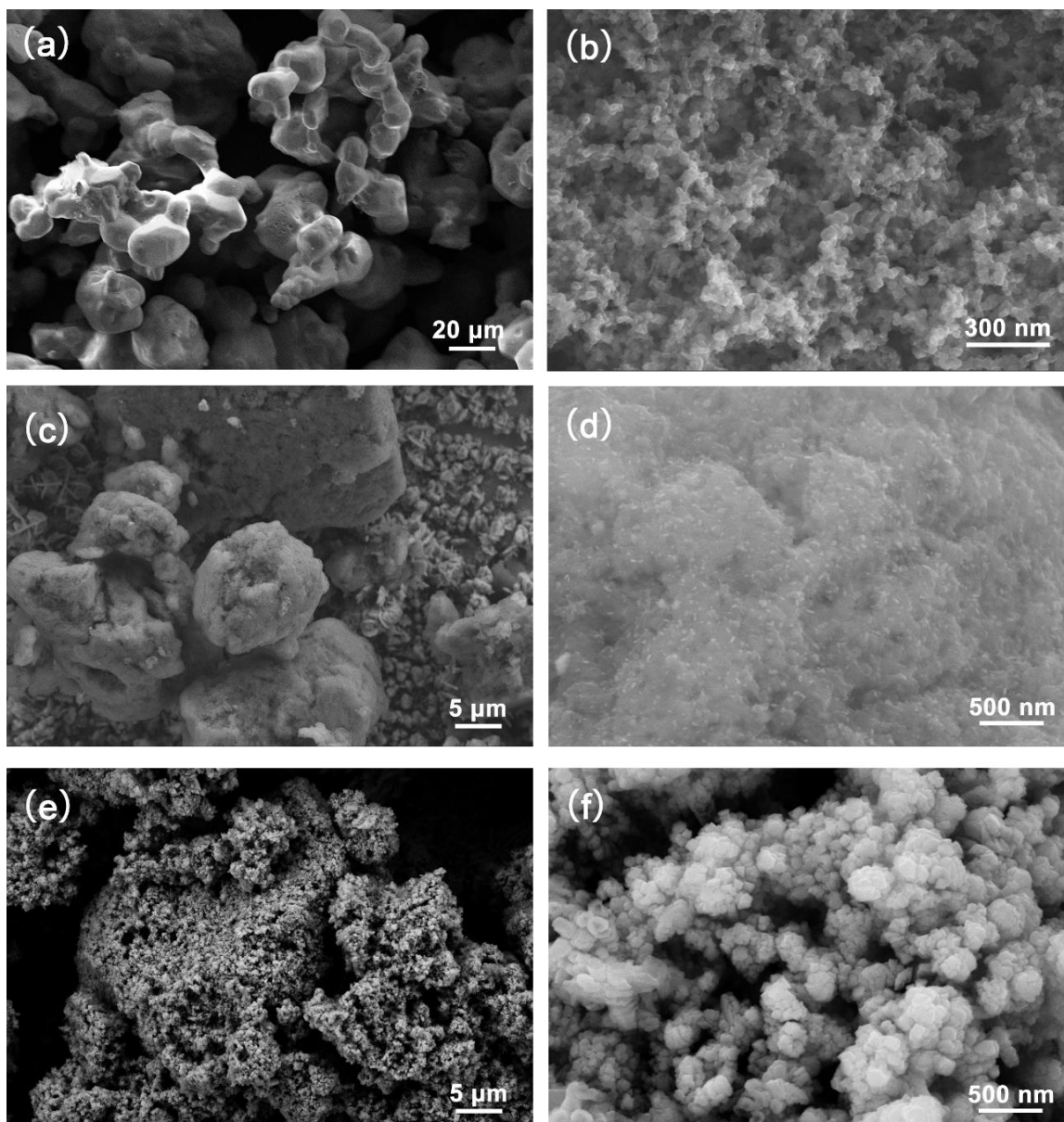


Figure 5-2 SEM images of (a) pristine sulfur, (b) pristine super P carbon, (c, d) ball-milled sulfur-carbon composite and (e, f) sulfur composite cathode powder after removing $\text{Li}_6\text{PS}_5\text{Br}$.

materials such as sulfur. The 2nd S-C residue particles have a typical size smaller than 100 nm, close to that of super P carbon. This drastic reduction in the particle size, compared to that of the 1st S-C, suggests that sulfur at least partially melted again during the second ball milling. Consequently, the large aggregates of the 1st S-C sample were segregated into smaller carbon-based composite particles (<100 nm) by $\text{Li}_6\text{PS}_5\text{Br}$. Such uniform mixing of the composite cathode with nano-scale particles is essential for a full utilization of the active material during cycling, as it maximizes the reactive electrolyte:electrode interface

area and minimizes the thickness of poorly conducting Li_2S_n layers through which Li^+ has to migrate to reach unreacted sulfur.

Figure 5-3 demonstrates the cyclic voltammogram (CV) of S/ $\text{Li}_6\text{PS}_5\text{Br}$ /In-Li cell in the voltage range of 1.0 to 3.0 V vs. Li/Li^+ (0.4 to 2.4 V vs. In-Li). As demonstrated by CV measurements in section 3.4, argyrodite electrolyte $\text{Li}_6\text{PS}_5\text{Br}$ is electrochemically stable between 0 and 4 V vs. Li/Li^+ . Accordingly, all the peaks observed in the voltammogram shown in Figure 5-3 belong to the active cathode material of sulfur. In the first cycle, two cathodic peaks around 2.2 V and 1.8 V vs. Li/Li^+ could be seen, in line with observations in literature for conventional liquid electrolyte batteries.^{147,195} The cathodic peak around 2.2 V corresponds to the reduction of elemental sulfur to higher-order polysulfides (Li_2S_n , $n \geq 4$), while the second cathodic peak around 1.8 V, which is broader with a shoulder at about 1.9 V, is attributed to the further reduction of polysulfides to lower-order polysulfides and finally to Li_2S . For the oxidation process, only one peak around 2.6 V vs. Li/Li^+ could be detected. Oxidation of Li_2S to lower-order polysulfides has slower kinetics compared to the subsequent oxidation to S; this will consequently lead to an overlap of the two reversible reaction steps.¹⁹⁶ During the second and third cycle, however, the cathodic peak around 2.2 V disappeared, leaving only one reduction peak shifted to around 1.7 V.¹⁹⁷ Close matching of the further CV cycles to the 2nd cycle indicates the high reversibility of the sulfur composite cathode and thus high cyclability of the battery.

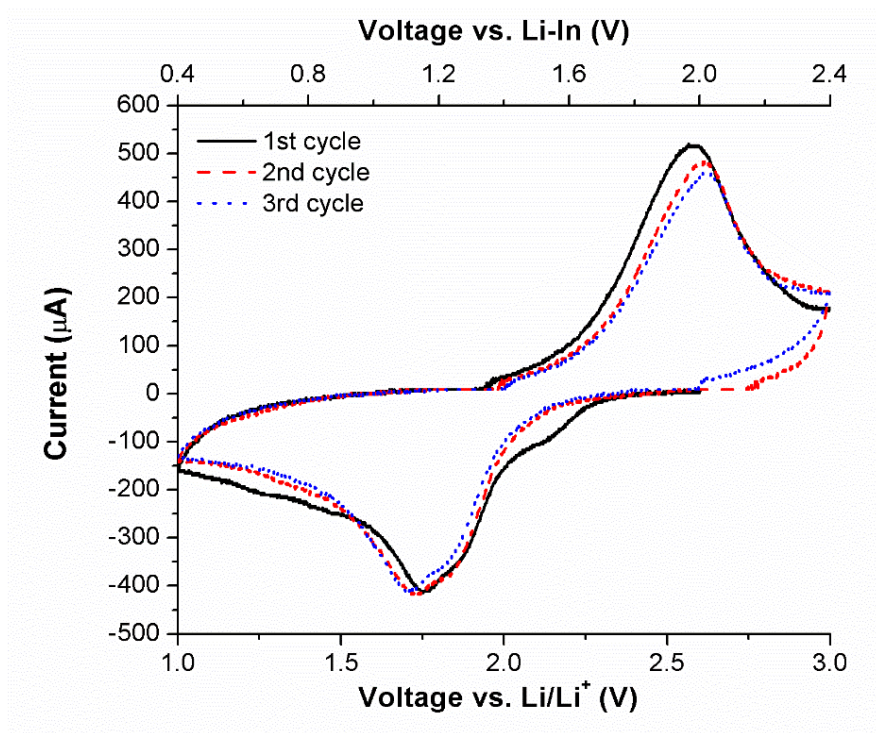
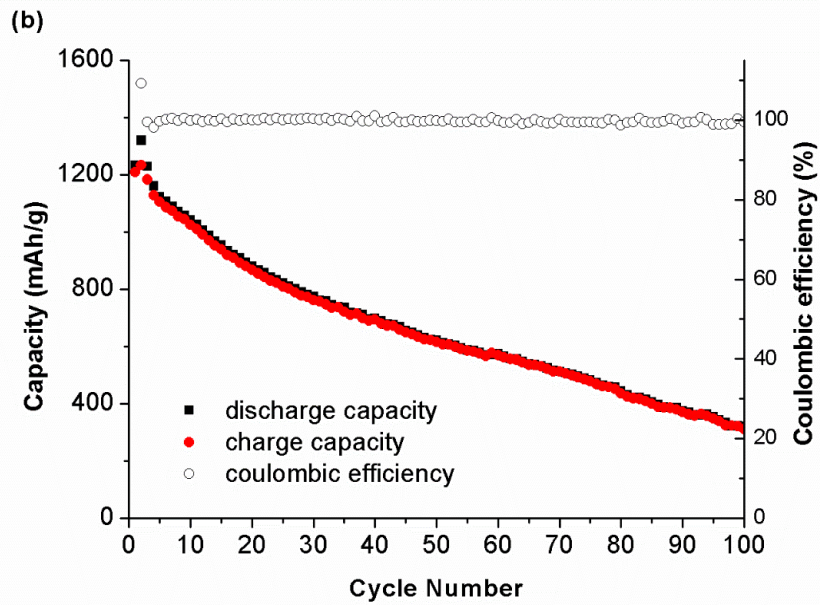
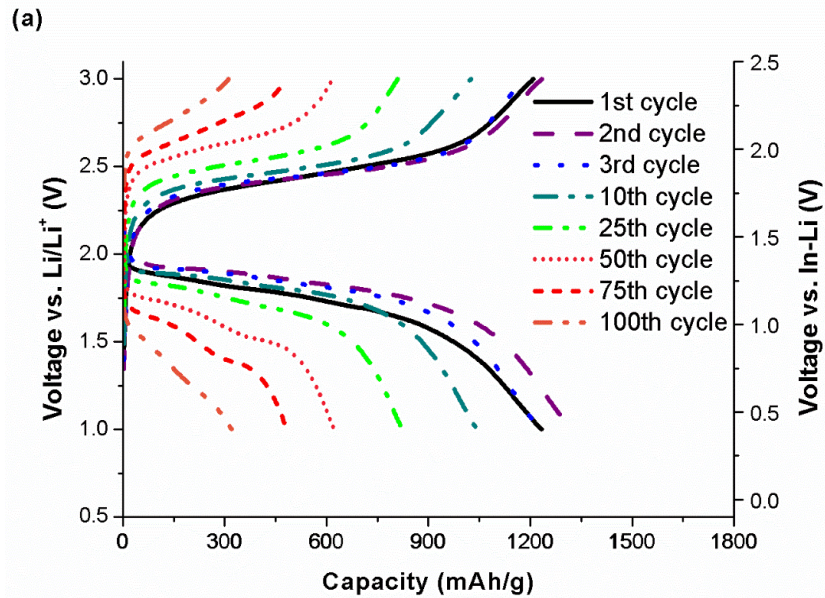


Figure 5-3 Cyclic voltammogram of the all-solid-state cell S/Li₆PS₅Br/In-Li in a voltage range of 1.0 to 3.0 V (vs. Li/Li⁺) at a scanning rate of 0.02 mV/s. Top voltage axis shows the corresponding values of the voltage vs. In-Li.

At first, the room temperature cyclic performance of an all-solid-state S/Li₆PS₅Br/In-Li cell was investigated in ambient atmosphere. The current density was 167 mA/g (0.38 mA/cm², corresponding to C/10) and the voltage range was 1.0 and 3.0 V vs. Li/Li⁺. The weight ratio of S:Li₆PS₅Br:C is 20:70:10. As shown in Figure 5-4 (a), an initial discharge capacity of 1230 mAh/g was achieved. With prolonged cycling, the overpotential, in spite of a decrease at the second cycle, gradually increased and nearly doubled up to the 50th cycle. Figure 5-4 (b) demonstrates the variation of capacity and coulombic efficiency with cycling. Despite the initial increase of 85 mAh/g in the second cycle to 1315 mAh/g, the discharge capacity overall experienced an average fading of 1.4% per cycle, leaving a reversible capacity of 620 mAh/g at the 50th cycle and 320 mAh/g at the 100th cycle. Coulombic efficiency reached an average value of 99.96% over cycles 2 – 50, while averaged over 100 cycles the coulombic efficiency still reached 99.8%.

Discharge depth of the cell during cycling with respect to the discharge/charge capacity is shown in Figure 5-4 (c). The cell exhibited almost the same depth of discharge (~78%) at

fully discharged state for about 60 cycles. On the other hand, the discharge depth after charging kept on increasing with prolonged cycling, clarifying that the capacity loss happened essentially to the discharged active material (i.e. Li_2S or low-order polysulfides). The reason will be further discussed below. At the later stage of cycling (from about cycle 60) the capacity fading became more symmetrical, indicating that the discharge also became less complete now, which may at least partially be ascribed to the growing overpotential.



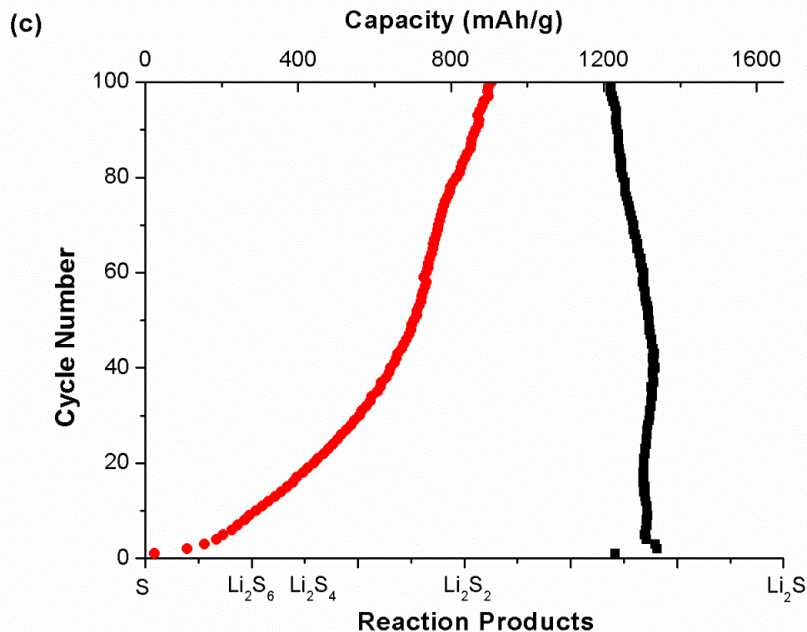


Figure 5-4 Room temperature cyclic performance of the all-solid-state S/Li₆PS₅Br/In-Li cell up to 100 cycles in ambient atmosphere. The current density is 167 mA/g of active sulfur (corresponding to C/10). The voltage range is 1.0 to 3.0 V vs. Li/Li⁺. (a) Discharge-charge curves, (b) discharge/charge capacity and coulombic efficiency and (c) discharge depth of composite cathode during cycling based on discharge/charge capacity shown in (b).

To identify the influence of atmosphere during cycling, room temperature cyclic performance of the all-solid-state Li/S cell was also investigated in the glove box with argon gas atmosphere at the same current density and voltage range. As shown in Figure 5-5 (a), an initial discharge capacity of 1355 mAh/g (i.e. 3.06 mAh/cm²) was achieved. With the prolonged cycling, the overpotential considerably decreased, which could be tentatively ascribed to an improved contact profile of the components within the composite cathode. The discharge-charge curves shifted right (towards lower order lithium polysulfides) on further cycling and stabilized after 40 cycles. Figure 5-5 (b) demonstrates the variation of capacity and coulombic efficiency with cycling. At the second cycle, the discharge capacity drastically decreases to 1150 mAh/g, probably due to the severe volume change of active material during cycling $S + 2Li \leftrightarrow Li_2S$. Over cycles 2 - 50, the discharge capacity experienced an average fading of 0.13% per cycle, representing a favorably high capacity retention of 94% for 49 cycles, leaving a reversible capacity of 1080 mAh/g at the 50th cycle. Coulombic efficiency reached an average value close to 100% over cycles 2 - 50, suggesting that there are hardly any side reactions during cycling. It may worth noting

that the capacity of the battery still undergoes some fading presumably because of the gradual loss of active material due to the cathode volume changes, but periodically the capacity increases again when further volume changes reestablish electrical contact to the temporarily detached cathode material.

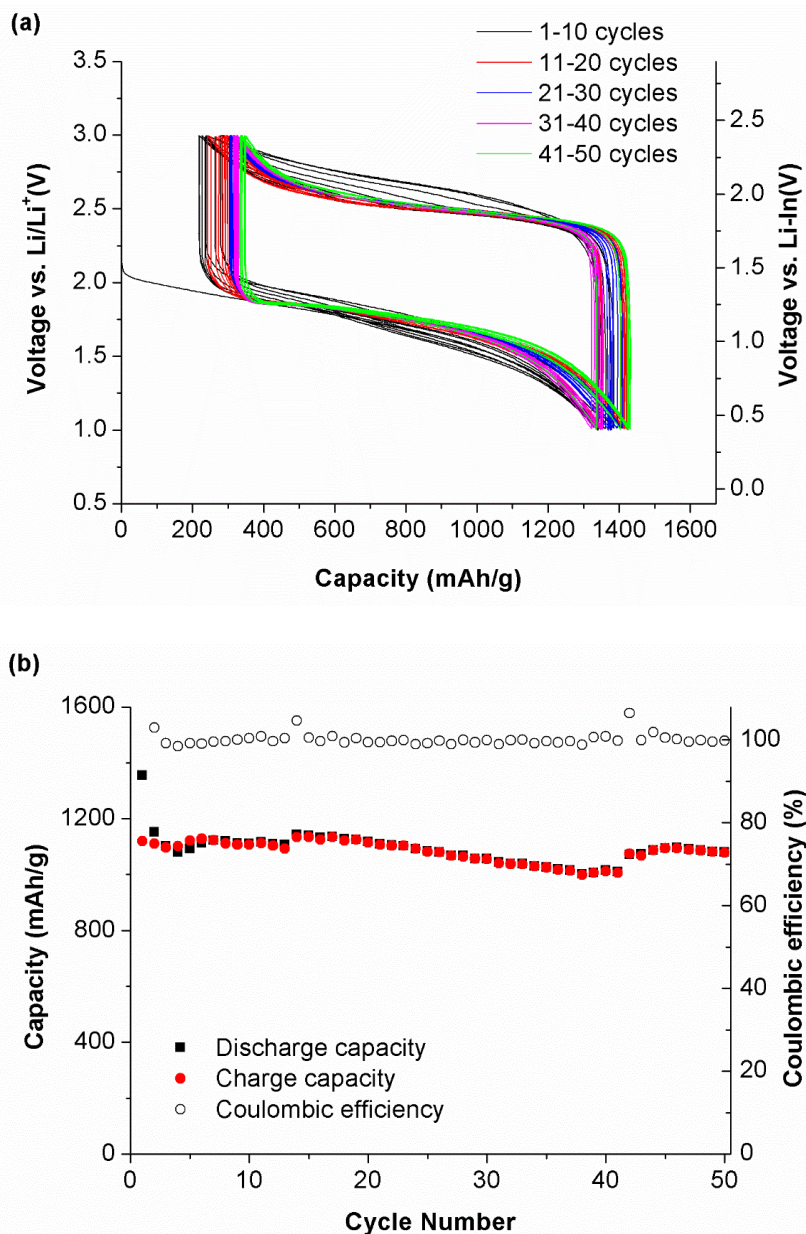


Figure 5-5 (a) Discharge-charge curves, (b) discharge/charge capacity and coulombic efficiency of the all-solid-state S/Li₆PS₅Br/In-Li cell up to 50 cycles at room temperature. The current density was 167 mA/g of active sulfur (corresponding to C/10). The voltage range was 1.0 to 3.0 V vs. Li/Li⁺. The measurement was carried out in argon atmosphere.

Recalling that the cell tested in air (though nominally in a closed Swagelok cell) as shown in Figure 5-4 exhibited a constantly increasing overpotential during cycling and a much faster capacity fading (around 50% over 50 cycles), cycling a cell in glove box can greatly enhance the cyclic performance, suggesting an imperfect sealing of the Swagelok cell. This difference remained when the testing in air was repeated for a variety of other Swagelok cells including newly purchased ones or the sealing is improved by Parafilm or Kapton-tape wrapping, indicating that a perfect sealing is indispensable for a long cycle life of these Li/S batteries.

The oxygen and especially moisture in the air can react with most of the components of the battery, such as lithium argyrodite $\text{Li}_6\text{PS}_5\text{Br}$, Li anode, discharge product Li_2S and the lithium polysulfides. These reactions of the active electrode materials and the electrolyte materials will produce insulating interfaces, thus increasing the overpotential of the cell. The loss of the active electrode materials will also cause the insistent capacity fading. In addition, elemental sulfur is stable in both O_2 and H_2O , while the discharge products like Li_2S and polysulfides are more likely to be consumed by oxidation or hydrolysis in contact with humid air. Therefore, the capacity fading should mostly occur at the end of discharge and at the beginning of charge, which is in line with the finding from Figure 5-4 (c). It is noted that since the initial discharge capacity of the battery cycling in the air is similar to that cycling in the glove box and its capacity retention is moderately high, the leakage of such Swagelok cells will only become discernible during long cycling (but too high to be ignored in such stability tests).

Ex-situ XRD was conducted on the composite cathode before and after cycling, as shown in Figure 5-6. Due to the amorphization of sulfur after the first ball milling, no peaks corresponding to sulfur could be observed for the composite cathode before cycling. Except for one broad peak around 53° attributed to carbon, all the peaks can be assigned to $\text{Li}_6\text{PS}_5\text{Br}$. After cycling, no obvious change occurred to the peak positions or intensities observed in the XRD pattern, suggesting that the argyrodite structure was stable throughout cycling. As discussed in Chapter 4, all-solid-state batteries using CuS or Cu- Li_2S as cathode materials and $\text{Li}_6\text{PS}_5\text{Br}$ as solid electrolyte revealed that Cu^+ can be reversibly exchanged for Li^+ in $\text{Li}_6\text{PS}_5\text{Br}$, leading to mixed mobile ion product $\text{Cu}_x\text{Li}_{6-x}\text{PS}_5\text{Br}$. Such

complications cannot occur in Li/S batteries, so that the favorably high cycling stability of the argyrodite solid electrolyte corroborates its application potential in all-solid-state Li/S secondary batteries.

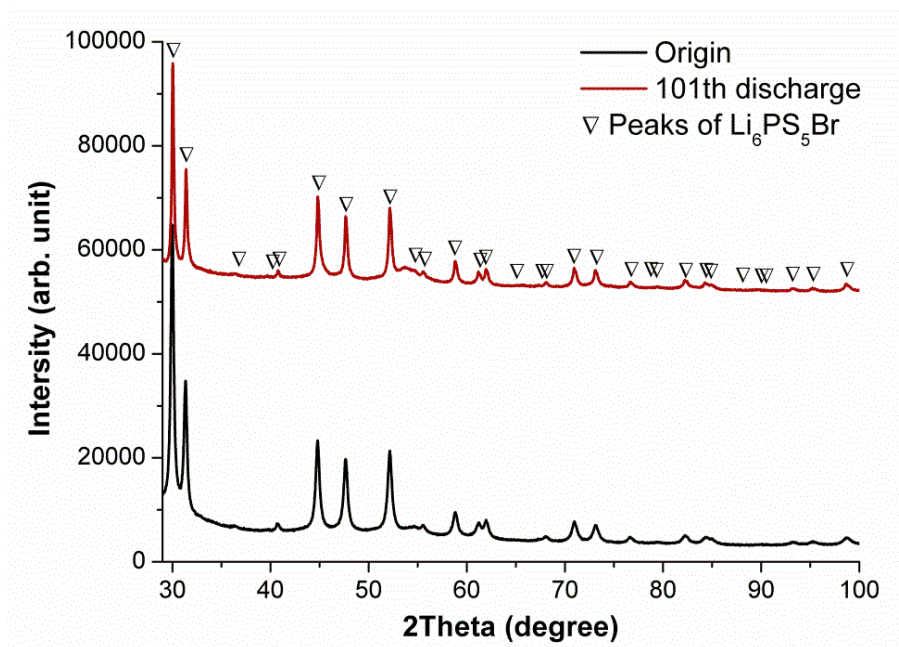


Figure 5-6 Ex-situ XRD patterns of composite cathode before cycling and after 101st cycle (discharged state).

Cyclic performance of all-solid-state Li/S cells using composite cathode with different S content (20 wt%, 25 wt%, 30 wt% and 40 wt%) were examined. Due to equipment limitations these tests had to be done in Swagelok cells outside the glove box. Therefore the number of cycles studied was limited, so that the slow influence of minor leakage should not significantly affect the outcome of this study. Figure 5-7 shows the variation of selective discharge capacities with S content of composite cathode (at the 1st, 10th, 15th and 20th cycles). At the beginning of cycling, a high value of discharge capacity (>1160 mAh/g with respect to the weight of S) was obtained for all the cells, suggesting that most of the sulfur took part into the electrode reaction regardless of the variation of sulfur content. When the S content is 25 wt%, the initial discharge capacity of the cell was 1460 mAh/g of S, which was the highest among all the cells investigated in this study. In Figure 5-7 the capacities are shown with respect to the weight of the cathode composite. In this way, the influence of the choice of S content on the energy density of the cell can be read more directly. Only in the first cycle the capacity of the cathode composite rises with the sulfur

content. After 10 cycles the discharge capacity at S= 25 wt% became the highest since the cells with S contents of 20 and 25 wt% initially showed similarly slow capacity fading. The capacity of cells with larger S contents faded considerably faster, which could be ascribed to the more severe volume change of the composite cathode due to the higher active materials content. Therefore, in terms of the capacity retention our cells at 20 wt% and 25 wt% S content are obviously superior to those with S contents ≥ 30 wt%. The optimized weight ratio of sulfur in the composite cathode of our cell is therefrom 25 wt%.

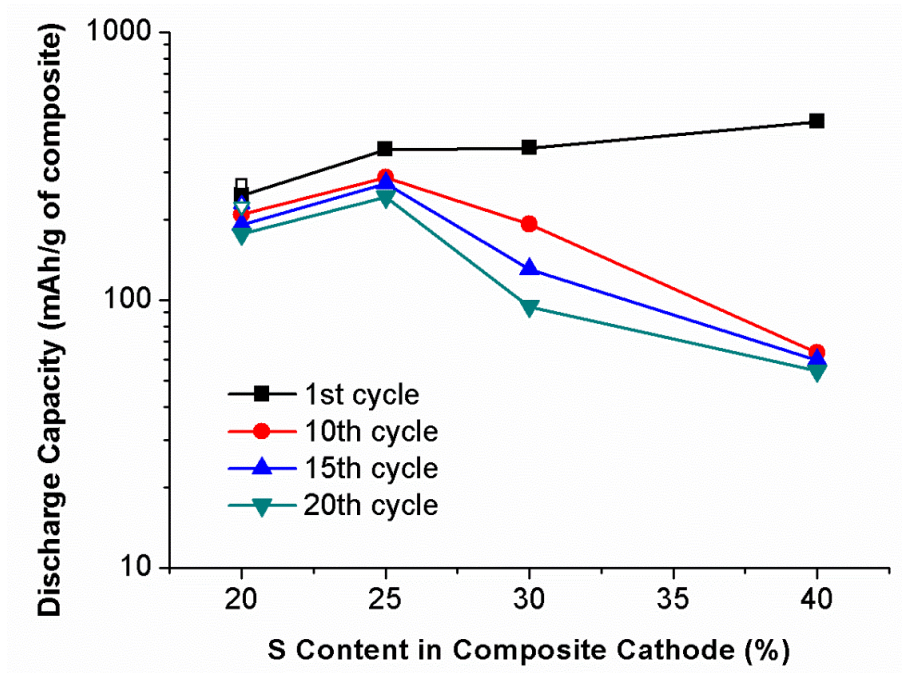


Figure 5-7 Discharge capacity of the all-solid-state cells using composite cathode mixture with various S contents, i.e. 20 wt%, 25 wt%, 30 wt% and 40 wt%. Here the discharge capacity is given with respect to the total weight of the composite cathode as a more direct measure for the energy density of cells based on these composites. Discharge capacity curves are shown only for the 1st, 10th, 15th and 20th cycle for clarity. The open symbols are data for the cell testing in the glove box (20 wt%).

Chapter 6 ALL-SOLID-STATE $\text{MoS}_2/\text{Li}_6\text{PS}_5\text{Br}/\text{In-Li}$ BATTERIES

In the previous chapter, high energy density all-solid-state S/ $\text{Li}_6\text{PS}_5\text{Br}/\text{In-Li}$ batteries have been demonstrated. Without the existence of Cu^+ playing a decisively negative role in the ASSLBs, the all-solid-state Li/S batteries exhibited a reversible capacity of 1080 mAh/g after 50 cycles. Typically, to mitigate the extremely low electronic conductivity of S and Li_2S , a large amount of carbonaceous electronic conductors are added. On the other hand, it has been reported recently that conventional liquid electrolyte batteries using MoS_2 will effectively become a Li/S battery with metallic Mo particles as electronically conducting materials after fully discharge. Therefore, in this chapter we studied MoS_2 as the cathode materials for ASSLBs with lithium argyrodite $\text{Li}_6\text{PS}_5\text{Br}$ as the solid electrolyte. It was confirmed by CV and TEM that the electrode reaction of $\text{MoS}_2 + 2\text{Li} \rightarrow \text{Mo} + \text{Li}_2\text{S}$ is irreversible after the first full discharge in ASSLBs as well, leading to the formation of a novel type of all-solid-state Li/S batteries with spherical Mo nanoparticles of around 7 nm in size finely dispersed in the composite cathode. The resulting batteries showed a reversible capacity of 190 mAh/g after 40 cycles at room temperature, and of 270 mAh/g even after 700 cycles at 70 °C, representing a capacity retention of 85%.¹⁹⁸

SEM images of the pristine MoS_2 powder (Sigma-Aldrich, 99%) and the MoS_2 composite cathode powder after ball milling are shown in Figure 6-1. In the layered crystal structure of MoS_2 , Mo atoms are covalently bonded to S atoms in two adjacent S layers; the electroneutral MoS_2 slabs are held together by van der Waals interactions. Due to the weak interaction between the S-Mo-S layers, the slabs can be easily separated from each other, leading to a pronounced plate-like morphology. As demonstrated in Figure 6-1 (a), the diameter of the particles is within the range of 1-5 μm , while the thickness is much smaller (around 100 nm). After ball milling the MoS_2 powder with $\text{Li}_6\text{PS}_5\text{Br}$ powder and carbon for 30 min at 500 rpm to prepare the composite cathode powder, no distinct variation of MoS_2 particles in either diameter or thickness can be discerned (see Figure 6-1 (b)), suggesting that to some extent MoS_2 can sustain high-energy mechanical milling without severe morphology change. So this ball milling should be seen more as an effective way to achieve a uniform mixing of the composite cathode powder: The MoS_2 plates are

surrounded by solid electrolyte $\text{Li}_6\text{PS}_5\text{Br}$ particles and carbon black particles, thus ensuring both efficient ionic and electronic conduction paths within the cathode.

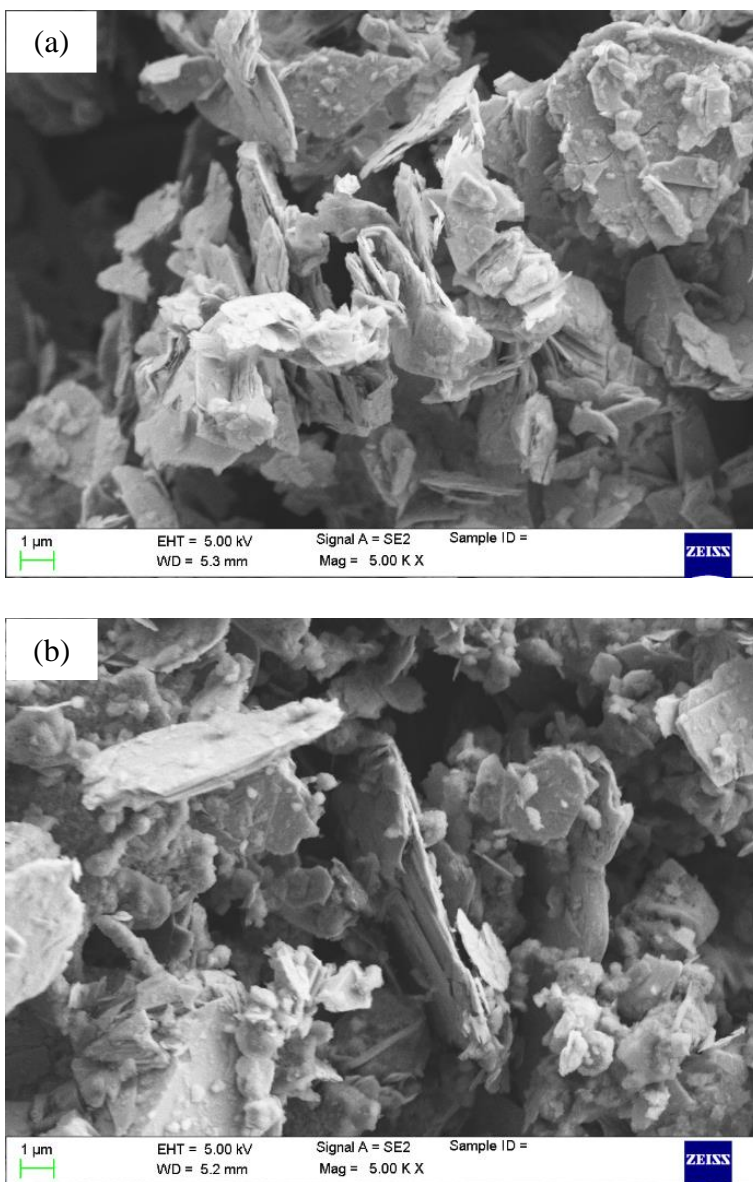


Figure 6-1 SEM images of the pristine MoS_2 powder and the MoS_2 composite cathode powder after ball milling.

Cyclic voltammetry (CV) was performed on the all-solid-state $\text{MoS}_2/\text{Li}_6\text{PS}_5\text{Br}/\text{In-Li}$ cell between 0.1-3.1 V vs. Li/Li^+ , as shown in the Figure 6-2. The first reduction cycle showed two distinct cathodic peaks around 1.0 and 0.4 V. These peaks can be respectively attributed to the intercalation reaction $\text{MoS}_2 + x\text{Li} \rightarrow \text{Li}_x\text{MoS}_2$ (equation (1.10)), and the conversion reaction $\text{Li}_x\text{MoS}_2 + (4-x)\text{Li} \rightarrow \text{Mo} + 2\text{Li}_2\text{S}$ (equation (1.11)) together with the

interfacial lithium storage, in line with the reported literature data in liquid electrolyte batteries (see section 1.4.5). Moreover, a minute peak at ca. 2.2 V occurred due to a minor impurity in the commercial MoS₂ (<< 1% of a Chevrel phase, as suggested from the XRD pattern), while a search for impurities by XPS only revealed tiny amounts of Mo⁶⁺ from surface oxidation and Mo²⁺ which may tentatively be ascribed to the Chevrel phase impurity. In the subsequent reduction cycles, significant changes in the CV curves could be discerned. The peak at 1.0 V disappeared, while two new peaks around 1.8 V and 1.1 V occurred, supporting the new electrode reaction $S + 2Li \rightarrow Li_2S$. The peak at ca. 0.25 V corresponding to the interfacial lithium storage still existed though with a gradual reduction in intensity, which may be tentatively ascribed to reduction of the electroactive interface area, e.g. by coarsening or agglomeration of the Mo particles.

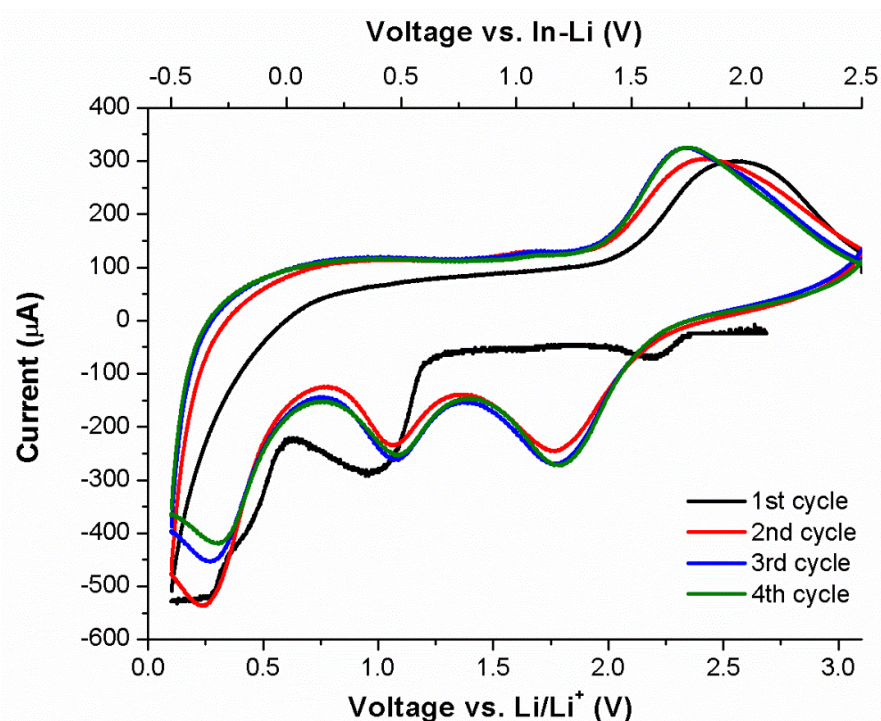


Figure 6-2 Cyclic voltammogram of all-solid-state MoS₂/Li₆PS₅Br/In-Li cell at a scanning rate of 0.05 mV/s. The voltage range is 0.1-3.1 V vs. Li/Li⁺.

The formation of all-solid-state Li/S batteries with Mo nanoparticles dispersed in the fully discharged composite cathode was verified by HRTEM. The all-solid-state batteries charged to 3.1 V after full discharge to 0.1 V was disassembled and the composite cathode was immersed in DI water. Since the lithium compounds in the composite cathode can

react with and then dissolve in water, the $\text{Li}_6\text{PS}_5\text{Br}$ solid electrolyte (and maybe Li_2S if it exists) was then removed, leaving only those insoluble to water, such as sulfur, minor carbon and $\text{MoS}_2/\text{Li}_x\text{MoS}_2$ (if it forms again). Note that Li_xMoS_2 in contact with water will lead to MoS_2 and soluble LiOH and thus it should be visible in the TEM as well.¹⁹⁹ TEM results of the resulting powder are demonstrated in Figure 6-3. Analysis of the selected area electron diffraction (SAED) pattern (bottom left of Figure 6-3) indicated that metallic Mo particles exist in the composite cathode powder, albeit without any sign of MoS_2 . The HRTEM image (right of Figure 6-3) shows that the size of the Mo particles in the composite cathode is around 7 nm, similar to the 3-6 nm reported for discharged MoS_2 cathode in a liquid electrolyte half-cell¹⁵⁷. These TEM results of cathode materials in the charged state support that $\text{MoS}_2/\text{Li}_x\text{MoS}_2$ will not reform in the following charge cycles once the ASSLB is fully discharged. In other words, the all-solid-state $\text{MoS}_2/\text{Li}_6\text{PS}_5\text{Br}/\text{In-Li}$ battery essentially becomes a Li/S battery with Mo nanoparticles dispersed in the cathode.

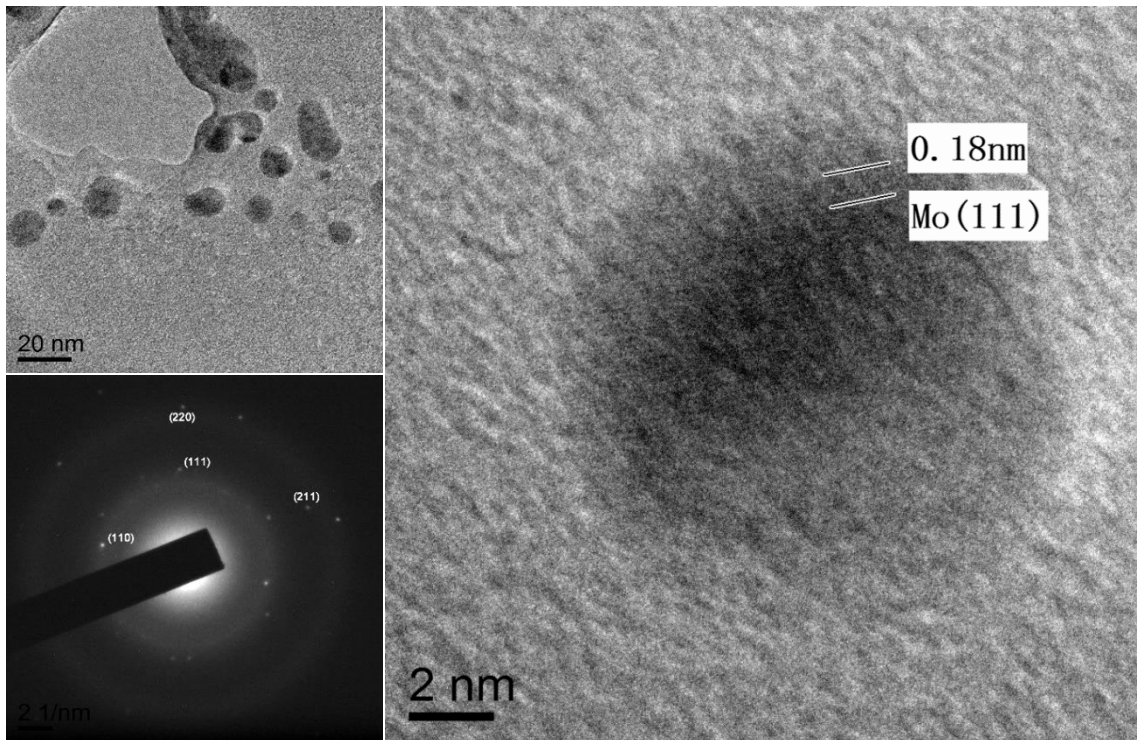


Figure 6-3 TEM results of the charged MoS_2 composite cathode powder after dissolving in DI water. Bottom left: SAED pattern of sample shown in the figure at the top left side. Right: HRTEM image.

Room temperature cyclic performance of the all-solid-state $\text{MoS}_2/\text{Li}_6\text{PS}_5\text{Br}/\text{In-Li}$ cell was investigated at C/10 rate (corresponding to a current density of 67 mA/g) (see Figure 6-4). The voltage range of the first 5 cycles is 0.1-3 V vs. Li/Li^+ so as to “activate” the Li/S cell, while that of the following cycles is within a more practical scale of 1-3 V vs. Li/Li^+ . An initial discharge capacity of 650 mAh/g was obtained, close to that of the theoretical capacity of 670 mAh/g. Various MoS_2 -based cells using liquid electrolyte have been reported in recent years with an initial discharge capacity exceeding the theoretical capacity^{171,173}. This excess capacity can be ascribed to the high contribution of interfacial charge storage at the $\text{Li}_2\text{S}/\text{Mo}$ interfaces, lithium intercalation in the conductive carbon and the SEI formation²⁰⁰. In most of their cases, a large amount of carbonaceous materials was employed in the MoS_2 electrode (e.g. $\text{MoS}_2:\text{C}\approx 3:1$ ¹⁷¹ or even 1:1¹⁷³) and the resulting liquid electrolyte batteries were typically discharged to a relatively low voltage (e.g. 0 V). Consequently, the carbonaceous materials contributed to a significant amount of the practical capacity. Nevertheless, in our case, the carbon content is drastically reduced to a weight ratio of $\text{MoS}_2:\text{C}=10:1$, leading to the practical capacity with a value close to but not exceeding the theoretical capacity. During the first charge, however, a significant capacity drop by 210 mAh/g was observed, which can be tentatively attributed to the severe volume expansion of the overall electrode reaction $\text{MoS}_2 + 4\text{Li} \rightarrow \text{Mo} + 2\text{Li}_2\text{S}$. Thereafter, the capacity fading of the cell became moderate, leading to a reversible capacity of 385 mAh/g after 5 cycles within the full voltage range of 0.1 - 3.0 V. These 5 cycles should be seen more as a pre-treatment of the battery ensuring the complete conversion of MoS_2 into Mo and S/ Li_2S .

From the 6th cycle onwards, the cell was then cycled over a practically useful voltage range of 1.0 – 3.0 V. Consequently, the capacity at the 6th cycle is considerably lower, since the lithium storage in the interfaces of $\text{Li}_2\text{S}/\text{Mo}$ and in the carbon both occurs below 1 V vs. Li/Li^+ .¹⁶⁷ With prolonged cycling, the capacity of the cell gradually recovered, probably due to the simultaneously improved electrical contact within the composite cathode. A reversible capacity of 190 mAh/g was achieved after 40 cycles. In addition, the cell showed a high coulombic efficiency after stabilization (19th cycle onwards), suggesting that there is hardly any side reaction during cycling.

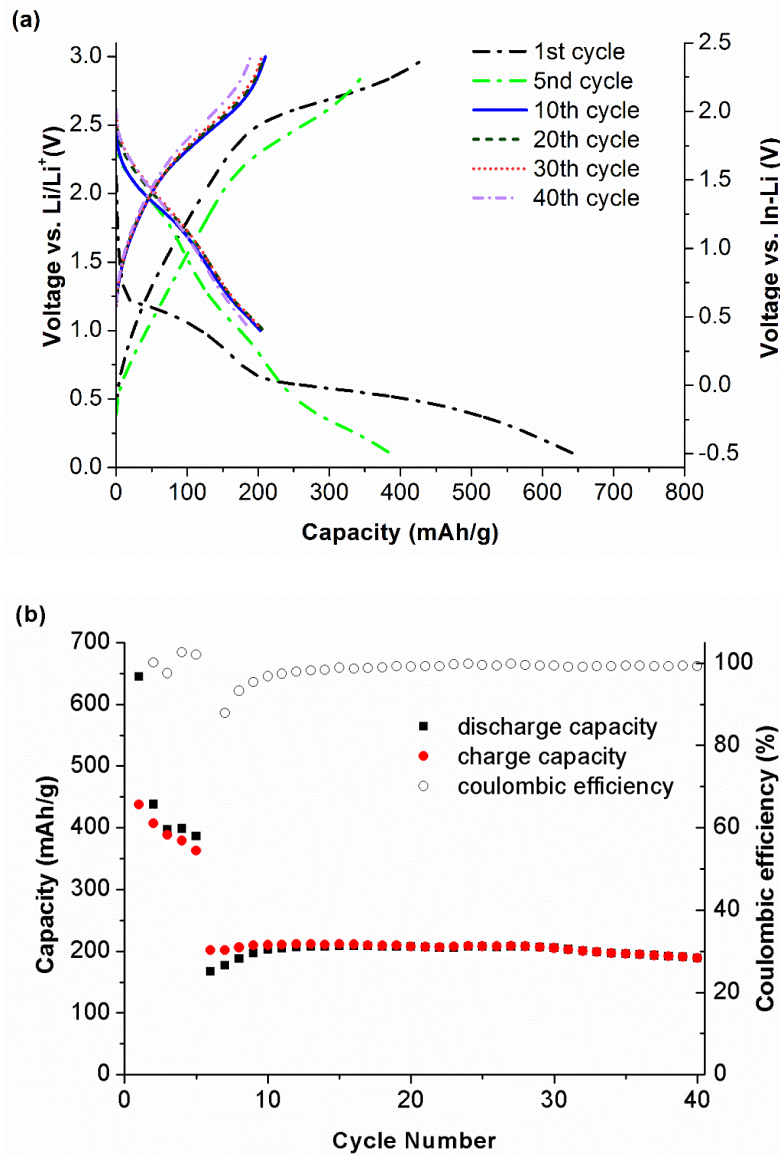


Figure 6-4 (a) Discharge-charge curves and (b) cyclic behavior of the all-solid-state $\text{MoS}_2/\text{Li}_6\text{PS}_5\text{Br}/\text{In-Li}$ cell at room temperature at a rate of $C/10$. The voltage range was 0.1-3 V (vs. Li/Li^+) in the first 5 cycles and 1-3 V in the following cycles.

High temperature cyclic performance of the all-solid-state $\text{MoS}_2/\text{Li}_6\text{PS}_5\text{Br}/\text{In-Li}$ cell was studied at various C rates, i.e. $C/5$, $C/2$ and $1C$, at a temperature of $70\text{ }^\circ\text{C}$. It should be noted that such rates are relatively high for ASSLBs, especially those using high capacity conversion electrodes. The voltage range was 0.1-3.1 V (vs. Li/Li^+) in the first cycle and 0.6-3.1 V in all following cycles. The discharge/charge rate was changed every 200 cycles. Similar to the cell cycling at room temperature, despite a capacity drop at the second cycle where the voltage range was narrowed, the cell gradually recovered in the following cycles

and achieved a reversible capacity around 315 mAh/g for 200 cycles at C/5. Increasing the C rate leads to the reduction of discharge capacity, i.e. 210 mAh/g at C/2 and 95 mAh/g at 1C. When the C rate was changed back to C/5, a reversible capacity of 270 mAh/g was still maintained, indicating a capacity retention of ca. 85% after 700 cycles. With such a high capacity retention, Li/S-batteries using MoS₂ as the starting composite cathode material may be commercially viable products.

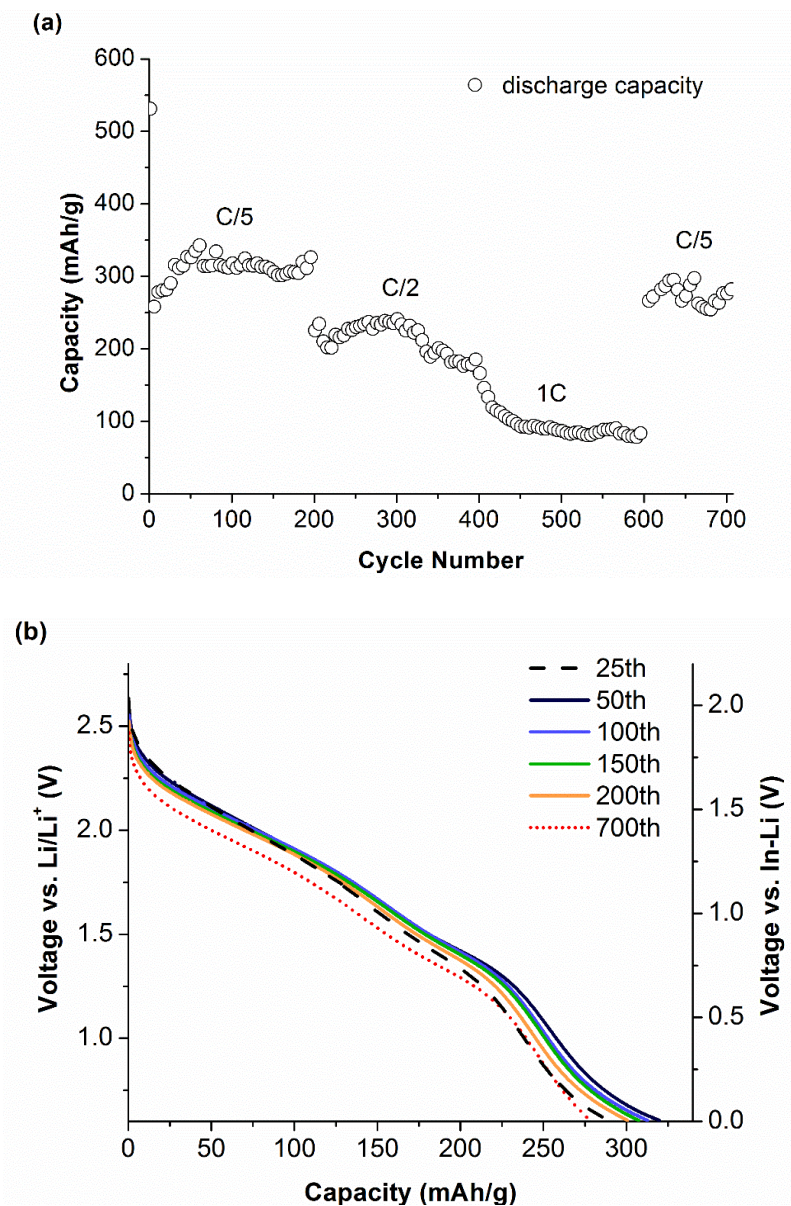


Figure 6-5 (a) Cycling behavior and (b) discharge curves of all-solid-state MoS₂/Li₆PS₅Br/In-Li cell at 70 °C. The voltage range was 0.1-3.1 V vs. (Li/Li⁺) at the first cycle and 0.6-3.1 V in the following cycles. The discharge/charge rate changed every 200 cycles from C/5, C/2 to 1C and then back to C/5.

Chapter 7 CONCLUSIONS AND OUTLOOK

In this study, fast Li^+ conductors lithium argyrodites $\text{Li}_6\text{PS}_5\text{X}$ ($\text{X}=\text{Cl}, \text{Br}$) were explored and all-solid-state lithium batteries (ASSLBs) were prepared combining argyrodites solid electrolyte with various sulfide materials, including CuS , S and MoS_2 . The key findings are briefly summarized as follows:

1. The structure, ionic conductivities, electrochemical stability and morphologies of lithium argyrodites $\text{Li}_6\text{PS}_5\text{X}$ ($\text{X}=\text{Cl}, \text{Br}$) were explored (Chapter 3). Phase formation of argyrodites was monitored in situ starting from partially amorphous ball-milled samples, revealing that argyrodite phase starts to form at low temperature, while the lattice parameters, halide content and halide distribution of argyrodites vary with annealing temperature. Impedance measured up to various temperatures shows a distinct dependency of both room temperature ionic conductivity and activation energy on the annealing temperature. Such dependence could be ascribed to the variation of structure and thus ordering in lithium argyrodites with the annealing temperature. A maximum room temperature ionic conductivity of 1.1×10^{-3} S/cm is obtained for $\text{Li}_6\text{PS}_5\text{Cl}$. The findings on the change of structure and ionic conductivity of lithium argyrodites details the formation process of argyrodites during heat treatment and could provide a guideline for determining the fabrication of argyrodites, especially the annealing temperature. Moreover, it is found that argyrodites are electrochemically stable between 0-4 V and pelletized argyrodites are sufficiently compact so that the solid electrolyte layer mechanically separates cathode and anode materials thus preventing short circuits e.g. by lithium dendrite formation. These studies on lithium argyrodites shed light on their capability as candidates for solid electrolyte of ASSLBs.
2. All-solid-state $\text{CuS}/\text{Li}_6\text{PS}_5\text{Br}/\text{In-Li}$ batteries were realized, and the effects of the original states of the composite cathode (i.e. composite cathode prepared by mortar grinding or ball milling, and initially in discharged or charged state) were examined (Chapter 4). Ball milling of the composite cathode powder can reduce its particle size and uniformity, thus significantly increase the utilization of active cathode materials and consequently increase the initial capacity of the ASSLBs. However, the reversible

capacity of batteries using composite cathode prepared by either method shows similar values for a range of C rates. In addition, batteries assembled in discharged state (Cu-Li₂S) show a better cyclic performance than those in charged state (CuS).

This study also revealed a peculiar reaction mechanism of CuS in ASSLBs using Li₆PS₅Br solid electrolyte, and investigated the reasons for the capacity fading. It is found that during discharge Cu⁺ reversibly and partially exchange for Li⁺ in both Li₆PS₅Br and Li₂S, leading to Cu_yLi_{6-y}PS₅Br and Cu_zLi_{2-z}S. A maximum value of Cu content $y=1.59$ is observed around half discharge, representing over one quarter of Li⁺ substituted by Cu⁺. The smaller ionic conductivity of Cu₆PS₅Br than Li₆PS₅Br, together with the significant role of mixed mobile ion effect in reducing ionic conductivity, lead to an inferior ionic conductor. In addition, crack formation in composite cathode layer can be discerned during cycling. Therefore, the capacity fading of ASSLBs can be attributed to reduced ionic conductivity of solid electrolyte by Cu⁺ for Li⁺ substitution and to the severe volume change of active materials. This is in line with the findings on the effects of the original states of the composite cathode. Ball milling does not improve the reversible capacity of the batteries, as the volume change and cation exchange are not alleviated. On the other hand, batteries starting from discharged state (Cu-Li₂S) lead to volume shrinkage first, which causes less and slower damage to the battery, especially with the existence of residual compressive stress from pelletization.

Based on the deeper understanding of the reasons for the capacity fading of our ASSLBs, disadvantages of using CuS or Cu-Li₂S as cathode materials and the way to enhance the cyclic performance of ASSLBs (by eliminating sources of Cu⁺) became obvious. Besides, the finding on the unusual role of Cu⁺ in ASSLBs using lithium argyrodite solid electrolyte should also apply to other types of ASSLBs and even conventional liquid electrolyte batteries. This study therefore provides a potential explanation for the poor cyclic performance of most of the reported CuS batteries^{201,202,203} and the high dependence of the cyclic performance of CuS batteries on the choice of the liquid electrolyte²⁰⁴.

3. To eliminate the detrimental role of Cu⁺ in ASSLBs using lithium argyrodite solid electrolyte, all-solid-state S/Li₆PS₅Br/In-Li batteries were assembled and investigated

(Chapter 5). The composite cathode powder of sulfur, $\text{Li}_6\text{PS}_5\text{Br}$ and super P carbon was fabricated by a two-step ball milling at high rotating speed of 500 rpm yielding a uniform composite cathode mixture with a particle size smaller than 100 nm. The resulting all-solid-state $\text{S}/\text{Li}_6\text{PS}_5\text{Br}/\text{In-Li}$ batteries show a maximum capacity of 1460 mAh/g and reversible capacity of 1080 mAh/g after 50 cycles at C/10. The ASSLBs are highly sensitive to the air and their cyclic performance is to some extent weakened when cycling at the ambient atmosphere, probably due to imperfect sealing of Swagelok cell (the de facto standard experimental set-up for such battery testing). Therefore, battery testing in glove box is necessary in the current stage and optimization of cell case is required in the future. Ex-situ XRD results demonstrate that $\text{Li}_6\text{PS}_5\text{Br}$ undergoes no structural change throughout the cycling. Compared to the batteries using CuS and $\text{Cu-Li}_2\text{S}$ as cathode materials, the significantly enhanced cyclic performance of the all-solid-state Li/S batteries again supports the detrimental effect of Cu^+ in ASSLBs using $\text{Li}_6\text{PS}_5\text{Br}$ solid electrolyte.

4. A novel type of all-solid-state Li/S batteries is achieved by fully discharging the all-solid-state $\text{MoS}_2/\text{Li}_6\text{PS}_5\text{Br}/\text{In-Li}$ batteries (Chapter 6). Ball milling the composite cathode mixture of MoS_2 , lithium argyrodite and super P carbon leads to the uniformly mixing of these components. After a full discharge to 0.1 V vs. Li/Li^+ , the cell effectively becomes a Li/S cell with Mo nanoparticles finely dispersed in the composite cathode. The Mo particles are spheres with a diameter of around 7 nm. At room temperature, the cell demonstrates an initial discharge capacity of 650 mAh/g and reversible capacity of 385 mAh/g up to 5 cycles with a voltage scale of 0.1-3.0 V. These initial discharge cycles down to low voltages should effectively be considered as a pre-treatment step to ensure the full conversion of MoS_2 to Mo and $\text{S}/\text{Li}_2\text{S}$. Thereafter the cell showed a reversible capacity of 190 mAh/g up to 40 cycles at C/10 with a high coulombic efficiency when cycled in the practically useful voltage range 1-3 V. At non-ambient temperature of 70 °C, these cells exhibit a high rate capability up to 1C and a high capacity retention of 85% up to 700 cycles with a reversible capacity of 270 mAh/g at C/5. The high capacity retention sheds light on the great commercial viability of the resulting ASSLBs.

5. Theoretical and practical capacities of the ASSLBs combining S or MoS₂ cathode materials with lithium argyrodite solid electrolyte produced in this thesis project compare favorably well to conventional battery types (see Figure 7-1). The practical capacity of S is more than six times higher than the capacity of intercalation cathode materials used in conventional Li-ion batteries. Even taking into account the large amount of solid electrolyte and carbon required for S composite cathodes with high capacity retention (and the anode material mass), the practical capacity of such S composite cathode still doubles that of conventional cathode. Thereby despite the lower cell voltage the achieved energy density the sulfur battery is 490 Wh per kg of cathode composite material, still competitive to the 490 Wh/kg (LiCoO₂), 440 Wh/kg (LiMn₂O₄) or 460 Wh/kg (LiFePO₄) of conventional cathode materials for liquid electrolyte batteries.

In terms of energy density of the full cell, although the composite cathode to solid electrolyte ratio in the studied cells was not optimized, the achieved practical energy densities of these ASSLBs (up to 51 Wh/kg vs. Li/Li⁺) is 7 times higher than the one reported recently by a leading research group for an all-solid-state LiCoO₂/Li₆PS₅Cl/Li₄Ti₅O₁₂ battery.²⁰⁵ However, the practical full (single) cell energy densities of our (or any available) ASSLBs cannot yet reach those of liquid electrolyte batteries.

The key limitation for achieving a high practical energy density is the high solid electrolyte to composite cathode weight ratio. In the typical test cells, 12 mg of sulfur composite cathode are used with 100 mg of solid electrolyte. Simply reducing the weight of lithium argyrodite solid electrolyte to a value of 20 mg (corresponding to a solid electrolyte layer thickness of ca. 100 μm) will raise the energy density to 170 Wh/kg (vs. Li/Li⁺). Other significant ways to enhance the energy density are to introduce a higher mass fraction of the composite cathode in the battery, and to increase the percentage of active materials in the composite cathode. More work will be done in the future to optimize the weight ratio of the components of ASSLBs to achieve a high energy density over the current commercial LIBs.

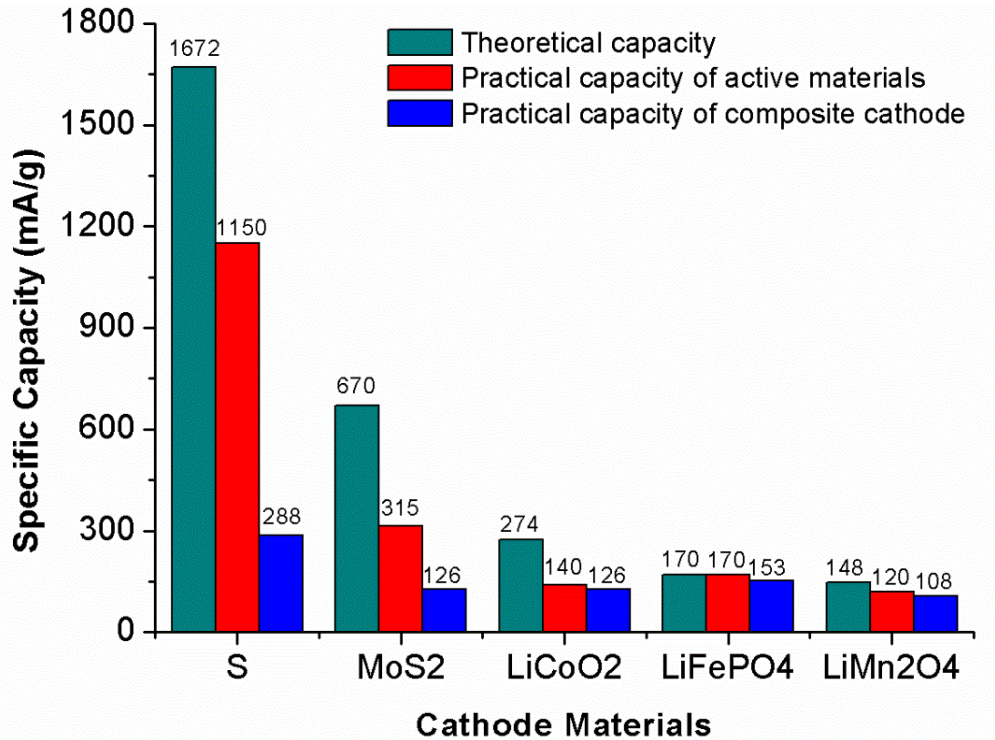


Figure 7-1 Theoretical and practical capacities of various cathode composite materials. The red columns of S and MoS₂ represent the practical capacity with respect to the amount of active material, while the blue columns represent the practical capacities with respect to the total weight of the composite cathode. The theoretical and practical capacities of LiCoO₂, LiFePO₄ and LiMn₂O₄ are taken from the literature.²⁰⁶

To further improve the performance of ASSLBs, several suggestions are proposed, as shown in the following:

1. More investigations on solid electrolytes are required to achieve the aims of: (a) higher ionic conductivity. Li₁₀GeP₂S₁₂²⁷ and Li₇P₃S₁₁⁷¹ have been reported with a high ionic conductivity in an order of 10⁻² S/cm, comparable to that of liquid electrolyte. In this respect, the recent case of Li₇P₃S₁₁ glass-ceramics is particularly encouraging, as the originally reported conductivity could be increased by a factor > 5 by improved thermal processing. Moreover, the possibility of further increasing the ionic conductivity of lithium argyrodites by doping should be explored, as this can prevent ordering process of the mobile charge carriers. This mechanism in fast ion conducting solids with high concentration of mobile charge carriers (such as the argyrodites) is effectively somewhat different from the doping of materials with low intrinsic conductivity, where the doping essentially serves to increase the number of charge carriers. (b) For

industrial application it may be even more important to explore the doping of argyrodites to enhance their chemical stability (especially with respect to hydrolysis). A preliminary study in this direction has been briefly discussed in section 3.6. As one of the key factors limiting the chemical stability of lithium argyrodites is the high reactivity of their decomposition product Li_3PS_4 , according to the simulation result of our group. Substitution of P by other elements such as Sn or Ge may enhance the hydrolysis stability.

2. MoS_2 nanosheets or nanoparticles should be prepared and their application to ASSLBs as cathode materials should be investigated. As discussed in Chapter 6, the ASSLB using raw MoS_2 powder (with a relatively large diameter of 1-10 μm) experienced a drastic capacity fading at the second cycle, which should be ascribed to the severe volume expansion of the active materials. Reducing the particle size should be helpful in mitigating the detrimental effect of the volume change. The employment of finely nanoparticles to some extent can allow more realignment/movement of the materials in the composite cathode and thus compensate the volume changes during cycling, leading to an enhanced cyclic performance of the resulting batteries. Recent studies on the liquid electrolyte batteries using nanostructured MoS_2 as electrode materials have demonstrated high cyclic performance of the batteries, where nanostructured MoS_2 powders were prepared by hydrothermal techniques¹⁷¹, template method¹⁷² or lithium-assisted exfoliation¹⁷³. In the future, the nanostructured MoS_2 will be studied as cathode materials of ASSLBs in combination with lithium argyrodite solid electrolyte.
3. Buffer materials for the composite cathode should be optimized. Most of the conversion materials show severe volume change during cycling. Therefore, buffer materials, typically carbonaceous materials, are playing a key role in achieving a high capacity retention for ASSLBs. In this study, super P carbon were used as the buffer material as well as the electronic conductor, considering its high void volume and high electronic conductivity²⁰⁷. On the other hand, other carbonaceous materials, such as graphene, Ketjen black and carbon nanotube, which vary in specific surface area, void volume and electronic conductivity, can be explored in ASSLBs as well.

4. Other kinds of anode materials need to be tested in the ASSLB system. In this study, indium-lithium alloy is employed as the anode in order to ensure the stability of the ASSLBs allowing the project to focus on the cathode and cathode:electrolyte interface. However, the potential of In vs. Li/Li⁺ (0.6 V) reduces the cell voltage and hence the energy density of the resulting batteries. Therefore and to avoid the high cost of indium, it is advisable to replace the In-Li alloy with other kinds of anode materials. An example is metallic lithium. It has been reported that internal short-circuit may occur to the ASSLBs using Li as anode during charging²⁰⁸, which should be ascribed to the dendritic formation, leading to the poor cyclic performance of the batteries. Similar phenomenon frequently occurred in my preliminary studies on ASSLBs as well. Nagao et al.²⁰⁸ reported formation of a favorable Li-solid electrolyte interface by depositing a lithium layer on the solid electrolyte using vacuum-evaporation techniques, thus achieving a better cyclic performance. More studies are required on mitigating or even eliminating the lithium growth in ASSLBs. Other alternatives are high capacity anode materials that can alloy with lithium, such as aluminum²⁰⁹ with capacity of 994 mAh/g and silicon with capacity of 4200 mAh/g^{210,211}.

With the further improvements outlined above, ASSLBs may not only promise significantly improved safety, but can also achieve high energy density, power density, cyclability and reliability. Accordingly, ASSLBs can become a commercially viable product applicable to a wide range of areas, such as electric vehicles, electronic devices and stationary energy storage systems, etc.

PUBLICATION LIST

JOURNAL PUBLICATION

M. Chen, S. Adams, All-solid-state MoS₂/Li₆PS₅Br/In-Li batteries as a novel type of Li/S batteries, *submitted to J. Mater. Chem. A*.

M. Chen, S. Adams, High performance all-solid-state lithium/sulfur batteries using lithium argyrodite electrolyte, *J. Solid State Electrochem.* (2014), in press, DOI: 10.1007/s10008-014-2654-1.

M. Chen, R.P. Rao, S. Adams, The unusual role of Li₆PS₅Br in all-solid-state CuS/Li₆PS₅Br/In-Li batteries, *Solid State Ionics* 268 (2014) 300.

M. Chen, R.P. Rao, S. Adams, High capacity all-solid-state Cu-Li₂S/Li₆PS₅Br/In batteries, *Solid State Ionics* 262 (2014) 183.

X. Yin, C. Tang, **M. Chen**, S. Adams, H. Wang, H. Gong, Hierarchical porous Cu₂ZnSnS₄ films for high-capacity reversible lithium storage applications, *J. Mater. Chem. A* 1 (2013) 7927.

R.P. Rao, **M. Chen**, S. Adams, Preparation and characterization of NASICON type Li⁺ ionic conductors, *J. Solid State Electrochem.* 16 (2012) 3349.

CONFERENCE CONTRIBUTIONS

Invited

R.P. Rao, **M. Chen** and S. Adams, "Li-ion conducting solid electrolytes for Lithium Sulfur batteries", invited talk at *International Nanotechnology Conference* (24 - 28 Mar 2014, Nsukka/Nigeria)

R.P. Rao, **M. Chen**, N. Sharma, V.K. Peterson and S. Adams, "Sulfur based solid electrolytes for safe new generation rechargeable Lithium batteries", invited talk at *International Battery Association* (2 - 7 Mar 2014, Brisbane/Australia)

S. Adams, **M. Chen**, and R.P. Rao, "Fast Lithium ion conductors for high power solid state batteries", Invited talk presented at *6th Asian Conference on Electrochemical Power Sources* (5 - 8 Jan 2012, Chennai/India)

S. Adams, R.P. Rao, and **M. Chen**, "Fast Li⁺ ion conductors for solid state batteries", Invited talk at *Materials Science and Technologies (MS&T 2011) conference* (16 - 20 Oct 2011, Columbus/United States)

Oral

M. Chen, R.P. Rao, and S. Adams, "All-solid-state lithium batteries using Li₆PS₅Br solid electrolyte", oral presentation at *14th Asian Conference on Solid State Ionics* (24 Jun - 27 Jul 2014, Singapore)

R.P. Rao, **M. Chen** and S. Adams, "Low temperature processing of lithium argyrodites and Li₁₀GeP₂S₁₂ for all-solid state batteries", oral presentation at *2013 MRS Fall Meeting & Exhibit* (1 - 6 Dec 2013, Boston/United States)

M. Chen, R.P. Rao, and S. Adams, "High capacity all-solid-state CuS/Li argyrodite/In-Li batteries", oral presentation at *ICMAT 2013 Conference on Materials for Advanced Technologies* (30 Jun - 5 Jul 2013, Singapore)

M. Chen, R.P. Rao, and S. Adams, "High capacity all-solid-state CuS/Li argyrodite/In-Li batteries", oral presentation at *2013 MRS Spring Meeting & Exhibit* (1-5 April, 2013, San Francisco/United State)

R.P. Rao, **M. Chen** and S. Adams, "Variation of ionic conductivity with annealing temperature in argyrodite solid electrolyte", oral presentation at *13th Asian Conference on Solid State Ionics - Ionics for Sustainable world* (17 - 20 Jul 2012, Sendai/Japan)

M. Chen, R.P. Rao, and S. Adams, "Structural stability and ion migration mechanism in Li₇La₃Zr₂O₁₂", oral presentation at *International Conference on Materials for Advanced Technologies* (26 Jun - 1 Jul 2011, Singapore)

Poster

M. Chen and S. Adams, “All-solid-state $\text{MoS}_2/\text{Li}_6\text{PS}_5\text{Br}/\text{In-Li}$ batteries as a novel type of Li/S batteries”, poster at *6th MRS-S Conference on Advanced Materials* (22-24 July, 2014, Singapore)

M. Chen, R.P. Rao, and S. Adams, “All-solid-state Li/S batteries using $\text{Li}_6\text{PS}_5\text{Br}$ as electrolyte”, poster at *1st Singapore Battery Meeting (SGBM) 2014* (27-28 Feb., 2014, Singapore)

M. Chen, R.P. Rao, and S. Adams, “Electrochemical behaviour of CuS in all-solid-state battery with $\text{Li}_6\text{PS}_5\text{Br}$ as electrolyte”, poster at *4th Trilateral MRS Conference* (5-7 Dec 2013, Singapore)

M. Chen, R.P. Rao, and S. Adams, “High capacity all-solid-state Cu-Li $2\text{S}/\text{Li}_6\text{PS}_5\text{Br}/\text{In}$ batteries”, poster at *19th International Conference on Solid State Ionics* (2-7 Jun 2013, Kyoto/Japan)

R.P. Rao, **M. Chen**, and S. Adams, “Variation of ionic conductivity with annealing temperature in Argyrodite solid electrolytes”, poster at *13th Asian Conference on Solid State Ionics* (17 - 20 Jul 2012, Sendai/Japan)

M. Chen, R.P. Rao, and S. Adams, "Structure dependence of ionic conductivity of lithium argyrodite solid electrolytes", poster at *International Conference of Young Researchers on Advanced Materials ICYRAM2012* (1 - 6 Jul 2012, Singapore)

R.P. Rao, **M. Chen**, N. Sharma, V.K. Peterson, and S. Adams, “Structure dependence of electrochemical performance of lithium argyrodite solid electrolytes”, *5th MRS-S Conference on Advanced Materials* (20 - 22 Mar 2012, Singapore)

R.P. Rao, **M. Chen**, and S. Adams, “Structure, transport and electrochemical performance of $\text{Li}_{1.3}\text{M}_{0.3}\text{Ti}_{1.7}(\text{PO}_4)_3$ ($\text{M}=\text{Fe}^{3+}$, Al^{3+})”, *18th International Conference on Solid State Ionics* (3 - 8 Jul 2011, Warsaw/Poland)

M. Chen, R.P. Rao, and S. Adams, “Structural Stability and Ion Migration Mechanism in $\text{Li}_7\text{La}_3\text{Zr}_2\text{O}_{12}$ ”, *ICMAT 2011 Conference on Advanced Materials for Energy Storage Systems - From Fundamentals to Applications* (26 Jun - 1 Jul 2011, Singapore)

R.P. Rao, **M. Chen**, and S. Adams, “Preparation and characterization of NASICON type Li⁺ ionic conductors”, *ICMAT 2011 Conference on Advanced Materials for Energy Storage Systems - From Fundamentals to Applications* (26 Jun - 1 Jul 2011, Singapore)

R.P. Rao, **M. Chen**, and S. Adams, “Ionic conductivity studies of NASICON type Li⁺ ionic conductors”, *Lithium Batteries Discussion Meeting 2011* (12 - 17 Jun 2011, Arcachon/ France)

REFERENCES

- ¹ J.M. Tarascon and M. Armand, *Nat.* 414 (2001) 359.
- ² M.S. Whittingham, *ChemInform* 35 (2004) 4271.
- ³ M. S. Whittingham, *Sci.* 192 (1976) 1126.
- ⁴ M. S. Whittingham, Vol. 4009052, U.S., 1976.
- ⁵ K. Mizushima, P.C. Jones, P.J. Wiseman, and J.B. Goodenough, *Mater. Res. Bull.* 15 (1980) 783.
- ⁶ M.M. Thackeray, W. I. F. David, P. G. Bruce, and J. B. Goodenough, *Mater. Res. Bull.* 18 (1983) 461.
- ⁷ M. Armand, in *Materials for Advanced Batteries* (eds. D. W. Murphy, J. Broadhead, and B. C. H. Steele), Plenum Press, New York, 1980.
- ⁸ B. Scrosati, *J. Electrochem. Soc.* 139 (1992) 2776.
- ⁹ J.O. Besenhard, and H.P. Fritz, *J. Electroanal. Chem.* 53 (1974) 329.
- ¹⁰ J.O. Besenhard, and G. Eichinger, *J. Electroanal. Chem.* 68 (1976) 1.
- ¹¹ R. Yazami, and P. Touzain, *J. Power Sources* 9 (1983) 365.
- ¹² A. Yoshino, K. Sanechika, and T. Nakajima, Vol. 4668595, Asahi Chemical Ind, U.S., 1985.
- ¹³ G. Feuillade, and Ph. Perche, *J. Appl. Electrochem.* 5 (1975) 63.
- ¹⁴ Y. Aihara, G.B. Appetecchi, and B. Scrosati, *J. Electrochem. Soc.* 149 (2002) A849.
- ¹⁵ J.N. Mrgudich, *Batteries, solid electrolyte*, in: C.A. Hampel (Ed.), *Encyclopedia of Electrochemistry*, Reinhold Publishing, New York, 1964.
- ¹⁶ B.B. Owens, *J. Power Sources* 90 (2008) 2.
- ¹⁷ B.B. Owens, G.R. Argue, *J. Electrochem. Soc.* 117 (1970) 1536.
- ¹⁸ C. Julien, and G.-A. Nazri, *Solid state batteries: materials design and optimization*, Kluwer Academic, Boston, 1994.
- ¹⁹ M. Armand, J.M. Chabagno and M.J. Duclot, in *Fast Ion Transport in Solids Electrodes and Electrolytes*, North-Holland, Amsterdam, 1979.
- ²⁰ K. Takada, T. Inada, A. Kajiyama, M. Kouguchi, H. Sasaki, S. Kondo, Y. Michiue, S. Nakano, M. Tabuchi, and M. Watanabe, *Solid State Ionics* 172 (2004) 25.
- ²¹ M.Duclot and J.-L. Souquet, *J. Power Sources* 97–98 (2001) 610.
- ²² S.D. Jones and J.R. Akridge, *Solid State Ionics* 86–88 (1996) 1291.
- ²³ D. Bresser, S. Passerini and B. Scrosati, *Chem. Commun.* 49 (2013) 10545
- ²⁴ M. Barghamadi, A. Kapoor and C. Wen, *J. Electrochem. Soc.* 160 (2013) A1256.
- ²⁵ H. Li, Y. Wang, X. Yang, L. Liu, L. Chen, and J. Wei, *Solid State Ionics* 255 (2014) 84.
- ²⁶ W.W. Wu, H.F. Xiang, G.B. Zhong, W. Su, W. Tang, Y. Zhang, Y. Yu, and C.H. Chen, *Electrochim. Acta* 119 (2004) 206.
- ²⁷ N. Kamaya, K. Homma, Y. Yamakawa, M. Hirayama, R. Kanno, M. Yonemura, T. Kamiyama, Y. Kato, S. Hama, K. Kawamoto, and A. Mitsui, *Nat. Mater.* 10 (2011) 682.
- ²⁸ K. Koji, in *Nikkei Electronics Asia*, Nikkei Business Publications, Japan, 2010.
- ²⁹ WinterGreen Research, Inc., 2012.
- ³⁰ U.V. Alpen, A. Rabenau, and G.H. Talat, *Appl. Phys. Lett.* 30 (1977) 621.
- ³¹ T. Lapp, S. Skaarup, and A. Hooper, *Solid State Ionics* 11 (1983) 97.
- ³² E. Quartarone, and P. Mustarelli, *Chem. Soc. Rev.* 40 (2011) 2525.
- ³³ N. Li, L. Wang, X. He, C. Wan, C. Jiang, *Ionics* 14 (2008) 463.

-
- ³⁴ S.K. Fullerton-Shirey, and J.K. Maranas, *J. Phys. Chem. C* 114 (2010) 9196.
- ³⁵ F. Croce, L. Settimi, B. Scrosati, and D. Zame, *J. New Mat. Electrochem. Systems* 9 (2006) 3.
- ³⁶ G. Zardalidis, E. Ioannou, S. Pispas, and G. Floudas, *Macromolecules* 46 (2013) 2705.
- ³⁷ W. Gorecki, M. Jeannin, E. Belorizky, C. Roux, and M. Armand, *J. Phys.: Condens. Matter* 7 (1995) 6823
- ³⁸ L.Z. Fan, X.-L. Wang, F. Long, and X. Wang, *Solid State Ionics* 179 (2008) 1772.
- ³⁹ T. Itoh, K. Hirai, T. Uno, and M. Kubo, *Ionics* 14 (2008) 1.
- ⁴⁰ H.M.J.C. Pitawala, M.A.K.L. Dissanayake, V.A. Seneviratne, B.-E. Mellander, and I. Albinson, *J. Solid State Electrochem.* 12 (2008) 783.
- ⁴¹ S.A. Suthanthiraraj, and D.J. Sheeba, *Ionics*, 13 (2007) 447
- ⁴² Y.W. Chen-Yang, Y.L. Wang, Y.T. Chen, Y.K. Li, H.C. Chen, and H.Y. Chiu, *J. Power Sources* 182 (2008) 340.
- ⁴³ J. Adebahr, A.S. Best, N. Byrne, P. Jacobsson, D.R. MacFarlane, and M. Forsyth, *Phys. Chem. Chem. Phys.* 5 (2003)720.
- ⁴⁴ G.T. Kim, G.B. Appetecchi, M. Carewska, M. Joost, A. Balducci, M. Winter, and S. Passerini, *J. Power Sources* 195 (2010) 6130.
- ⁴⁵ S.Y. An, I.C. Jeong, M.-S. Won, E.D. Jeong, Y.-B. Shim, *J. Appl. Electrochem.* 39 (2009) 1573.
- ⁴⁶ T.J. Singh, and S.V. Bhat, *Bull. Mater. Sci.* 26 (2003) 707.
- ⁴⁷ T. Uno, S. Kawaguchi, M. Kubo, and T. Itoh, *J. Power Sources* 178 (2008) 716.
- ⁴⁸ Z. Bakenov, M. Nakayama, M. Wakihara, I. Taniguchi, *J. Solid State Electrochem.* 12 (2008) 295.
- ⁴⁹ P.G. Bruce, and A.R. West, *J. Electrochem. Soc.* 130 (1983) 662.
- ⁵⁰ Y.G. Sun, *Nano Energy* 2 (2013) 801.
- ⁵¹ P. Knauth, *Solid State Ionics* 180 (2009) 911.
- ⁵² J.A. Alonso, J. Sanz, J. Santamaria, C. Leon, A. Varez, and M.T. Fernandez-Diaz, *Angew. Chem. In. Ed.* 39 (2000) 619.
- ⁵³ S. Stramare, V. Thangadurai, and W. Weppner, *Chem. Mater.* 15 (2003) 3974.
- ⁵⁴ R. Murugan, V. Thangadurai, and W. Weppner, *Angew. Chem. In. Ed.* 46 (2007) 7778.
- ⁵⁵ C.A. Geiger, E. Alekseev, B. Lazic, M. Fisch, T. Armbruster, R. Langner, M. Fechtelkord, N. Kim, T. Pettke, and W. Weppner. *Inorg. Chem.* 50 (2011) 1089.
- ⁵⁶ S. Adams, and R.P. Rao, *J. Mater. Chem.* 22 (2011) 1426.
- ⁵⁷ A. Logeat, T. Kohler, U. Eisele, B. Stiaszny, A. Harzer, M. Tovar, A. Senyshyn, H. Ehrenberg, B. Kozinsky, *Solid State Ionics* 206 (2012) 33.
- ⁵⁸ J.B. Bates, N.J. Dudney, G.R. Gruzalski, and R.A. Zuhr, *Solid State Ionics* 53-56 (1992) 647.
- ⁵⁹ J.W. Long, B. Dunn, D.R. Rolison, and H.S. White, *Chem. Rev.* 104 (2004) 4463.
- ⁶⁰ Z. Zhang, and J.H. Kennedy, *Solid State Ionics* 38 (1990) 217.
- ⁶¹ T. Ohtomo, A. Hayashi, M. Tatsumisago, and K. Kawaomto, *J. Solid State Electrochem.* 17 (2013) 2551.
- ⁶² F. Mizuno, A. Hayashi, K. Tadanaga, and M. Tatsumisago, *Adv. Mater.* 17 (2005) 918.
- ⁶³ S. Ujiie, A. Hayashi, and M. Tatsumisago, *J. Solid State Electrochem.* 17 (2013) 675
- ⁶⁴ K. Minami, A. Hayashi, and M. Tatsumisago, *J. Cera. Soc. JPN* 118 (2010) 305.
- ⁶⁵ M. Nagao, Y. Imade, H. Narisawa, T. Kobayashi, R. Watanabe, T. Koyoi, T. Tatsumi, and R. Kanno, *J. Power Sources* 222 (2013) 237.

-
- ⁶⁶ Y. Wang, Z. Liu, X. Zhu, Y. Tang, and F. Huang, *J. Power Sources* 224 (2013) 225.
- ⁶⁷ N. Kamaya, K. Homma, Y. Yamakawa, M. Hirayama, R. Kanno, M. Yonemura, T. Kamiyama, Y. Kato, S. Hama, K. Kawamoto, and A. Mitsui, *Nat. Mater.* 10 (2011) 682.
- ⁶⁸ S. Adams and R. Prasada Rao, *J. Mater. Chem.* 22 (2012) 7687.
- ⁶⁹ A. Kuhn, J. Köhler and B.V. Lotsch, *Phys. Chem. Chem. Phys.* 15 (2013) 11620.
- ⁷⁰ P.E. Stallworth, J.J. Fontanella, M.C. Wintersgill, C.D. Scheidler, J.J. Immel, S.G. Greenbaum, and A.S. Gozdz, *J. Power Sources* 81–82 (1999) 739.
- ⁷¹ Y. Seino, T. Ota, K. Takada, A. Hayashi, and M. Tatsumisago, *Energy Environ. Sci.* 7 (2014) 627.
- ⁷² J.W. Fergus, *J. Power Sources* 195 (2010) 4554.
- ⁷³ A. Weisbach, *Neues Jahrb. Mineral.* 2 (1886) 67.
- ⁷⁴ C. Winkler, *Ber. Dtsch. Chem. Ges.* 19 (1886) 210.
- ⁷⁵ A. Haznar, A. Pietraszko, and I.P. Studenyak, *Solid State Ionics* 119 (1999) 31.
- ⁷⁶ W.F. Kuhs, R. Nitsche, and K. Scheunemann, *Mat. Res. Bull.* 14 (1979) 241.
- ⁷⁷ R.B. Beeken, J.J. Garbe, J.M. Gillis, N.R. Petersen, B.W. Podoll, and M.R. Stoneman, *J. Phys. Chem. Solids* 66 (2005) 882.
- ⁷⁸ M. Evain, E. Gaudin, F. Boucher, V. Petricek, and F. Taulelle, *Acta Crystallogr. B* 54 (1998) 376.
- ⁷⁹ M. Onoda, H. Wada, A. Sato, and M. Ishii, *J. Alloys Compd.* 238 (2004) 113.
- ⁸⁰ S.-T. Kong, H.-J. Deiseroth, C. Reiner, O. Gun, E. Neumann, C. Ritte, and D. Zahn, *Chem. Eur. J.* 16 (2010) 2198.
- ⁸¹ A.F. Orliukas, A. Kežionis, E. Kazakevičius, T. Šalkus, M.I. Kayla, M. Kranjčec, and I.P. Studenyak, *Solid State Ionics* 251 (2013) 83.
- ⁸² W.F. Kuhs, R. Nitsche, and K. Scheunemann, *Acta Crystallogr. B* 34 (1978) 64.
- ⁸³ R.B. Beeken, J.J. Garbe, and N.R. Petersen, *J. Phys. Chem. Solids* 64 (2003) 1261.
- ⁸⁴ H.-J. Deiseroth, S.-T. Kong, H. Eckert, J. Vannahme, C. Reiner, T. Zaiß, and M. Schlosser, *Angew. Chem. Int. Ed.* 47 (2008) 755.
- ⁸⁵ F. Stadler, and C. Fietzek, *ECS transactions*, 25 (2010) 177.
- ⁸⁶ S.-T. K, H.-J. Deiseroth, J. Maier, V. Nickel, K. Weichert, and C. Reiner, *Z. Anorg. Allg. Chem.* 636 (2010) 1920.
- ⁸⁷ M.R. Palacín, *Chem. Soc. Rev.* 8 (2009) 2565.
- ⁸⁸ C.-X. Zu and H. Li, *Energy Environ. Sci.* 4 (2011) 2614.
- ⁸⁹ M. Winter, J. O. Besenhard, M. E. Spahr, and P. Novák, *Adv. Mater.* 10 (1998) 725.
- ⁹⁰ C.M. Julien and M. Massot, *Mater. Sci. Engin. B* 97 (2003) 217.
- ⁹¹ F. Ding, W. Xu, D. Choi, W. Wang, X. Li, M.H. Engelhard, X. Chen, Z. Yang, and J.-G. Zhang, *J. Mater. Chem.* 22 (2012) 12745.
- ⁹² X.-Y. Qiu, Q.-C. Zhuang, Q.-Q. Zhang, R. Cao, P.-Z. Ying, Y.-H. Qiang, and S.-G. Sun, *Phys. Chem. Chem. Phys.* 14 (2012) 2617.
- ⁹³ S. Adams, *J. Solid State Electrochem.*, 14 (2010) 1787.
- ⁹⁴ B. A. Boukamp, G. C. Lesh, and R. A. Huggins, *J. Electrochem. Soc.* 128 (1981) 725.
- ⁹⁵ U. Kasavajjula, C. Wang, A.J. Appleby, *J. Power Sources* 163 (2007) 1003.
- ⁹⁶ P. Poizot, S. Laruelle, S. Grugéon, L. Dupont, and J. M. Tarascon, *Nat.* 407 (2000) 496.
- ⁹⁷ Y. Oumellal, A. Rougier, G. A. Nazri, J. M. Tarascon, and L. Aymard, *Nat. Mater.* 7 (2008) 916.
- ⁹⁸ N. Pereira, L. C. Klein, and G. G. Amatucci, *J. Electrochem. Soc.* 149 (2002) A262.

-
- ⁹⁹ P. Poizot, S. Laruelle, S. Grugeon, and J.-M. Tarascon, *J. Electrochem. Soc.* 149 (2002) A1212.
- ¹⁰⁰ D.C.C. Silva, O. Crosnier, G. Ouvrard, J. Greedan, A. Safa-Sefat, and L.F. Nazar, *Electrochem. Solid-State Lett.* 6 (2003) A162.
- ¹⁰¹ Y. Wang, Z.-W. Fu, X.-L. Yue, and Q.-Z. Qin, *J. Electrochem. Soc.* 151 (2004) E162.
- ¹⁰² S. Iijima, *Nature* 354 (1991) 56.
- ¹⁰³ N. Jayaprakash, J. Shen, S.S. Moganty, A. Corona, and L.A. Archer, *Angew. Chem. Int. Ed.* 50 (2011) 5904.
- ¹⁰⁴ T. Kobayashi, Y. Imade, D. Shishihara, K. Homma, M. Nagao, R. Watanabe, T. Yokoi, A. Yamada, R. Kanno, and T. Tatsumi, *J. Power Sources* 182 (2008) 621.
- ¹⁰⁵ H. Li, G. Richter, and J. Maier, *Adv. Mater.* 15 (2003) 736.
- ¹⁰⁶ Y.F. Zhukovskii, P. Balaya, E.A. Kotomin, and J. Maier, *Phys. Rev. Lett.* 96 (2006) 058302.
- ¹⁰⁷ T. Ohzuku, and A. Ueda, *J. Electrochem. Soc.* 141 (1994) 2972.
- ¹⁰⁸ *Nanomaterials for Lithium-Ion Batteries: Fundamentals and Applications* (ed. R. Yazami), Pan Stanford publishing, 2013.
- ¹⁰⁹ A. D̄bart, L. Dupont, R. Patrice, and J. M. Tarascon, *Solid State Sciences* 8 (2006) 640.
- ¹¹⁰ J.-W. S, Y.-W. Jun, S.-W. Park, H. Nah, T. Moon, B. Park, J.-G. Kim, Y.J. Kim, and J. Cheon, *Angew. Chem. Int. Ed.* 56 (2007) 8828.
- ¹¹¹ Y. Nishio, H. Kitaura, A. Hayashi, and M. Tatsumisago, *J. Power Sources* 189 (2009) 629.
- ¹¹² *Handbook of Batteries* (eds. D. Linden, T. B. Reddy), McGraw-Hill, New York, 2002.
- ¹¹³ <https://www.materialsproject.org/> (Retrieved on 20 July 2014)
- ¹¹⁴ F. Zhou, M. Cococcioni, C. Marianetti, D. Morgan, and G. Ceder, *Phys. Rev. B* 70 (2004) 235121.
- ¹¹⁵ K. Zhong, X. Xia, B. Zhang, H. Li, Z. Wang, and L. Chen, *J. Power Sources* 195 (2010) 3300.
- ¹¹⁶ K. Zhong, B. Zhang, S. Luo, W. Wen, H. Li, X. Huang, and L. Chen, *J. Power Sources* 196 (2011) 6802.
- ¹¹⁷ G. Huang, T. Chen, Z. Wang, K. Chang, and W. Chen, *J. Power Sources* 235 (2013) 122.
- ¹¹⁸ A. Ueda, M. Nagao, A. Inoue, A. Hayashi, Y. Seino, T. Ota, and M. Tatsumisago, *J. Power Sources* 244 (2013) 597.
- ¹¹⁹ A. Hayashi, T. Ohtomo, F. Mizuno, K. Tadanaga, and M. Tatsumisago, *Electrochem. Commun.* 5 (2003) 701
- ¹²⁰ A. Hayashi, Y. Nishio, H. Kitaura, and M. Tatsumisago, *Electrochem. Commun.* 10 (2008) 1860.
- ¹²¹ K. Aso, A. Sakuda, A. Hayashi, and M. Tatsumisago, *Appl. Mater. Interfaces* 5 (2013) 685.
- ¹²² M. Nagao, A. Hayashi, and M. Tatsumisago, *Electrochim. Acta* 56 (2011) 6055.
- ¹²³ H. Grijalva, M. Inoue, S. Boggavarapu and P. Calvert, *J. Mater. Chem.* 6 (1996) 1157.
- ¹²⁴ A. D̄bart, L. Dupont, R. Patrice, and J. M. Tarascon, *Solid State Sci.* 8 (2006) 640.
- ¹²⁵ G. Eichinger, and H.P. Fritz, *Electrochem. Acta* 20 (1975) 753.
- ¹²⁶ M. Hughes, N.A Hampson, and S. Karunathilaka, *J. Power Sources* 12 (1984) 144.
- ¹²⁷ I. Exner, and J. Hep, *J. Power Sources* 12 (1984) 153.
- ¹²⁸ J.-S. Chung, and H.-J. Sohn, *J. Power Sources* 108 (2002) 226.
- ¹²⁹ N. Yamakawa, M. Jiang, and C.P. Grey, *Chem. Mater.* 21 (2009) 3162.

-
- ¹³⁰ A. Hayashi, T. Ohmoto, F. Mizuno, K. Tadanaga, and M. Tatsumisago, *Electrochem. Acta* 50 (2004) 893.
- ¹³¹ N. Machida, K. Kobayashi, Y. Nishikawa, and T. Shigematsu, *Solid State Ionics* 175 (2004) 247.
- ¹³² A. Hayashi, R. Ohtsubo, and M. Tatsumisago, *Solid State Ionics* 179 (2008) 1702.
- ¹³³ A. Hayashi, R. Ohtsubo, T. Ohtomo, F. Mizuno, and M. Tatsumisago, *J. Power Sources* 183 (2008) 422.
- ¹³⁴ D. Marmorstein, T.H. Yu, K.A. Striebel, F.R. McLarnon, J. Hou, and E.J. Cairns, *J. Power Sources* 89 (2009) 219.
- ¹³⁵ N.A. Canas, S. Wolf, N. Wagner, and K.A. Friedrich, *J. Power Sources* 226 (2013) 313.
- ¹³⁶ Y.-S. Su, Y. Fu, T. Cochell, and A. Manthiram, *Nat. Commun.* 4 (2013) 2985.
- ¹³⁷ M. Hagen, P. Schiffels, M. Hammer, S. Dorfler, J. Tubke, M.J. Hoffmann, H. Althues, and S. Kaskel, *J. Electrochem. Soc.* 160 (2013) A1205.
- ¹³⁸ S. Walus, C. Barchasz, J.-F. Colin, J.-F. Martin, E. Elkaim, J.-C Lepretre, and F. Alloin, *Chem. Commun.* 49 (2013) 7899.
- ¹³⁹ X. Ji, and L.F. Nazar, *J. Mater. Chem.* 20 (2010) 9821.
- ¹⁴⁰ B.M.L. Rao, and J.A. Shropshire, *J. Electrochem. Soc.* 128 (1981) 942.
- ¹⁴¹ H. Yamin, and E. Peled, *J. Power Sources* 9 (1983) 281.
- ¹⁴² Y.-J. Choi, Y.-D. Chung, C.-Y. Baek, K.-W. Kim, H.-J. Ahn, and J.-Y. Ahn, *J. Power Sources* 184 (2008) 548.
- ¹⁴³ Z. Lin, Z. Liu, W. Fu, N.-J. Dudney, and C. Liang, *Angew. Chem. Int. Ed.* 52 (2013) 7460.
- ¹⁴⁴ X. Ji, K.T. Lee, and L.F. Nazar, *Nat. Mater.* 8 (2009) 500.
- ¹⁴⁵ L. Yin, J. Wang, F. Lin, J. Yang, and Y. Nuli, *Energy Environ. Sci.* 5 (2012) 6966.
- ¹⁴⁶ Y. Yang, G. Yu, J. J. Cha, H. Wu, M. Vosgueritchian, Y. Yao, Z. Bao, and Y. Cui, *ACS Nano* 5 (2011) 9187.
- ¹⁴⁷ B. Zhang, X. Qin, G.R. Li, and X.P. Gao, *Energy Environ. Sci.* 3 (2010) 1531.
- ¹⁴⁸ D. Aurbach, E. Pollak, R. Elazari, G. Salitra, C.S. Kelley, and J. Affinito, *J. Electrochem. Soc.* 156 (2009) A694.
- ¹⁴⁹ X. Liang, Z. Wen, Y. Liu, M. Wu, J. Jin, H. Zhang, and X. Wu, *J. Power Sources* 196 (2011) 9839.
- ¹⁵⁰ S.S. Zhang, *J. Electrochem. Soc.*, 159 (2012) A920.
- ¹⁵¹ S. Xiong, X. Kai, X. Hong, and Y. Diao, *Ionics*, 18 (2012) 249.
- ¹⁵² L.X. Yuan, J.K. Feng, X.P. Ai, Y.L. Cao, S.L. Chen, and H.X. Yang, *Electrochem. Commun.* 8 (2006) 610.
- ¹⁵³ M. Nagao, A. Hayashi, and M. Tatsumisago, *Energy Technol.* 1 (2013) 186.
- ¹⁵⁴ M. Agostini, Y. Aihara, T. Yamada, B. Scrosati, and J. Hassoun, *Solid State Ionics* 244 (2013) 48.
- ¹⁵⁵ S. Kinoshita, K. Okuda, N. Machida, M. Naito, and T. Shigematsu, *Solid State Ionics* 256 (2014) 97.
- ¹⁵⁶ H. Nagata, and Y. Chikusa, *J. Power Sources* 264 (2014) 206.
- ¹⁵⁷ X. Fang, X. Guo, Y. Mao, C. Hua, L. Shen, Y. Hu, Z. Wang, F. Wu, and L. Chen, *Chem. Asian J.* 7 (2012) 1013.
- ¹⁵⁸ J. Xiao, X. Wang, X.-Q. Yang, S. Xun, G. Liu, P.K. Koech, J. Liu, and J.P. Lemmon, *Adv. Funct. Mater.* 21 (2011) 2840.
- ¹⁵⁹ X. Huang, Z. Zeng, and H. Zhang, *Chem. Soc. Rev.* 41 (2013) 1934.

-
- ¹⁶⁰ G. Eda, H. Yamaguchi, D. Voiry, T. Fujita, M.W. Chen, and M. Chhowalla, *Nano Lett.* 11 (2011) 5111.
- ¹⁶¹ S.J. Sandoval, D. Yang, R.F. Frindt, and J.C. Irwin, *Phys. Rev. B: Condens. Matter Mater. Phys.* 44 (1991) 3955.
- ¹⁶² M.G. Sibi, B.S. Rana, L.N.S. Konathala, G.D. Thakre, S. Saran, and A.K. Sinha, *J. Mater. Res.*, 28 (2013) 1962.
- ¹⁶³ Y. Li, H. Wang, L. Xie, Y. Liang, G. Hong, and H. Dai, *J. Am. Chem. Soc.* 133 (2011) 7296.
- ¹⁶⁴ Y. Tan, K. Yu, T. Yang, Q. Zhang, W. Cong, H. Yin, Z. Zhang, Y. Chen, and Z. Zhu, *J. Mater. Chem. C*, 2 (2014) 5422.
- ¹⁶⁵ B. Radisavljevic, A. Radenovic, J. Brivio, V. Giacometti, and A. Kis, *Nat. Nanotechnol.* 6 (2011) 147.
- ¹⁶⁶ E. Benavente, M.A. Santa Ana, F. Mendizabal, and G. Gonzalez, *Coordination Chem. Rev.* 224 (2002) 87.
- ¹⁶⁷ X. Fang, C. Hua, X. Guo, Y. Hu, Z. Wang, X. Gao, F. Wu, J. Wang, and L. Chen, *Electrochim. Acta* 82 (2012) 155.
- ¹⁶⁸ Y. Wang, X. Zhang, P. Chen, H. Liao, and S. Cheng, *Electrochim. Acta* 80 (2012) 264.
- ¹⁶⁹ L. Fei, Q. Lin, B. Yuan, G. Chen, P. Xie, Y. Li, Y. Xu, S. Deng, S. Smirnov, and H. Luo, *Appl. Mater. Interfaces* 5 (2013) 5330.
- ¹⁷⁰ Q. Su, J. Xie, J. Zhang, Y. Zhong, G. Du, and B. Xu, *Appl. Mater. Interfaces* 6 (2014) 3016.
- ¹⁷¹ X. Zhou, L.-J. Wan, and Y.-G. Guo, *Nanoscale* 4 (2012) 5868.
- ¹⁷² S.K. Das, R. Mallavajula, N. Jayaprakash, and L.A. Archer, *J. Mater. Chem.* 22 (2012) 12988.
- ¹⁷³ X. Zhou, L.-J. Wan, and Y.-G. Guo, *Chem. Commun.* 49 (2013) 1838.
- ¹⁷⁴ S. Laruelle, S. Grugeon, P. Poizot, M. Dolle, L. Dupont and J.-M. Tarascon, *J. Electrochem. Soc.* 149 (2002) A627.
- ¹⁷⁵ C. Julien, S.I. Saikh, and M. Balkanski, *Mater. Sci. Eng. B14* (1992) 121.
- ¹⁷⁶ C. Julien, *Ionics* 2 (1996) 169.
- ¹⁷⁷ A.C. Larson and R.B. von Dreele, General Structure Analysis System (GSAS); Report LAUR 86-748; Los Alamos National Laboratory, Los Alamos, NM (2000).
- ¹⁷⁸ B.H. Toby, *J. Appl. Cryst.* 34 (2001) 210-213.
- ¹⁷⁹ R.P. Rao, N. Sharma, V.K. Peterson, and S. Adams, *Solid State Ionics* 230 (2013) 72.
- ¹⁸⁰ R.P. Rao, M. Chen, and S. Adams, in *Solid State Ionics: Ionics for Sustainable World* (eds. B.V.R. Chowdari, J. Kawamura, J. Mizusaki, and K. Amezawa), Proceedings of the Asian Conference on Solid State Ionics Sendai/Japan, World Scientific, Singapore, 2012.
- ¹⁸¹ M. Chen, R.P. Rao, and S. Adams, *Solid State Ionics* 262 (2014) 183.
- ¹⁸² N. Machida, H. Yamamoto, and T. Shigematsu, *Chem. Lett.* 33 (2004) 30.
- ¹⁸³ S. Boulineau, M. Courty, J.-M. Tarascon, and V. Viallet, *Solid State Ionics* 221 (2012) 1.
- ¹⁸⁴ N.A.W. Holzwarth, N.D. Lepley, and Y.A. Du, *J. Power Sources* 196 (2011) 6870.
- ¹⁸⁵ A. Hayashi, H. Muramatsu, T. Ohtomo, S. Hama, and M. Tatsumisago, *J. Mater. Chem. A*, 1 (2013) 6320.
- ¹⁸⁶ M. Chen, R.P. Rao, and S. Adams, *Solid State Ionics* 268 (2014) 300.
- ¹⁸⁷ A. Hayashi, R. Ohtsubo, and M. Tatsumisago, *Solid State Ionics* 179 (2008) 1702.

-
- ¹⁸⁸ A. Hayashi, R. Ohtsubo, T. Ohtomo, F. Mizuno, and M. Tatsumisago, *J. Power Sources* 183 (2008) 422.
- ¹⁸⁹ A. Hayashi, T. Ohtomo, F. Mizuno, K. Tadanaga, and M. Tatsumisago, *Electrochim. Acta* 50 (2004) 893.
- ¹⁹⁰ A. Haznar, A. Pietraszko, and I. Studenyak, *Solid State Ionics* 119 (1999) 31.
- ¹⁹¹ R.B. Beeken, J.J. Garbe, and N.R. Petersen, *J. Phys. Chem. Solids* 64 (2005) 1261.
- ¹⁹² J. Swenson, S. Adams, *Phys. Rev. Lett.* 90 (2003) 155507.
- ¹⁹³ M. Chen, and S. Adams, *J. Solid State Electrochem.* (2014), in press, DOI: 10.1007/s10008-014-2654-1.
- ¹⁹⁴ A.G. Simmonds, J.J. Griebel, J. Park, K.R. Kim, W.J. Chung, V.P Oleshko, J. Kim, E.T Kim, R.S. Glass, C.L Soles, Y.-E. Sung, K. Char, and J. Pyun, *ACS Macro Lett* 3 (2014) 229.
- ¹⁹⁵ X. Zhou, J. Xie, J. Yang, Y Zou, J. Tang, S. Wang, L. Ma, Q. Liao, *J. Power Sources* 243 (2013) 993.
- ¹⁹⁶ K. Li, B. Wang, D. Su, J. Park, H. Ahn, G. Wang, *J. Power Sources* 202 (2012) 389.
- ¹⁹⁷ B. Zhang, C. Lai, Z. Zhou, X.P. Gao, *Electrochim. Acta* 54 (2009) 3708.
- ¹⁹⁸ M. Chen, and S. Adams, *submitted to J. Mater. Chem. A.*
- ¹⁹⁹ G. Du, Z. Guo, S. Wang, R. Zeng, Z. Chen, and H. Liu, *Chem. Comm.* 46 (2010) 1106.
- ²⁰⁰ T. Stephenson, Z. Li, B. Olsen, and D. Mitlin, *Energy Environ. Sci.* 7 (2014) 209.
- ²⁰¹ Y. Han, Y. Wang, W. Gao, Y. Wang, L. Jiao, H. Yuan, S. Liu, *Powder Technol.* 212 (2011) 64.
- ²⁰² Y. Chen, C. Davoisne, J.-M Tarascon, and C. Gu áy, *J. Mater. Chem.* 22 (2012) 5295.
- ²⁰³ H.-C. Tao, X.-L. Yang, L.-L. Zhang, and S.-B. Ni, *J. Phys. Chem. Solids* 75 (2014) 1205.
- ²⁰⁴ B. Jache, B. Mogwitz, F. Klein, and P. Adelhelm, *J. Power Sources* 247 (2014) 703.
- ²⁰⁵ S. Boulineau, J.-M. Tarascon, J.-B. Leriche, and V. Viallet, *Solid State Ionics* 242 (2013) 45.
- ²⁰⁶ M.M. Doeff, *Encyclopedia of Sustainability Science and Technology*, Springer New York (2012) 708.
- ²⁰⁷ <http://www.timcal.ch/scopi/group/timcal/timcal.nsf/pagesref/SCMM-7EVDTT?Opendocument&lang=en> (retrieved on 01 Aug 2014)
- ²⁰⁸ M. Nagao, A. Hayashi, and M. Tatsumisago, *Eletrochem. Comm.* 22 (2012) 177.
- ²⁰⁹ Y. Hamon, T. Brousse, F. Jousse, P. Topart, P. Buvat, and D.M. Schleich, *J. Power Sources* 185 (2001) 97.
- ²¹⁰ C.K. Chan, H. Peng, G. Liu, K. McIlwrath, X.F. Zhang, R.A. Huggins, and Y. Cui, *Nat. Nanotechnol.* 3 (2008) 31.
- ²¹¹ C. Wang, H. Wu, Z. Chen, M.T. McDowell, Y. Cui, and Z. Bao, *Nat. Chem.* 5 (2013) 1042.